Optoelectronics with Carbon Nanotubes

A Dissertation Presented

by

Megumi Kinoshita

to

The Graduate School

in Partial Fulfillment of the

Requirements

for the Degree of

Doctor of Philosophy

in

Physics

Stony Brook University

May 2011

Stony Brook University

The Graduate School

Megumi Kinoshita

We, the dissertation committee for the above candidate for the

Doctor of Philosophy degree, hereby recommend

acceptance of this dissertation.

Emilio E. Mendez – Dissertation Advisor
Professor, Physics

Philip B. Allen - Chairperson of Defense
Professor, Physics

Harold J. Metcalf
Professor, Physics

Stanislaus Wong
Professor, Chemistry

This dissertation is accepted by the Graduate School

Lawrence Martin
Dean of the Graduate School

Abstract of the Dissertation

Optoelectronics with Carbon Nanotubes

by

Megumi Kinoshita

Doctor of Philosophy

in

Physics

Stony Brook University

2011

The carbon nanotube is a promising material for future micro- and nano-scale electronics because of its unique electronic properties, high carrier mobility and extraordinary capacity for high current density. In particular, semiconducting carbon nanotubes are direct bandgap materials with a typical energy gap in the order of 1 eV, which means they emit light in the near-infrared range, making them an attractive option in telecommunications applications. However, there have been few systematic investigations of electrically-induced light emission (i.e. electroluminescence) from carbon nanotubes, and their emission properties are not well understood.

In this dissertation, we explore the characteristics of electroluminescence in three different types of carbon-nanotube devices. The first is a single-tube field-effect transistor (CNTFET), whose emission has previously been found to have a very broad spectral shape and low emission efficiency. We analyze the spectral shape in detail, which reveals that a high electric field near metal contacts contributes most to the bias-dependent component of broadening, in addition to smaller contributions from tube nonuniformity, inelastic scattering of phonons, high temperature, etc.

In the second part of the study, single-tube light-emitting diodes are constructed by employing a split top-gate scheme. The split gate creates p- and n-doped regions electrostatically, so that electrons and holes combine between the two sections and can decay radiatively. This configuration creates electron-hole pairs under much lower electric fields and gives us a greater control over carrier distribution in the device channel, resulting in much narrower spectral linewidths and an emission intensity several orders of magnitude larger than that of CNTFETs. The much better signal-to-noise also leads to the observation of emission from defect-induced states.

Finally, we extend the idea of the single-tube p–n diode and fabricate CNT film diodes from many purified tubes aligned in parallel. While the operating principle is somewhat different from that of single-tube diodes because of the presence of metallic tubes in the material, the film diodes nonetheless show a rectifying behavior and much greater light intensity than single-tube devices. With their superior light output and robustness, they bring us one step closer to a real-world application of carbon nanotubes optoelectronics.

To my son, Sam. I love you.

Table of Contents

Abstract iii
Table of Contents vi
List of Figures viii

Chapter I Introduction 1
1. Structure of single-wall carbon nanotubes (SWNTs) 2
2. Electron-electron and electron-hole interactions in SWNTs 8
3. Phonon modes in SWNTs 12
4. Exciton-phonon coupling in SWNTs 14
5. Transport mechanism in semiconducting SWNT devices 15
6. Electroluminescence from carbon canotube devices 21
7. Problems with carbon-nanotube optoelectronics addressed in this work 26

Chapter II Methods 28
1. Materials 28
2. Device fabrication 30
  i. CNTFETs 30
  ii. Single-tube p-n diodes 31
  iii. Film p-n diodes 33
3. Experimental set-up 34
4. Electroluminescence measurements 36

Chapter III Unipolar, High-Bias Emission 38
1. Introduction 38
2. Experimental results and discussion 39
  i. Unipolar electrical transport characteristics 39
  ii. Electroluminescence intensity in the unipolar regime 43
  iii. Electroluminescence spectra 47
  iv. Observation of polarization effects in electroluminescence spectra 60

3. Conclusions 66

Chapter IV Narrow-Band Electroluminescence from a Single Carbon-Nanotube p-n Diode 67
1. Introduction 67
2. Transport characteristics of the single CNT p-n diode 68
3. Electroluminescence mechanism and characteristics 70
4. Conclusions 80

Chapter V The Polarized Carbon Nanotube Thin Film LED 82
1. Introduction 82
2. Physical characteristics of CNT films and top-gated devices 83
3. Transport characteristics of the CNT film diode 85
4. Electroluminescence characteristics of the CNT film diode 90
5. Investigation of electroluminescence spectra 96
6. Conclusions 106

Summary 107

Bibliography 110

List of Figures

Chapter I

Figure I-1 The honeycomb structure of a graphene sheet 4

Figure I-2 Energy dispersion of graphene 6

Figure I-3 The Brillouin zones of metallic and semiconducting SWNTs. 7

Figure I-4 One-dimentional energy dispersion of metallic and semiconducting SWNTs. 8

Figure I-5 First and second transitions between van-Hove singularities 9

Figure I-6 Phonon energy dispersion for (19,0) CNT 13

Figure I-7 Schematic illustration of a standard bottom-gated CNTFET 18

Figure I-8 Schematic band structure of the first conduction and valence bands in the “on” and “off” states 19

Figure I-9 Schematic illustrations of band structures in ambipolar and unipolar conduction 21

Figure I-10 Ambipolar and unipolar emission mechanisms 22

Chapter II

Figure II-1 Schematics of a back-gated CNTFET device 31

Figure II-2 Schematics of a CNT p-n junction 32

Figure II-3 Schematics of the optics to detect emitted light. 35

Chapter III

Figure III-1 Semi-log plot of drain current as a function of gate voltage 40

Figure III-2 Source-Drain sweep showing saturation 41

Figure III-3 Change in transport from predominantly p-type to n-type FET 42

Figure III-4 Electroluminescence spectrum 44

Figure III-5 Drain current as a function of applied drain-source voltage 45

Figure III-6 Average current as a function of applied V_{DS}.. 46

Figure III-7 EL intensity as a function of current 47

Figure III-8 Electroluminescence spectrum width as a function of power. 48

Figure III-9 The temperatures of three different phonon modes as a function of power.. 53

Figure III-10 EL intensity spectra with blackbody background 55

Figure III-11 Comparison between experimental and theoretical widths 57

Figure III-12 Integrated Lorentz peak intensity as a function of current 58

Figure III-13 Spectra from a device showing E_{11} and E_{22} peaks 60

Figure III-14 Polarization of EL intensity 61

Figure III-15 EL spectra in parallel and transverse polarizations. 63

Figure III-16 EL spectra of the double-peak sample showoing E_{12} emission 65

Chapter IV

Figure IV-1 Device structure and electronic characteristics of the CNT infrared LED... 69

Figure IV-2 Identification of the light emission mechanism... 71

Figure IV-3 Electroluminescence spectra of a CNT diode 74

Figure IV-4 Characteristics of a two-peak CNT p-n junction device 76

Figure IV-5 Comparison between ambipolar and unipolar light emission 79

Chapter V

Figure V-1 SEM and AFM images of self-assembled CNT stripes. 84

Figure V-2 Schematic illustration and SEM image of CNT film diodes 85

Figure V-3 Source-drain electrical current transfer as a function of the top-gate voltage. 86

Figure V-4 Electrical output characteristics of CNT film diodes 88

Figure V-5 Examples of two CNT film diodes with rectifying characteristics 89

Figure V-6 Spatial characteristics and infrared images of EL from a CNT LED 91

Figure V-7 Comparison of light output characteristics of film and single-tube diodes. 92

Figure V-8 EL Threshold characteristics of film FET and diodes 94

Figure V-9 Electroluminescence spectra of a CNT film light emitting diode 98

Figure V-10 Full-width at half maximum of electroluminescence spectra 102

Figure V-11 Total electroluminescence intensity as a function of current 104

Figure V-12 Polarization dependence of the EL intensity from a CNT thin film diode 105

Acknowledgements

First, I would like to express my gratitude to my dissertation advisor, Dr. Emilio E. Mendez, who has been much more than a dissertation advisor to me. If I had not taken his introductory solid state physics course as an undergraduate student, I would never have gone into this field, and without the inspiration I received from his teaching, I may not have gone into teaching. His guidance, understanding and patience helped me persist and finish my graduate work through one of the most challenging periods of my life. I feel honored to have been his student. He also assisted me extensively throughout the editing process. While I am grateful to Dr. Mendez for his assistance, I must clarify that the blame for errors in the empirical analysis and in the writing (if any) lies with me alone.

I would also like to thank the members of my dissertation committee for their interest: Drs. Philip B. Allen, Harold J. Metcalf and Stanislaus Wong. In particular, special thanks go to Dr. Allen who not only served as the committee chair, but also made numerous suggestions for improving my dissertation.

The bulk of the work presented here was conducted at IBM T. J. Watson Research Center in Yorktown Heights, NY, with the group lead by Dr. Phaedon Avouris, and his help and insights are greatly appreciated as well. My collaborators at IBM were very generous with their expertise, from which I learned a tremendous amount and benefited in tangible ways. For this, I am indebted to (titles omitted) Thomas Mueller, Mathias Steiner, Ageeth Bol (for growing countless carbon nanotube samples and for her expert knowledge in nanotube growth), Vasili Perebeinos, Michael Engel, Joshua Small, Damon Farmer (for ALD growth), Bruce Ek (for much technical support and e-beam evaporation), Jim Bucchignano (for e-beam writing), Hsin-Ying Chiu, Jim Tsang, Siyu Koswatta, Yu-Ming Lin, Fengnian Xia, Marcus Freitag, Ali Afzali, George Tulevski, Zhihong Chen, Jim Rozen, Teresita Graham and many others.

This dissertation was finished while I was working at SUNY Orange Community College as a first-year instructor, and I appreciate the understanding and support of my colleagues during that time. In particular, I would like thank John Wolbeck and Stacey Moegenburg for being very understanding and for encouraging me throughout the process. My thanks also go to my other colleagues for cheering me on. I am very fortunate to work in such an incredible work environment.

Carolyn Ramsey and Christian Lavoie helped me through some of the most difficult phases of my graduate life. Without their care, support, understanding and friendship, this dissertation would not have been possible. I am forever grateful for their generosity of heart. In addition, I would like to thank Monica Mack, Merrill and Tamaji Harmin and the members of their meditation group, Hsin-Ying Chiu, Jerome Ramsey, Daniel Kerr, Ching-tzu Chen, Qing Wang, Brian Hessel and all my other friends for their friendship and support.

My parents have been steadfast supporters of my personal and academic pursuits no matter what I wanted to do, through the meandering path I have taken to get to this point. I cannot thank them enough for everything they have given me and done for me.

And last, but not least, I would like to thank my son, Samuel Nicholas Kinoshita-Millard, who never once complained that I spent more time in the lab than with him. It is forever etched in my memory how I would go to the library with him in tow and work for hours on end while he sat quietly and read on his own. My everlasting gratitude to him for his unconditional love, understanding and encouragement.

Chapter I Introduction

It is well recognized that the ongoing scaling down of electronic technology, especially with silicon, cannot continue forever because of its theoretical and technological limits [1]. Alternative device technologies are needed to enhance or replace the current approach. Carbon nanotubes (CNTs), since their discovery in 1991 [2], followed by the discovery of single-walled carbon nanotubes (SWNTs) in 1993 [3] by Iijima, have been a subject of intense research because of the many unique and desirable properties they exhibit, such as their extraordinary tensile strength, the ability to withstand high pH and temperature, and particularly, their distinctive electronic and optical properties [4-6]. Multiwall carbon nanotubes (MWNTs) are concentric tubes of rolled up one-atom layer sheet in a honeycomb configuration of carbon atoms (i.e. graphene), while SWNTs are composed of only one such tube. The diameter of a CNT can be sub-nanometer for SWNTs, up to a few to tens of nanometers. Detailed physical characteristics of these structures are covered in the next section.

The SWNT with its simpler structure has garnered a greater interest in electronics; it can be a semiconductor or a metal with very high mobility that can withstand enormous current densities. This makes it attractive for use in nano-scale electronics, as the sizes of integrated circuits become ever smaller and are reaching the natural limit of miniaturization. Currently, as silicon devices are made smaller and denser, problems with leakage through dielectric and heat dissipation are two major obstacles to the further scaling down in existing chip designs. The superior mobility of SWNTs means less phonon scattering (i.e., less heat production per unit current), and their extremely small sizes are naturally advantageous in micro- and nano-scale electronics. Field-effect transistors made from CNTs (CNTFETs) were demonstrated as early as 1998 by Tans et al. and Martel et al. [7, 8]. Compared to conventional bulk silicon MOSFET, CNTFET exhibits superior performance in terms of transconductance and drive currents by a factor of a few per unit width, making it an attractive alternative to silicon [9]. In addition, as will be discussed shortly, their reduced dimensionality contributes to their unique electrical and optical properties, which make them a promising candidate for near- to mid-infrared optoelectronics.

This work explores both fundamental physical properties and application possibilities of electroluminescence (EL) from semiconducting CNT devices. While there has been much work on photoluminescence (PL) from CNTs in solution and suspended in air (see, for example, the chapter on PL by Lefebvre, et al. in Ref. 6 and references therein), electrically induced luminescence has been less explored because of complexity of device fabrication, its typically low luminescence efficiency, e.g., as low as 10^{-10} in some cases [10], and limitations in the detection technology of infrared radiation. Additionally, until 2009, when EL from CNT p-n junction was observed for the first time [11], very high fields and accompanying high current/heating was a hindrance to elucidating the details of luminescence characteristics. While laser-induced PL studies have done a great deal to help us understand the fundamental physics of CNTs, it is vital that we understand their EL mechanisms and apply the knowledge to the development of carbon-based, nano-scale optoelectronics in order to capitalize on the unique properties of CNTs in application.

In the effort to contribute to these endeavors, this thesis reports on the findings from three distinctly different CNT device structures: (1) conventional bottom-gated CNT field-effect transistors (CNTFETs) operated in the unipolar transport and emission regime; (2) single-tube, top split-gate CNT p-n junction devices as light-emitting diodes (LEDs); and (3) top split-gate p-n junction LEDs with self-aligned, purified semiconducting SWNTs. Each device probes different aspects of EL mechanisms, the results of which, we hope, will come together to play an important part in advancing the science and technology of this fascinating material. In the rest of this chapter, fundamentals of carbon nanotube physics are discussed with a particular emphasis on their transport and luminescent properties to provide background information for subsequent chapters.

1. Structure of single-wall carbon nanotubes (SWNTs)

With the diameter in the order of only a nanometer and the length ranging up to microns and even millimeters, SWNTs are a prime example of almost perfect one-dimensional structures. This reduced dimensionality has several significant consequences for their electronic and optical properties, which are discussed in this and the following sections.

An SWNT can be defined as a cylinder of a rolled up graphene sheet, which is a monolayer of carbon atoms in a honeycomb structure (Figure I-1). Note that CNTs are not actually manufactured from graphene and that this is a conceptual convenience; see the methods section for details of carbon nanotube synthesis. In graphene, each carbon atom has four valence electrons (i.e., $2s$, $2p_x$, $2p_y$ and $2p_z$), three of which ($2s$, $2p_x$, and $2p_y$) are sp^2 hybridized and form covalent bonds with the nearest neighbor atoms, making graphene a very stable structure. Graphite is many sheets of graphene that are stacked, while another allotrope, diamond, forms covalent bonds with all four valence electrons with four neighboring atoms. Carbon nanotubes' exceptional tensile strength is also due to the covalent bonds. The remaining fourth $2p_z$ electron in graphene/carbon nanotube is free and contributes to conduction.

The way in which an SWNT is "rolled up" from graphene defines its structure and determines the electronic properties. Figure I-1 shows the graphene honeycomb structure in real space with unit vectors $\mathbf{a_1}$ and $\mathbf{a_2}$, and the chiral vector **C** for a particular SWNT (i.e., a (4, 5) SWNT). The structure can be visualized as a strip of graphene cut along the dotted lines perpendicular to **C** and rolled up in the direction of **C** into a long cylinder so that the length $|\mathbf{C}|$ becomes the circumference. The chiral vector uniquely defines a SWNT and can be expressed as

$$\mathbf{C} = n\mathbf{a}_1 + m\mathbf{a}_2 \qquad \text{(Eq. I.1)}$$

where n and m are integers. The indices (n, m) are sufficient to define any SWNT; the figure shows, for example, the (4, 5) nanotube. There are two specific types of nanotubes called "armchair" where $n = m$, and "zigzag" where $m = 0$, named after the pattern of lines connecting the atoms seen around the circumference. Armchair nanotubes are always metallic, but zigzag tubes can be either semiconducting or metallic (see below). These are useful structures that appear frequently in theoretical work because of their high degree of symmetry that simplifies calculations. In practice, SWNTs are a family of many different structures with varied electronic and optical properties, the fact that poses interesting and often challenging problems. For example, there is little control over what types of SWNTs are produced in any fabrication method. Although there is usually a limited range of diameters and the number of sidewalls (i.e., SWNT vs. MWNT) depending on the growth conditions and catalyst particles, the product is always a mixture of metallic and semiconducting CNTs of different diameters, chiralities and lengths, which makes it difficult to control their properties and identify their (n, m) designations.

In fact, we typically have no knowledge of the actual *n* and *m* values of a CNT used in an electronic device, since getting a PL signal from a single tube (the only way to identify them) on a surface is very difficult and laborious.

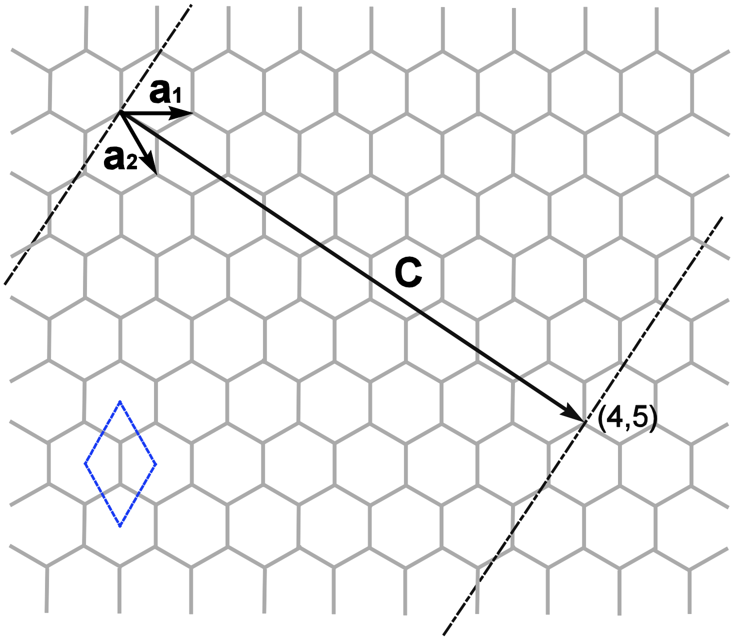

Figure I-1. The honeycomb structure of a graphene sheet in real space, showing the example of a (4, 5) SWNT. One carbon atom exists at each hexagonal point. $\mathbf{a}_1$ and $\mathbf{a}_2$ are unit vectors, and **C** indicates the chiral vector for the SWNT. The blue dotted lines indicate the primitive unit cell containing two translationally inequivalent atoms.

Once the chiral vector and therefore the type of a SWNT is defined, its diameter d can be expressed as

$$d = \frac{\sqrt{3}a_{c-c}\sqrt{n^2 + m^2 + nm}}{\pi} \qquad \text{(Eq. I.2)}$$

where a_{c-c} is the distance between neighboring atoms, known to be 0.142 nm. A typical SWNT has the diameter in the order of only nanometers, so this confinement quantizes the component of the momentum **k** in the circumferential direction of the cylinder. In other words, the quasi – 1D nature of the nanotube imposes a true periodic condition around the circumference and defines the Brillouin zone of the nanotube in that direction. The quantization condition,

$$\mathbf{C} \bullet \mathbf{k} = 2\pi i; \quad i = 1, 2, 3... \qquad \text{(Eq. I.3)}$$

determines whether the SWNT is metallic or semiconducting; if the momentum vector coincides with the location in graphene k-space where there is no bandgap, it is metallic, otherwise, it is semiconducting. This is a direct consequence of the energy dispersion relation in graphene which is now discussed in greater detail.

The energy dispersion of graphene considering only the π and π* orbitals was calculated as early as 1947 by Wallace [12] using the tight-binding approximation. This model shows that graphene is a zero-bandgap semiconductor (or semimetal) with a linear dispersion near the Fermi level (Figure I-2). At low energy, it can be approximated as cone shapes meeting at K and K' symmetry points of the Brillouin zone, called the Dirac points (Figure I-2 (b)). Taking the low-energy approximation in terms of k = |**k**-**k_F**| based on the graphene energy eigenvalues from Ref. 12, we get

$$\begin{aligned} E(k) &= E_F \pm \frac{\sqrt{3}}{2}\gamma_0 ka \\ &= E_F \pm \hbar v_F k \end{aligned} \qquad \text{(Eq. I.4)}$$

where γ_0 is the C-C transfer energy and a □ is the unit vector length (Figure I-1). Using known values for γ_0 and a gives the Fermi velocity $v_F \approx 8.7 \times 10^5$ m/s. Note that there is only one electron per atom contributing to these orbitals; in an updoped graphene at zero temperature, the valence band is completely filled and the conduction band is empty, making graphene a semi-metal (or a zero-bandgap semiconductor). How these cones are effectively "cut" by an SWNT's circumferential momentum determines whether the SWNT is metallic or semiconducting.

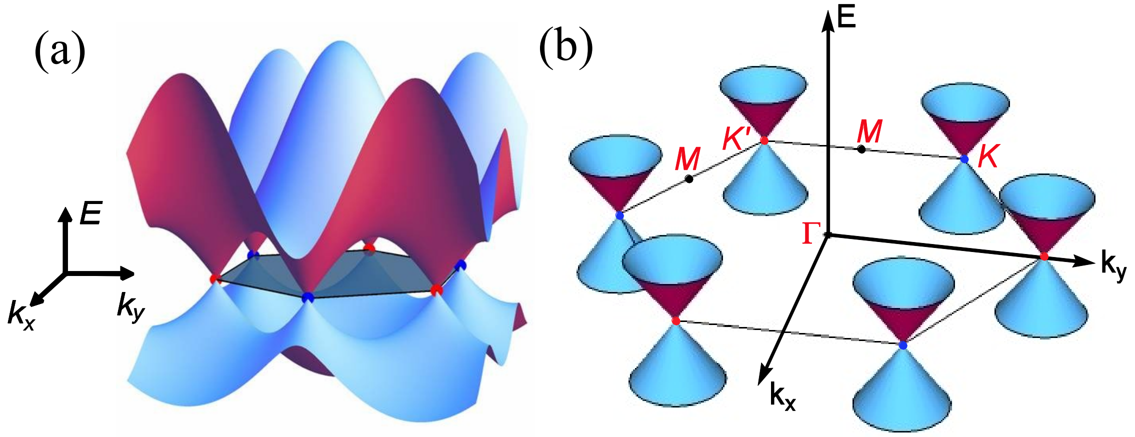

Figure I-2 (a) Energy dispersion of graphene showing inequivalent *K* and *K'* points as blue and red dots, and (b) details at low energy, showing the linear dispersion. *K*, *K'*, *M*, and *Γ* are high-symmetry points in graphene's Brillouin zone. The plane of the hexagons denotes the Fermi level.

Figure I-3 further illustrates the difference between these two types of SWNTs in reciprocal space. If the quantized momentum vector in the circumferential direction of an SWNT coincides with a Dirac point, it is metallic. If it misses the Dirac point, it creates an energy gap (i.e., the cone is cut away from the point) and the SWNT is semiconducting. Using the (n, m) indices, it can be shown that if (n - m) / 3 is an integer, the SWNT is metallic; otherwise it is semiconducting. Therefore, if SWNTs are produced randomly in bulk, two-thirds should be semiconducting on the average. It should be pointed out that this is a simplified picture in the first order approximation, and the linear dispersion approximation may be less valid in certain situations such as in small-diameter tubes (i.e., large unit wave vector in the circumferential direction). For example, the so-called trigonal warping effect (a distortion of equi-energy contours away from the circular shape that connect *M* points in a triangle) can create a small energy gap in the order of meVs in metallic nanotubes [4, 13].

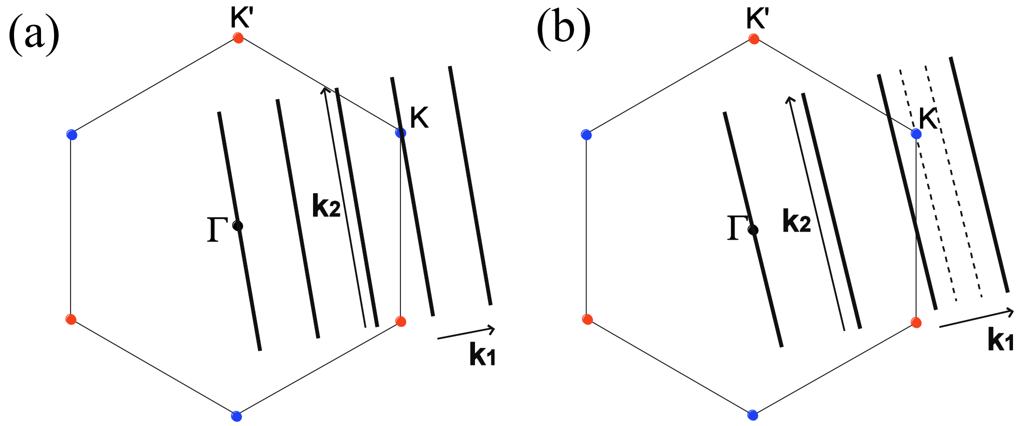

Figure I-3. The Brillouin zones of (a) metallic and (b) semiconducting SWNTs mapped onto the hexagonal Brillouin zones of graphene. The blue (K) and red (K') dots indicate the Dirac points where conduction and valence bands meet, as in Figure I-2. Note that in (b), the "cutting line" of the quantized momentum misses the K point, thus creating an energy gap. Reciprocal lattice vectors $\mathbf{k_1}$ corresponds to the chiral vector **C** in Figure I-1, and $\mathbf{k_2}$ to the translational vector in the direction of the long axis of the CNT (not shown in Figure I-1).

Based on Equation (I.4) and the above argument, the one-dimensional energy-dispersion can be expressed as

$$E(\Delta) = E_F \pm \sqrt{(\hbar v_F k)^2 + (j\Delta)^2};\ \text{j=0, 1, 2, ...} \qquad \text{(Eq. I.5)}$$

where Δ is one-half of the energy gap, which depends on the diameter of the tube. Figure I-4 shows the first three bands of metallic and semiconducting SWNTs calculated for when ν is (a) 0, 3, and 6 (metallic), and (b) 1, 2, and 4 (semiconducting). Once the one-dimensional energy dispersion is thus known, the corresponding density of states (DOS) can be calculated (shown in green in Figure I-4). As seen in Figure I-4, the DOS shows singularities named van Hove singularities because of the SWNT's reduced dimensionality.

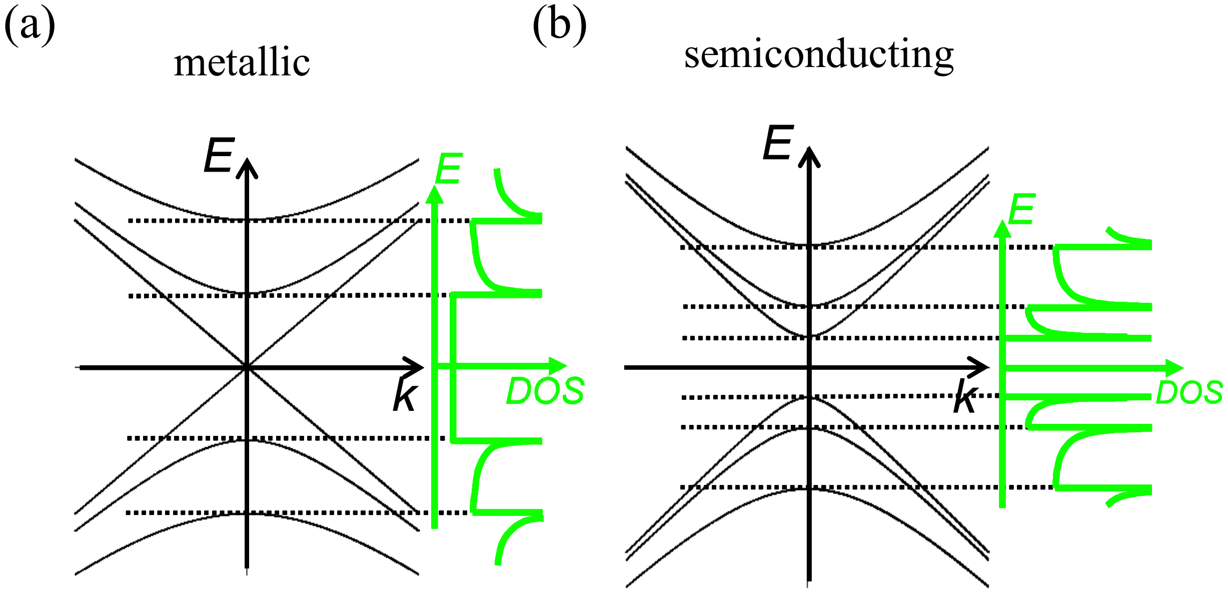

Figure I-4. One-dimensional energy dispersion of (a) metallic and (b) semiconducting SWNTs according to the single-particle interband theory. Corresponding density of states with van Hove singularities are indicated in green.

In an undoped SWNT at zero temperature, the bands are filled up to the Fermi level because there is only one extra electron per atom. The energy gap in semiconducting SWNTs are in the order of 1 eV, meaning that we can expect to see transition effects from electrically or optically excited carriers across the gap at room temperature. However, the unique dimensionality of carbon nanotubes has a further consequence that needs to be considered first, namely, many-body effects.

2. Electron-electron and electron-hole interactions in SWNTs

There are two main effects that significantly modify the single-particle bandgap, E_g, described in the previous section. One is the electron-electron repulsion, which contributes to the self energy E_{ee} of the system. The other is the creation of localized electron-hole pairs bound by the Coulomb attraction, forming hydrogen-like particles called excitons, each with a series of Rydberg states. The energies of these two effects are both significant fractions of the single-particle bandgap in one-dimension and considerably affect the electrical and optical excitations of carriers and emission of photons. Initially the single-particle model served adequately enough in explaining the optical phenomena, partly because the two Coulombic effects tend to cancel each other in the diameter range (around 1 nm) that has been the main focus of investigation.

Excitonic effects in luminescence have been demonstrated in traditional bulk semiconductors. The exciton binding energy in these materials is typically tens of meV and manifests itself as a sharp peak below the broader spectrum from free particles, observable only in low-temperature measurements. In the early days of carbon nanotube research, optical transitions were interpreted using the same single-particle model combined with the corresponding one-dimensional density of states. In this model, electrons are excited optically or electrically from a valence band to a conduction band at van-Hove singularities and generate light when they relax down to a lower-energy state by emitting a photon. Figure I-5 shows schematically the radiative transitions between van-Hove singularities leading to photo-emission. The energy differences between the conduction and valence bands are referred to as Δij, where i = 1,2,3… denotes the first, second, third… valence bands and j likewise refers to the conduction bands. In contrast, excitonic transition levels will be referred to as E_{11}, E_{22}, etc.

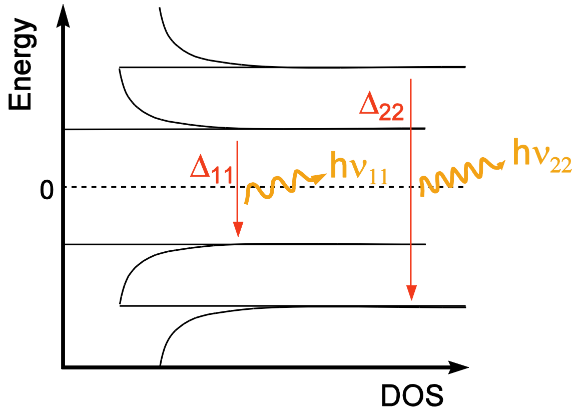

Figure I-5. First and second transitions between van-Hove singularities (i.e., sharp peaks in the DOS). Δ_{ij} denotes the energy difference between the ith valence band and the jth conduction band.

Because the quantized momentum normal to the tube axis is determined by the tube circumference, the transition energies depend on the SWNT diameter (Figure I-3). The transition energy-diameter relationship was first presented by Kataura, et al. to explain observed optical absorption peaks for different samples and their corresponding diameter measurements by transmission electron microscopy (TEM) [14]. The so-called Kataura plot and its subsequent enhancements (especially Ref. 15) have been widely used to identify the diameter and even particular species of SWNTs, although it was developed within the van-Hove transition scheme. While Kataura mentions the effect of excitons briefly in his original paper, it is treated as a slight deviation from the calculated values.

The discrepancy between the single-particle picture and the nature of excitation and emission observations first became apparent in the so-called "ratio problem" [16, 17], in which the ratio of the energy of the second-excited state to the first one deviates significantly from the expected value of 2 expected from the single-particle picture (see Figure I-5). While there are additional complicating factors because of the chirality and the warping that comes from the rolled geometry, the average ratio should approach 2 as the diameter increases and the system goes from one dimension to two. The actual picture turns out to be an interplay of electron self-energy E_{ee} and the exciton binding energy E_b: the effect of the former interaction remains the same as the diameter increases because it is an intrinsic property of graphene, while the latter scales roughly as d^{-1} (Ref. 18). Since E_{ee} blueshifts the first and the second transitions by nearly the same amount, the ratio approaches a value smaller than 2 (Ref. 19). Recently, a successful direct measurement of electronic bandgap ($\approx E_g + E_{ee}$) under different dielectric environments was conducted using scanning tunneling spectroscopy (STS) in which the self-energy correction was deduced to be in the order of 500 meV [20]. It should also be noted from this experiment that the environmental medium also plays a significant role, as it screens the electron-electron interaction. The effect is thought to scale as the inverse of the dielectric constant, ε [21, 22].

Now we discuss the excitonic effect, which also modifies the optical transition energies. Beginning with Ando's theoretical work [23], it became increasingly apparent that the binding energy E_b of excitons in nanotubes is a significant fraction of the bandgap. The Coulomb interaction between an electron and a hole is greatly enhanced in one dimension, and the charge screening is also reduced, all contributing to a large E_b. Collaborating theoretical [24, 25] and experimental [26-28] works have provided definitive evidence for the excitonic nature of observed optical transitions in SWNTs, especially the two-photon excitation experiments [18, 26, 28] and the observation of sidebands from an exciton-phonon complexes [27, 29, 30]. Perebeinos, et al. [24] gives a general expression for E_b that agrees well with the results of the two-photon experiments if one uses the parameter $\varepsilon = 3.3$; namely $E_b = Cd^{a-2}m^{*a-1}\varepsilon^{-a}$, where C and a are empirical constants with $a = 1.40$ and m* is the carrier effective mass. This gives the typical value of E_b to be hundreds of meVs, compared to the single-particle bandgap in the order of 1 eV, making it possible to observe the excitonic effects at room temperature. Note that E_b depends sensitively on the dielectric environment as seen in the factor $\varepsilon^{-1.4}$.

Because electrons and holes (the spin of the latter is defined to be the opposite of the electron that has left the hole) can either be spin up or down and the conduction and valence bands are doubly degenerate, the first excited state of exciton can have a four-fold degeneracy. The degeneracy is actually lifted by the exchange energy, resulting in optically active "bright" excitons and so-called "dark" excitons that do not decay radiatively. Theoretical and experimental studies generally indicate that the lowest state is a dark exciton and the second lowest state is a strong bright exciton with a large dipole moment along the tube axis [31, 32]. The first dark excitonic state is lower in energy than the lowest bright state by about ten meV, contributing to the non-monotonic dependency of exciton radiative lifetime on the temperature and to the poor PL efficiency at room temperature [33-35].

The dominance of excitonic absorption and emission were not apparent initially also because almost all the oscillator strength in absorption spectra is transferred from the interband free particle states to the excitonic states [24, 25], making it difficult to observe both states simultaneously. Another complicating factor is a large shift due to the environment which modifies both E_{ee} and E_b. Most photoluminescence (PL) measurements have been conducted in solution or with suspended tubes because the substrate quenches the signal severely. The measured values were not necessarily comparable across studies for this reason. While there is now ample evidence of the dominance of excitonic transitions in SWNTs, the investigation is far from complete, as the effect of doping, which has not been studied systematically, is also expected to significantly modify the bandgap and the binding energy [36].

Since the radiative lifetime determines the emission efficiency, understanding different decay pathways is crucial in scientific understanding and in technical applications. The major decay pathways include non-dipole allowed states (i.e. "dark excitons") and non-radiative decay due to scattering with phonons. As has been mentioned, the presence of dark excitons contributes to the poor emission observed from SWNTs since excitons in the radiative state can relax rapidly to lower non-radiative states [19]. Another factor is an array of phonon modes that exist in SWNTs; phonons can serve as a valuable measurement tool, but they also make it much more challenging to understand SWNT optoelectronics. Inelastic scattering of phonons is a decay mechanism that affects EL and PL efficiency very significantly.

3. Phonon modes in SWNTs

Resonance Raman spectroscopy (RRS) has been a standard tool in the optical investigation of SWNTs since the first observation of a single-tube RRS in 2001 [37]. It is also commonly used in characterization of bulk samples, but the resonance-dependence of Raman signal intensities complicates the determination of relative abundance of different tubes. There are several characteristic phonon modes that are observed in SWNTs using this technique. Figure I-6 shows an example of phonon dispersion that shows the six branches of phonon modes in SWNTs. Because of the energy-momentum conservation requirement, one can only observe phonons near the Γ point in the first order, although secondary processes produce additional observable peaks. Here, we only discuss some commonly observed modes that are relevant to PL and EL experiments.

The radial breathing mode (RBM) is the lowest vibrational mode observable in RRS, ranging in wavenumber from only 100 to 400 cm^{-1}. It originates from the expansion and contraction in the radial direction of nanotubes perpendicular to the axis, and is therefore sensitive to the diameter of the tube. The frequency ω_{RBM} is known to be inversely proportional to the nanotube diameter; the empirical equation $\omega_{RBM} = 248\ cm^{-1}\ nm/d$ is commonly used to determine the diameter and even the particular (*n, m*) assignment of SWNTs on a SiO_2 substrate, as long as the diameter is below ~1.8 nm [37]. For larger diameter tubes, too many SWNTs can be resonant with the laser energy used in a given Raman measurement, so the identification of a particular SWNT species is difficult. On the other hand, it is very unlikely that one can get a strong enough RBM signal from any given individual SWNT if the excitation energy does not happen to be in resonance with an absorption energy of that specific tube [38]. In addition, larger diameter tubes have a small $\omega_{RBM,}$ so the Raman peak is not easily distinguishable from the laser excitation line.

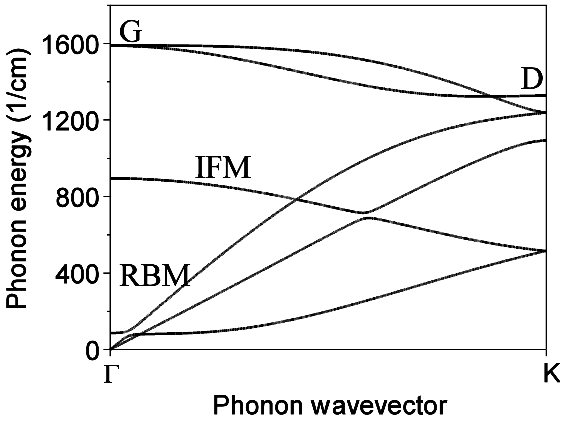

Figure I-6. Phonon energy dispersion for (19,0) CNT showing six branches. The lowest three are low-energy acoustic phonons, and the other three are optical phonons. Commonly observed modes are marked as RBM (radial breathing mode), G (graphite-like mode), IFM (intermediate frequency modes), and D (disorder-induced mode).

The graphite-like band (G-band) around 1500 to 1600 cm^{-1} comes from the stretching mode of carbon-carbon bonds of neighboring atoms in the tangential plane to the SWNT sidewall. It is a high-frequency optical phonon mode that couples strongly to excitons (because it modifies the electronic structure directly) and is therefore observable in excitonic photo-emissions from SWNTs [39], which will be discussed further. Graphite has a single G-band at 1582 cm^{-1}, but in SWNTs, it is split into G$^+$ and G$^-$ lines due to the quantum confinement of the k-vector in SWNTs [6]. The G$^+$ line is associated with vibrations along the long nanotube axis (LO phonons) and is therefore insensitive to the diameter, while the G$^-$ line comes from vibrations in the circumferential direction (TO phonons) and is diameter-dependent [38]. (Note that Piscanec, et al. calculated that the LO phonons may be downshifted enough to be below the TO phonon signal in metallic SWNTs due to the Kohn anomaly [40].) A detailed study of the G-band from a large sample found that the frequency of the G$^-$ band ω_{G-} can be fitted well as a function of the frequency of the G$^+$ band ω_{G+}: $\omega_{G-} = \omega_{G+} - 47.7\ \text{cm}^{-1}\text{nm}^2/d^2$ for semiconducting SWNTs [41]. Hence, the G-band frequencies can be used to determine the diameter when RBM is not available.

The disorder-induced band (D-band) is observed at 1300 to 1400 cm^{-1} and originates from symmetry breaking that occurs because of impurities, structural defects, etc., which couples the laser photons with the phonons near the K and K' points of the Brillouin zone (Figure I-6). It is the most common second-order feature, which appears as a result of relaxing the selection-rule in sp^2-hybridized carbon structures [38]. Because it is dependent on the presence of disorders, its relative intensity with respect to the G-band is used to gauge the structural integrity of a single tube or the purity of bulk nanotube samples. For example, this line could be virtually absent in chemical-vapor deposition (CVD) grown SWNTs that have not gone through additional chemical processing [42]. The CVD process is discussed in greater detail in the Methods section.

There are other lines from second-order phonon processes that are commonly seen. One of them is the G'-band (or 2D-band) at 2600 cm^{-1}, which is the first overtone of the D-band. Another common second-order phonon signature is the IFMs (intermediate frequency modes) that show up as low-intensity features between RBM and the D-band. They can be explained as double-resonant processes involving two phonons that connect two electronic states [38]. While these and other second-order processes are commonly observed in RRS, it is the G-band that has been of utmost interest in spectral features of SWNT emission because of the strong coupling of the high-frequency optical phonons to excitons.

4. Exciton-phonon coupling in SWNTs

Distinct satellite peaks to a main electronic-level transition (E_{11} and/or E_{22}) have been observed in photoluminescence excitation (PLE) [29, 30, 43], PL [44], and photoconductivity (PC) spectra [27], the strongest one being at approximately 200 meV from the main peak and showing a characteristic asymmetric shape. Perebeinos, et al. theoretically investigated the role of coupling between excitons and phonons in optical absorption by solving the Bethe-Salpeter equation with Hamiltonian that takes into account electron-phonon interactions [39]. They found that a significant fraction (8% for a (17, 0) tube) of the total spectral weight is transferred to exciton-phonon complexes, especially to the coupling of excitons and optical LO phonons at about 200 meV from the main peak, with an asymmetric lineshape. For free-carrier transitions, coupling to the phonons was found to merely modify the main peak somewhat, without creating a side band.

Furthermore, the fraction of spectral weight transfer is expected to depend on the nanotube diameter, which was also observed in a PLE experiment [29]. The appearance of such a phonon side band is another strong evidence for the dominance of excitonic transitions in SWNT light emission and absorption.

In Perebeinos' theoretical work, some of the spectral weight was also found to be transferred to the coupling to the RBM phonons, which is very close to the exciton line because of the low energy of the RBM phonons near the Γ point [39]. More recently, an updated theoretical work taking multiphonon sidebands into account also suggested the presence of a sideband due to RBM phonons, in addition to a prominent sideband due to the LO phonon coupling with the bright exciton [45]. The presence of an exciton-phonon sideband has also been observed in metallic SWNTs using Raleigh scattering spectroscopy [46], highlighting the importance of excitons even in metallic tubes in which screening plays a greater role and exciton binding energy should be smaller. Given the prominent characteristics of phonon modes in SWNTs and their strong coupling to excitons, phonons are expected to play an important part in EL as well.

5. Transport mechanism in semiconducting SWNT devices

In EL, carrier transport is an essential aspect of the operating principle because it is by electrically exciting carriers in a device that a CNT generates light. Here, we discuss electrical transfer characteristics of SWNTs, with the main focus on semiconducting tubes, since this work explores EL originating from excitation of carriers across the bandgap. Electrical emission from metallic tubes has also been observed and will be touched on briefly in the subsequent section on the history of EL theory and observations.

One of the remarkable characteristics of carbon nanotubes is their extraordinary ability to withstand a current density exceeding 10^9 A/cm^2 [47-49]. For metallic nanotubes, the current-carrying capability seems to hit a limit at 25 μA by Joule self-heating [50] and by the scattering of optical phonons [49, 51-53]. Since the inelastic optical phonon scattering length is about 10-15 nm [54], a SWNT can carry even more current, up to 100 μA [55] if the channel is shorter than that characteristic length.

The saturation limit for semiconducting SWNTs is more complex, since a main source of a device's electrical resistance is the Schottky barrier at the nanotube-metal contact whose height depends on the diameter and work function of the contact metal [56], and also because the phonon scattering mechanism is different from metallic tubes because of the different electronic band structures. Large diameter tubes form thin and small Schottky barriers, i.e., "transparent contacts" through which carriers can easily tunnel. In such tubes, there is some evidence that the saturation behavior is similar to that of metallic tubes [55, 57]. However, others have shown that this limit can be exceeded in semiconducting tube devices (limited by velocity saturation) [58], and there is evidence that avalanche generation of carriers involving higher subbands can create a current "up-kick", allowing currents > 25 μA in semiconducting tubes [54].

The three main sources of resistance that limit carrier transport in SWNTs are (1) the quantized contact resistance R_Q arising from the mismatch in the number of states between bulk contacts and a 1D nanotube; (2) elastic and inelastic scattering mechanisms; and (3) Schottky barriers and possible additional contact resistance. When R_Q is the only resistance observed, the conduction is said to be in the "ballistic" regime, i.e., no scattering or energy losses occur in the channel. SWNT is a structure that enables the observation of ballistic conduction in one dimension, but only if the channel length is less than the mean free path of the scatterers and if the Schottky barriers are transparent.

Quantized contact resistance R_Q is inherent in the structure of a device and thus puts a theoretical limit on its conductivity. The minimum resistance R_Q that can be achieved when contacting three-dimensional electrodes with continuous states to a one-dimensional SWNT with discrete states is calculated to be

$$R_Q = \frac{h}{2e^2 M} \qquad \text{(Eq. I.6)}$$

where M is the number of modes between the Fermi levels of the source and drain [59]. M = 2 (valley degeneracy) in metallic SWNTs, so in a ballistic conductor, R_Q is 6.5 kΩ. Resistances approaching this limit have been demonstrated in both metallic [60, 61] and large-diameter (2 to 2.4 nm) semiconducting [57] SWNT devices.

Carbon nanotube's superior conduction due to limited scattering and hence the high mobility in SWNTs is a result of their unique one-dimensional structure. Because small-angle scattering is not allowed in a 1D material (i.e., carrier motion is limited to forward and backward), and because contemporary manufacturing methods produce SWNTs relatively free of defects and impurities, the elastic mean free path (mfp) can be very long, in the order of microns [62]. This means that the transport properties are largely determined by inelastic scattering, mostly of phonons. At low bias and/or low temperature, only low-energy acoustic phonons can participate in inelastic scattering. However, the coupling between acoustic phonons and electrons is weak because of the aforementioned scattering-angle restriction, and also due to the energy-momentum conservation requirement, resulting in only a small fraction of acoustic phonons that can contribute to this process. The optical phonon energy is very high (~200 meV), so they do not come into play at low-bias/temperature. Thus, the carrier mobility is very high (upward of ~ 100,000 cm^2/Vs) in SWNTs [63], even at room temperature. At high bias, carriers can produce high-energy optical phonons, which modify the carbon-carbon bonds in SWNTs and thereby change the electronic structure; such phonons naturally couple strongly to carriers. As discussed in the current saturation section above, optical phonons have a very short mfp which leads to the maximum current limit, especially in suspended devices, where phonons cannot be easily dissipated through the substrate and even lead to negative differential conductance [53].

The third important mechanism that affects the transport, the Schottky barrier, is best understood in the context of carbon nanotube field-effect transistors (CNTFETs). The conventional CNTFET design is shown in Figure I-7 (a) and has been used in many experiments because of the relative ease of fabrication and its effectiveness and reliability. The carbon nanotube itself provides the transport channel when contacted on each end by bulk metal, and the heavily doped silicon substrate acts as the back gate, with SiO_2 (or another dielectric material) as the gate dielectric. The switching behavior of a CNTFET is such that one can obtain an I_{on}/I_{off} ratio of 10^5 to 10^7 and an on-current of ~1 μA at the operating drain-source voltage V_{DS} of 1V. The details of the conduction characteristics depend on the tube diameter, the choice of the contact metal, etc. (Figure I-7 (b)).

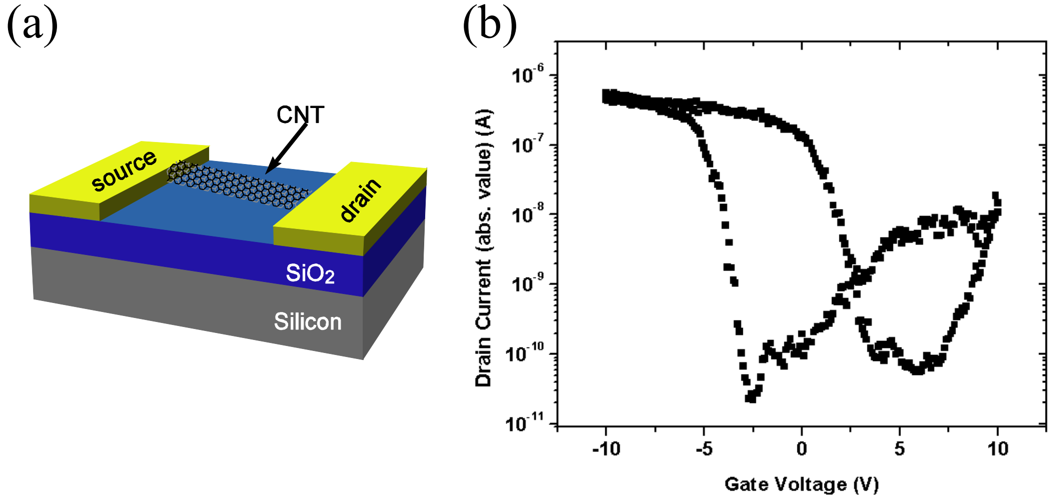

Figure I-7. (a) A schematic illustration of a standard bottom-gated CNTFET. The substrate is typically heavily doped silicon with a gate dielectric layer (thermally grown SiO_2 in our samples). (b) An example of the change in drain current as the bottom gate is swept between -10 V and 10 V. The drain voltage was kept constant at -1 V. This device shows mostly p-type conduction. The hysteresis is due to trap charges in the gate dielectric.

Subsequent studies have shown that unlike the conventional MOSFET in which the channel conduction itself is modulated by the gate, CNTFETs operate as Schottky barrier transistors in which the gate controls the Schottky barriers and hence the injection of carriers. Heinze, et. al modeled a realistic device geometry with a Schottky barrier at the metal-SWNT contact and showed that it agrees well with experimental observations and explains the effects of gas adsorption by the metal contacts [64]. Léonard, et al. also showed theoretically that given the 3D to 1D geometry of the contacts, it is the metal work function of the contacts that control the transport behavior, and that Fermi-level pinning does not affect the Schottky-barrier height [65]. Experiments confirmed that the transport in CNTFETs is controlled by the Schottky barrier, and highlighted the importance of choosing the right metal as a contact [56, 66, 67]. It was in this context that ballistic conduction in CNTFETs was achieved by using larger diameter tubes and a contact metal such as palladium, which has a high work-function and wets well with CNT [57]. In fact, palladium has become the metal of choice for creating p-type carbon nanotube devices with good conduction. Palladium's work function, known to be 5.12 eV [68], is among the highest in commonly available metals, so the Fermi level aligns with the valence band edge, allowing for holes to tunnel easily into the conduction channel.

Thus, the alignment of bandgap with the Fermi level of the contact metal determines the type of conduction that takes place. If the Fermi level aligns midgap with the CNT, both types of carriers can be injected from opposite contacts, in which case the device is defined to be ambipolar. In ambipolar devices, the back gate can be biased positive or negative to switch the majority carrier. On the other hand, in a unipolar device, either the conduction or valence band edge aligns with the Fermi level of the metal, so the current is carried mostly by electrons or holes, respectively. For such a device, only one polarity of the back gate will allow significant conduction.

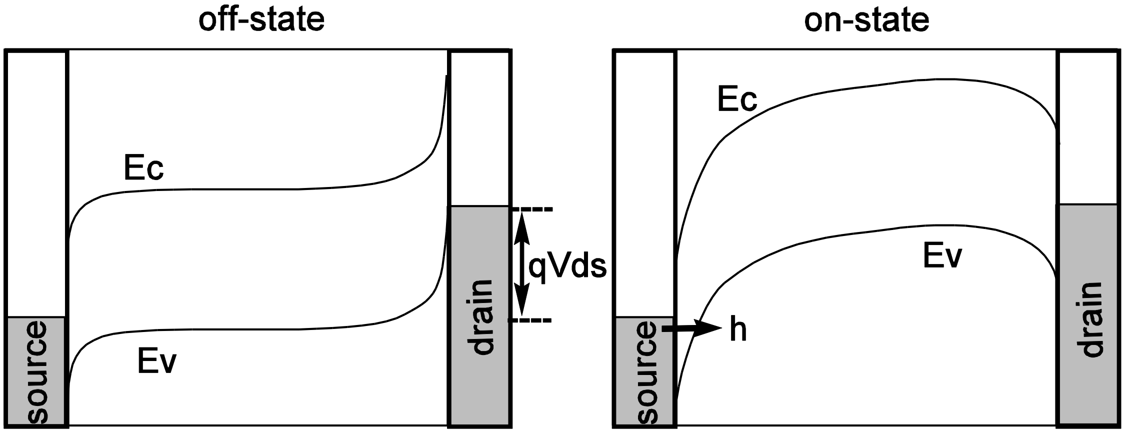

Figure I-8. Schematic band structure of the first conduction (Ec) and valence (Ev) bands in the “on” and “off” states. The source-drain bias (V_{DS}) is the same in both cases. In the on-state, applied gate voltage changes the thickness of the Schottky barrier, allowing p-type carriers (denoted “h” for holes) to tunnel through.

Figure I-8 illustrates how a CNTFET operates as a p-type device. In the “off” state, the p-type carriers, i.e., holes, at Fermi level cannot tunnel through the Schottky barrier into the conduction channel. By changing the band bending with an applied gate voltage (V_{GS}), the barrier becomes thin, allowing the holes to tunnel from the contact into the channel. As is apparent from Figure I-8, the effective Schottky barrier thickness is the critical property that determines the conductivity of the device. Appenzeller, et al. demonstrated that thermally-assisted tunneling through Schottky barrier is the dominant injection mechanism by comparing a simulation and measurements using carbon nanotube and boron nitride nanotube FETs [69]. Later, detailed imaging of band bending at contacts was conducted via spatially-resolved photoconductivity on ambipolar SWNT devices [70], confirming the presence of Schottky barriers and characterizing them at different gate voltages. In this experiment, absorbed photons create excitons across the bandgap, which are separated by the electric field present at the Schottky barriers and detected as current. Current intensity as a function of position yields spatially-resolved electric field strengths, i.e. band potential profile along the channel.

Figure I-9 compares ambipolar and unipolar conduction to show that ambipolar devices (i.e., exhibiting both p-type and n-type conduction) can be created by using a metal with a work function that aligns at the mid-gap of the nanotube. Furthermore, to achieve sufficient tunneling rates, it is usually desirable to use a large-diameter SWNT, i.e., a smaller-bandgap SWNT for lower Schottky barriers. Applied gate voltage can shift the band energies up and down to make electrons or holes the majority carrier, leading to a “V” shape in the current versus gate sweep as seen in Figure I-7 (b). If electrons and holes are injected simultaneously, they could recombine across the bandgap and emit light. In principle, this process could be highly efficient because, as we have already seen, SWNTs have direct bandgap. However, in a conventional ambipolar CNTFET, there is little control over position-dependent carrier concentration within the channel, which limits our ability to improve efficiency. A position-specific electrostatic doping offered by a split-gate can overcome this limitation, which will be discussed briefly below, and is the topic of Chapter IV.

Figure I-9 also shows that the highest electric field regions exist next to the contacts. If injected carriers are accelerated to a sufficiently high kinetic energy, an additional inelastic scattering mechanism comes into play, i.e., creation of excitons by impact excitation. This means that even in unipolar transport, radiative recombination of excitons can occur under certain conditions. In the next section, we give a brief history of EL including both emission mechanisms in order to provide some background information for our work.

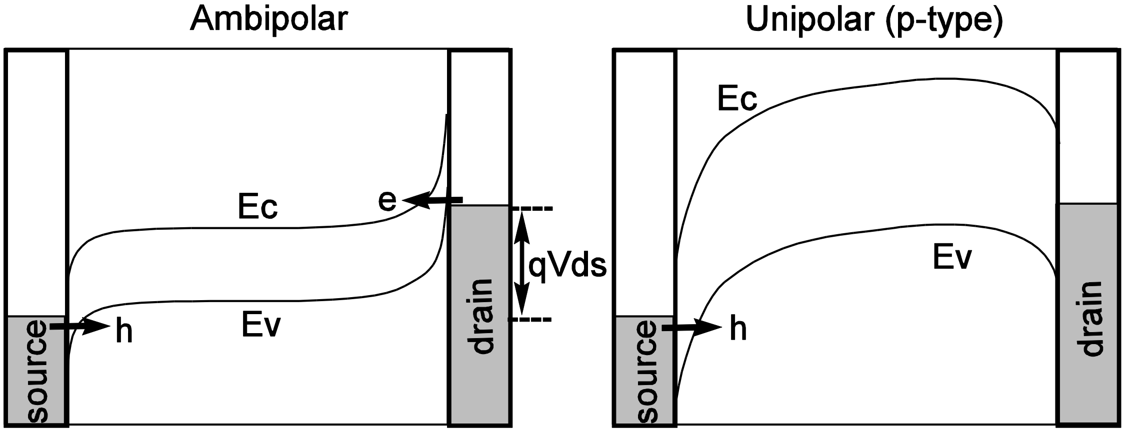

Figure I-9. Schematic illustrations of band structures in ambipolar and unipolar conduction. Note that the bandgap is smaller in the ambipolar case, allowing both types of carriers to be injected from midgap-aligned contacts.

6. Electroluminescence from carbon nanotube devices

The semiconducting CNT is a direct bandgap material with almost an ideal one-dimensional structure and high mobility; it allows us to study optoelectronics and photonics in 1D and is a promising material in developing an integrated nano-scale electronic and optoelectronic technology. In EL, excitons are created by electrical excitation of carriers, so the process is not restricted by dipole selection rules as in the case of photon absorption, and the momentum conservation requirement is also different. This means that states that may not be available to photo-excitation can be accessible by electrical excitation. From the technological point of view, CNTFETs could function as an integrated transistor and an IR light emitter or detector in an extremely compact package.

Emission from CNT devices involves (except for blackbody radiation) radiative combination of electron and holes, either as free carriers or bound in the form of excitons. Two basic mechanisms for creating electron-hole pairs in CNTs electrically are related to the transport mechanisms discussed in the previous section. Ambipolar emission refers to the case in which both positive and negative carriers are injected into the device from opposite contacts and combine radiatively in the channel. In contrast, in unipolar emission, there is only one type of majority carriers that gain enough kinetic energy in an electric field to impact-excite electron-hole pairs. Figure I-10 schematically illustrates the two different types of emission.

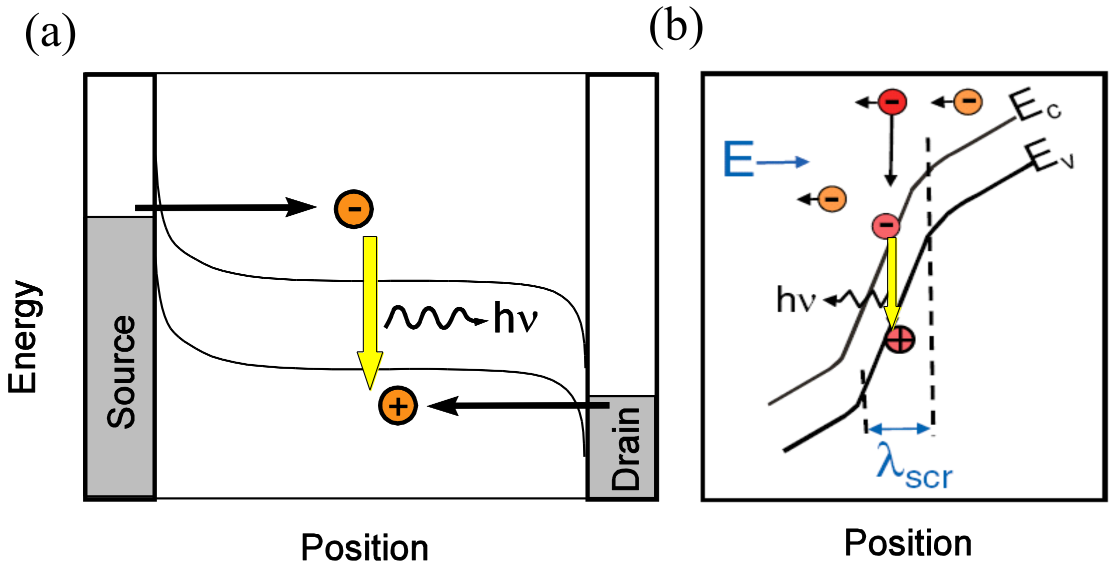

Figure I-10. (a) In ambipolar emission, carriers are injected from source and drain contacts through Schottky barriers. Some of them combine radiatively and emit a photon, as shown. (b) Unipolar emission mechanism. A carrier (electron in this picture) gains kinetic energy and creates an electron-hole pair, which in turn can recombine radiatively.

In the ambipolar case, the emission intensity is determined by the number of minority carriers since that limits the total number of pairs. To maximize the intensity, the gate bias should be one-half of drain bias in order to have a symmetric injection. In contrast, in unipolar emission (Figure I-10 (b)), one type of carrier (an electron in the figure) gains kinetic energy in a high electric field and excites another electron, creating an electron-hole pair. The pair recombines and emits a photon in some cases. The high field is typically created by structures that create sudden changes in potential along the channel, such as Schottky barriers, defects [1, 2], or structures such as a trench edge [71] or change in dielectric environment [72].

Observation of EL from a single carbon nanotube was first reported under ambipolar conditions in 2003 [73]. As we saw in Figure I-9 and I-10 (a), ambipolar devices inject electrons and holes from opposite contacts. By controlling the gate voltage, a specific region along the channel is created where electrons and holes coexist and can annihilate each other, some of which emit light. Misewich, et al. [73] found that the light intensity is maximum when $V_{GS} = V_{DS}/2$, that is, when the band structure is symmetrical with respect to the electrons and holes, so that they are injected at equal rates. The light intensity is governed by the number of minority carriers, since they limit the total number of electron-hole pairs that can be created per unit time. Therefore, the greatest recombination rate occurs when the numbers of carriers are equal and there is a region of strong concentration of both carriers.

Consequently, a later experiment using long-channel CNTFETs found that the ambipolar radiative spot can be physically moved along the channel by changing the gate voltage [74]. The size of the recombination spot was 1 μm (spatial resolution limit) or less, and a simple analytic model with drift transport was found to describe the phenomenon quite well [75]. Because carriers are injected directly, the quantum efficiency of the ambipolar emission can be calculated in a straightforward manner in the case of equal-rate injection. The EL efficiency was found to be 10^{-6} to 10^{-7} per electron-hole pair compared to the observed PL efficiency of up to 10^{-2}, and to depend on the type of nanotube and the channel length [76]. However, these numbers are not necessarily comparable since PL efficiency has been measured from tubes in solution or on suspended CNTs [77-79], unlike EL efficiency measured in on-substrate devices. PL from on-substrate single tubes is very difficult to observe because of the severe quenching due to the presence of the substrate. At this writing, the efficiency of PL on a substrate has not been quantified, and there is yet to be a study of EL from suspended CNTFETs in the ambipolar regime.

One way to improve efficiency is to electrostatically create p- and n- regions within the channel so that the recombination can occur at a well-defined p-n junction. Such a device was first demonstrated by Lee et al. in 2004 [80] using an embedded split-gate design, which remarkably showed a close to ideal p-n junction diode behavior. The device was consequently improved so that the SWNT was suspended, which showed the ideal p-n diode characteristics and enabled a photovoltaic investigation of the bandgap structure, excitonic transition states and bandgap renormalization from the electronic self energy [81-83]. A natural extension of this work was a single-tube carbon nanotube light-emitting diode, which was demonstrated by us in 2009 [11] and was shown to give a narrow spectrum (compared to conventional EL) and a quantum efficiency of about 10^{-4}, an improvement of two to three orders of magnitude over the conventional ambipolar emission. This work comprises Chapter 4 of this thesis, and will be discussed in detail.

There is another mechanism that can efficiently create electron-hole pairs in SWNTs, namely, impact excitation of excitons. This process is analogous to impact ionization in bulk semiconductors; a high-energy carrier goes through an inelastic scattering process to excite an electron from the valence to the conduction band, thus producing an electron-hole pair. Since only one type of carrier is necessary to impact-excite an electron, this type of emission can happen in a unipolar device. The large exciton binding energy because of SWNT's 1D structure means that the product of this scattering process is mostly excitons, not free electrons and holes. Perebeinos et al. found that the large Coulomb interaction in 1D results in a large enhancement of exciton production in SWNTs, about four orders of magnitude greater than in bulk semiconductors [84]. However, the process requires an initial electron with large kinetic energy and therefore relies on the existence of a large electric field to accelerate the carriers.

The first observation of light emission by impact excitation was reported on single SWNTs suspended over a narrow trench [71], where there was an abrupt change in the dielectric constant between the substrate and the vacuum at a trench edge. It was found that the light generated was about 1000 times brighter than in an ambipolar emission with comparable current, dramatically illustrating the efficiency of impact excitation in SWNTs. Localized emission due to high fields has also been observed at various heterogeneities that produce a potential drop, such as a change in the environmental conditions (i.e., PMMA vs. air), local defects, nanotube loops, and Schottky barriers. Emission from such localized spots was found to be more intense than the ambipolar emission from the same device [72]. Marty, et al. further investigated the dynamics of exciton formation and annihilation from unipolar emission, most likely from Schottky barriers [85]. These observations are of a fundamentally different origin than light emission from blackbody radiation observed in bundled multi-wall nanotubes [86], or from thermally excited carriers in metallic carbon nanotubes that can be understood by the Fermi distribution of hot (free) carriers [87, 88]. In suspended metallic nanotubes used in hot carrier emission experiments, the light originates from the center of the channel where the temperature is the highest[87, 89], in contrast to the light generation from CNTFETs, in which the emission is localized at Schottky barriers and other high-field regions.

Finally, we note the observation of EL from carbon nanotube networks. An array of many CNTs forming a thin film offers greater robustness than single-tube devices, and is more reproducible and consistent because of statistical averaging among the tubes. Thin CNT films and transistors made from such structures have garnered attention as a viable material in flexible and transparent electronics component with high mobility [90-96]. EL from a random network of SWNTs as a transistor device was first observed by Adam, et al. by ambipolar recombination of carriers [97]. The spectral analysis of the light emission revealed that it was preferentially generated in the largest diameter tubes in the sample; they found that convoluting the density of states and the Fermi-Dirac distribution of carriers reproduced the red-shift observed in the main EL peak relative to the absorption peaks. Their calculations show that the largest diameter tubes, though comprising only 4 % of their sample, dominate the EL spectrum.

The quality of CNTFETs was greatly improved by Engel et al., when they combined 99% purely semiconducting tubes produced by density gradient ultracentrifugation [98] and a CNT self-assembly technique from solution [99]; they succeeded in fabricating FETs from highly aligned CNT thin films with a high on/off ratio and a very low sheet resistance. The devices operated in ambipolar transport regime, and the EL from this material was also found to emit mainly from large-diameter tubes even at higher source-drain biases (V_{DS}). They attribute this to the fact that the current is carried preferentially in large-diameter tubes, and that excitons created in smaller-diameter tubes can decay into large-diameter tubes before decaying radiatively. This same material was used in the film LED experiment in this work that will be discussed in much more detail later.

EL has also been observed from an array of aligned SWNTs grown on a quartz substrate. It is possible to grow very straight and long carbon nanotubes that are aligned along a crystallographic plane of quartz. Zaumseil et al. achieved an efficient injection of carriers by using electrolytes instead of oxide dielectric, which enable a high capacitive coupling between the gate and the nanotube array grown on quartz [10]. They observed many ambipolar emission spots at relatively low source drain voltage ($|V_{DS}| < 3$ V) thanks to the efficient gating provided by ionic liquids. However, the calculated light emission efficiency is quite low ($\sim 10^{-9}$), although this may be partly due to the limits of detection. Another problem is the presence of metallic tubes in the array, resulting in high off-currents and poor on/off ratios. There is little control over the metallic/semiconducting ratio and the diameter distribution of aligned nanotubes grown on quartz, which remains a significant challenge not just on quartz, but in any carbon nanotube growth method. Therefore, the purified tubes employed by Engel, et al. and in this work are the most promising in device application to date.

7. Problems with carbon-nanotube optoelectronics addressed in this work

While carbon nanotubes are attractive materials for nano-scale optoelectronics, their practical use in application is still far from being realized, due to our limited understanding of EL mechanisms and unresolved challenges associated with the operation of CNT devices. PL studies have made some headway in understanding the excitonic nature of light absorption and emission, but the observations are from higher transition energies because of the ready availability of laser wavelengths in the visible range that is resonant with higher energy states, and also due to the difficulty of detection in the near infrared range below the silicon bandgap. In EL, lowest energy states are populated first, so the strongest emission is naturally from the E_{11} state. In addition, smaller-diameter CNTs (i.e., tubes with larger transition energies) create higher Schottky barriers, which impede electronic transport, so a certain diameter is required for electronic operation. We first tackled this problem by choosing just the right range of diameters and by using a specialized infrared camera that allowed us to detect energies as low as ~0.6 eV (see Methods). Chapter III analyzes transport and spectroscopic data thus obtained on the intensity, spectral shape and polarization of emitted photons, with the aim of understanding the characteristics of EL emission, such as carrier and phonon interactions, emission efficiency, and energy threshold for creating excitons.

Other significant problems in analyzing EL emission are its very broad spectral shape and the low emission efficiency. From the analysis presented in Chapter III, it will be apparent that the very operating principle of single-tube CNTFET is the main contributor to broadening. The broad spectral shape obscures different emission peaks and greatly reduces the signal-to-noise ratio in spectra, making data analysis very difficult, if not impossible. We solved this problem by creating p-n junctions constructed with single tubes, which is discussed in Chapter IV. By doing away with high electric fields at contacts and controlling the p- and n- junctions electrostatically, we were able to obtain narrow linewidths with high signal-to-noise ratios. A better control of injected carriers also resulted in a great improvement in emission efficiency. In addition, we also compared emission from a p-n junction and from a CNTFET using the same tube, which further provided evidence for broadening due to high electric fields in CNTFET.

From a practical point of view, single-tube devices have many shortcomings, such as the non-uniform wavelength of emitted photons from different tubes, and the lack of robustness of any single device. Since CNTs are actually a family of different structures which also come in metallic and semiconducting varieties with different energy gaps, controlling the output characteristics of a single-tube CNTFET or p-n junction is essentially impossible. Chapter V presents results from carbon nanotube film LEDs made of many aligned tubes that had been purified to be 99% semiconducting. Using such thin films made from almost-parallel CNTs has several advantages. Firstly, electric current per tube is greatly reduced, making it unlikely that individual tubes fail. And because of the presence of many tubes in a device, the device remains operational even if a few tubes fail, and the overall emission characteristic changes little. Secondly, statistical averaging leads to similar peak energy levels among devices for better uniformity. And finally, the total light output from a film device far exceeds that from a single-tube under similar operating voltages. For these reasons, CNT thin film devices are perhaps the most promising in terms of practical applications.

The history of EL from CNT devices discussed in the previous section shows that there is much we do not yet understand regarding emission mechanisms, and that there lies a great deal of challenge before CNTs can be used in commercial optoelectronics. In the following pages, we hope to contribute to a better understanding of EL emission from CNT devices and hence to better techniques for employing CNTs in applications.

Chapter II Methods

1. Materials

One of the most important characteristics of the CNTs for optoelectronic experiments is their diameter distribution since the E_{11} transition energy depends inversely on the diameter. Practically speaking, an appropriate distribution of diameters is required for the emission signal to fit within the measurement energy window of about 0.55 eV to 1.2 eV. This energy range approximately corresponds to the diameter range of 0.7 nm to 1.5 nm. The empirical data show that the transition energy actually varies a great deal depending on the chirality, not just the diameter [15], so it is likely that the practical diameter range extends further.

Of the several standard ways to determine the CNT diameter, transmission electron microscopy (TEM) is the most direct and accurate, but it cannot be conducted on a wafer surface. Atomic force microscopy (AFM) has a measurement error of at least 0.2 nm (about 0.5 nm for the AFM system that was available to us), too large a fraction of a CNT diameter to measure it to any useful precision. A more promising approach is to use Raman spectroscopy to determine the phonon frequency of the tube's radial breathing mode (RBM), which is inversely proportional to the diameter [37]. However, Raman signals, especially the RBM signal, are very weak from a CNT on a wafer surface (in contrast to suspended tubes), unless the laser excitation energy happens to be in resonance with the CNT's E_{33} absorption energy. This means that the excitation energy needs to be tuned while searching for Raman signals, which is a very slow and labor-intensive process. Given such limitations, it is not practical to determine individual CNT diameters in advance, so the samples were chosen on the basis of their statistically-known diameter distribution. Attempts to measure individual diameters by Raman spectroscopy afterwards were not always successful.

Several reliable methods have been developed to produce different types of carbon nanotubes (CNTs). For this work, the tubes used were grown using arc-discharge, laser-ablation and chemical-vapor deposition (CVD) methods. Of the three methods, laser ablation and arc-discharge produce bulk bundles of nanotubes in quantities of milligrams and even grams, while the CVD method grows individual nanotubes directly on a SiO_2 surface from catalyst particles.

The CNTs produced for this study were all known to be single-wall nanotubes (SWNTs) from their prior characterizations [100-102].

The arc-discharge method was the first one used in the discovery of CNTs [2, 3, 103]. It has since been improved to produce long, aligned bundles of SWNTs suitable for electronic and optical experiments at the single-tube level [100]. Liu et al. successfully synthesized ropes of high-quality SWNTs with the individual SWNT diameter of about 1.7 nm by creating a high direct-current plasma arc between two graphite rods with appropriate metal catalysts (nickel and cobalt) and a growth promoter (sulfur). The arc-discharge SWNTs used in this study were produced by the same group at Shenyang National Laboratory for Materials Science, Institute of Metal Research in China. Its diameter range was determined to be 1.8 nm to 2.2 nm by independent TEM measurements of tubes from the same batch.

Similarly to arc-discharge, laser ablation produces bulk bundles of CNTs. This technique utilizes continuous or pulsed high-intensity laser that ablates a carbon target containing metal catalysts (nickel and cobalt). CNTs form as the laser-evaporated carbon condenses in a 1200 °C furnace, and are then collected by an inert gas flow [102]. Van der Waals interactions cause the formation of bundled ropes that consist of hundreds of SWNTs each. The laser ablation sample used was synthesized at Rice University and consisted of the smallest diameter range of all the samples used. Statistics using the TEM have shown the diameters to be 0.6 nm to 1.5 nm, centered around 1.0 nm [56]. Using this sample, a large-scale study of CNT field-effect transistor (CNTFET) transport was conducted with three different contact metals, giving us a good electrical characterization of back-gated CNTFETs and better understanding of the role of the work functions of contact metals [56].

While the previous two methods produce CNT bundles which require chemical processing and sonication to be separated into individual tubes, the CVD approach allows for a direct growth of clean, spatially-separated CNTs on the substrate. Catalyst particles dispersed in solution are spun on a sample surface and heated in a tube furnace through which a hydrocarbon gas flows. CVD eliminates the need for sonication to unbundle individual CNTs, avoiding extra chemical and/or physical stress that could contribute to unwanted defects. Defects and chemical residues can significantly affect the properties of CNTs and could complicate the interpretation of experimental results. The CVD tube growth parameters had been tailored to grow small-diameter (< 2 nm) SWNTs at IBM T. J. Watson Research Center where all the devices were fabricated.

CNT film devices were made from laser-ablation grown bulk nanotubes dispersed in a surfactant (sodium dodecyl sulphate or SDS) solution. Via density gradient ultracentrifugation, the sample was purified to ~99 % semiconducting CNTs with a narrow diameter range [98]. The average length of individual tubes after the processing was about 1 μm. Stripes of individual tubes and bundles of ~10 μm width were self-assembled by a mechanical slip-stick process [99]. The SDS was subsequently removed by annealing at 600 °C for 60 seconds in argon. The sample used for this work had been assembled and processed previously for a CNT film FET study [99].

2. Device fabrication

i. CNTFETs

For single-tube devices, CNTs produced by laser ablation or arc-discharge method were suspended in 1, 2-dichloroethane by sonication at a medium power setting for about 30 minutes, which was found sufficient to separate CNT bundles into individual tubes. The resulting tubes range in length from sub-micron to ~10 μm, with the majority of them in the 1 to 5 μm range. The solution was drop-cast onto a highly p-doped Si wafer with a 100 to 300 nm thermally-grown SiO_2 layer. After waiting about 30 seconds for tubes to adhere to the surface by van der Waal forces, the extra solution was blown off by dry nitrogen gas. The solution concentration was adjusted until the surface density of the nanotubes imaged with an SEM was determined to be spatially separated, in the order of 10 CNT per 1000 μm^2. While the spatial resolution of the SEM does not approach nanometers, imaging at the accelerating voltage of 1 kV distinctly scatters electrons off of CNT surface and enables us to determine the placement of individual tubes.

Contact electrodes were written via standard electron-beam lithography. The distance between electrodes is 1 μm. Ti = 0.5 nm/Pd = 20~30 nm/Au = 20~30 nm were deposited via e-beam evaporation. The very thin Ti layer is used for adhesion and does not uniformly cover the surface, so the Fermi level of the metal depends on the work function of Pd, which is 5.22 eV [68] and is closer to the bottom of the energy gap for our sample. This makes the devices p-type because holes have a much thinner and lower Schottky barrier than electrons. The devices were annealed in argon or nitrogen at 220 °C for 10 minutes to improve contacts. The heavily-doped silicon serves as the back gate (see Figure II-1 for a device schematic).

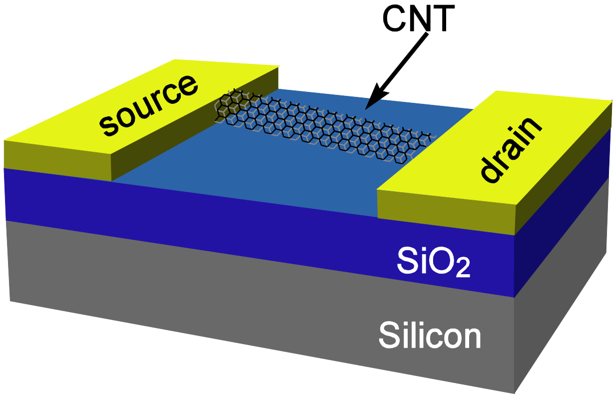

Figure II-1. Schematics of a back-gated CNTFET device. A CNT lies directly on the SiO_2 layer (thickness 50 to 1000 nm) grown thermally on a p++ silicon wafer. The source and drain contacts are separated by a distance of about 1 μm. The thickness of the layers is not to scale.

ii. Single-tube p-n diodes

The basic CNTFET design with added top split gates was used to create p- and n- regions electrostatically (figure 2). For p-n junction devices, Ti=50 nm was used as the contact metal to make the devices ambipolar, which is critical for efficient injection of p- and n- type carriers. The work function of Ti, 4.33 eV [68], makes the alignment with Fermi level roughly mid-gap.

CNTs were grown by CVD at 900 °C with the catalyst of iron oxide nanoparticles (diameters 3 to 4 nm) and ethylene gas as the feedstock. The process is similar to the one developed at Columbia University [101]. The tubes were grown on a highly p-doped silicon substrate with a 200 nm-thick thermal silicon dioxide layer. The tube density was kept low (~1 CNT per 1000 μm^2) to keep the CNTs spatially separated for single-tube devices and to prevent formation of nanotube bundles. After a Ti deposition by e-beam lithography for contacts, the devices were annealed in vacuum at ~100 °C and their FET characteristics were measured using the highly-doped silicon substrate as the back gate. Devices showing clear ambipolar behavior with a high on/off ratios ($> 1 \times 10^3$) were selected for further fabrication.

The top oxide is a 33-nm Al_2O_3 layer deposited by atomic layer deposition (ALD) which covers the entire sample surface. The dielectric constant of the ALD-deposited Al_2O_3 was determined to be $\varepsilon = 7.5$ by C-V measurements. In addition to acting as a gate oxide, this layer protects the tubes and allows for stable performance over a period of months. The top split gates were fabricated by another round of e-beam lithography. The recombination region width is about 1 μm, with the gated regions between 1 μm and 2 μm wide. Another lithography step defined windows over the large drain/source contact pads, and the Al_2O_3 layer was removed by diluted H_3PO_4 at 55 °C.

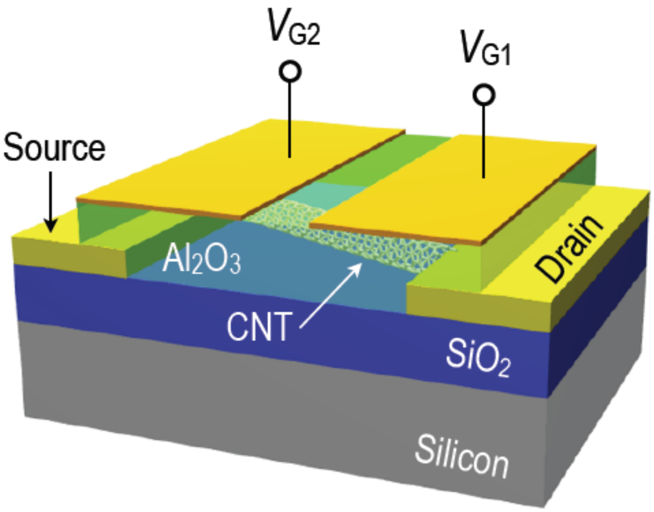

Figure II-2. Schematics of a CNT p-n junction. The structure is very similar to CNTFETs (Figure II-1), except the addition of the top Al_2O_3 dielectric layer (~33 nm) and the top gates. The source-drain distance used was typically 4 to 5 μm and the space between the top gates was approximately 1 μm.

iii. Film p-n diodes

The design of the film p-n diodes is the same as the single-tube p-n junction (Figure 2), except that there are multiple tubes and most of the tubes do not traverse the entire channel length so that carriers have to tunnel from tube to tube. Using the same CNT films as described in Ref. 99, we redesigned the gate stack to construct a split-gate configuration to create separate p- and n-doped regions along the transport channel. First, we identified film FET devices with clear ambipolar characteristics and the on/off ratio of at least 10^3. We used e-beam lithography to open 100 μm × 100 μm windows over the critical device areas. The existing single top gate (Al and Au) and the Al_2O_3 oxide layer were removed by wet-etching in H_3PO_4. The lithography to wet-etch process was repeated once to completely remove the Al_2O_3 layer because the PMMA layer tends to degrade after a time in the H_3PO_4 solution. We followed this process by a very brief rinse in a KI/I_2 gold etchant to remove residual gold particles, preserving only the CNT films and the metal (Ti = 1 nm/Pd = 40 nm/Au = 20 nm) source and drain contacts.

A new layer of Al_2O_3 = 33 nm was deposited over the same device area to serve as the top gate oxide. The top split-gate pattern was then defined by another round of e-beam lithography, and Ti = 35 nm was deposited by e-beam evaporation. The distances between the top gates were 1 to 2 μm, and the widths of top gates varied from 1.5 to 2 μm.

After the first round of measurements, many of the Al_2O_3 layers developed a significant leakage when the voltage bias between a contact and a top gate exceeded 15 V. Subsequently, the above process was repeated, but with a thicker Al_2O_3 layer (50 nm). In order to lift off the PMMA covered with a hard shell of 50-nm Al_2O_3, the sample was exposed to UV light (wavelength 252 nm) for 10 minutes in order to facilitate the breakdown of PMMA. The top split-gate metal (Ti=15 nm) was patterned and deposited by e-beam lithography and e-beam evaporation as before. The excessive processing seems to have degraded the film quality, judging from the transport and luminescent properties after the second time.

3. Experimental set-up

The optical path for detecting emitted light is schematically described in Figure 3. The sample was mounted on a sample stage with silver paint in an MRR vacuum chamber equipped with four probes. The stage and the probes were electrically connected to an Agilent 4145C parameter analyzer for applying voltages and measuring currents. The vacuum level in the chamber was typically 3 to 5 × 10^{-6} Torr.

Emitted light from samples was collected by a 10x, 20x or 50x Mitutoyo near-infrared (NIR) objective lens mounted directly above the sapphire view port on top of the chamber. Light then goes through a grating prism (GRISM) for spectroscopy, and/or through a linear polarizer for polarized measurements. The field lens mounted before the camera is used to keep the light path parallel through the GRISM and the polarizer. All the optical components are at ambient temperature before the light enters the detector through the outer window. The short-pass filters and the mercury-cadmium-telluride (MCT) chip inside the detector are cooled by liquid nitrogen.

For low-temperature measurements, a sample stage cooled directly by a small continuous-flow liquid helium cryostat by MMR Technologies was used in conjunction with an MMR K-20A Programmable Temperature Controller. The cold pad on the stage is equipped with a resistor heater and a temperature sensor. Liquid helium is pushed by the pressure in the dewar through a specially designed transfer line and into the cryostat. The sample stage can be cooled to about 20 K, but when the probe needles (connected thermally to ambient temperature through cables) are touching the sample, the temperature increases quickly and the practical low temperature measurement limit is close to 90 K.

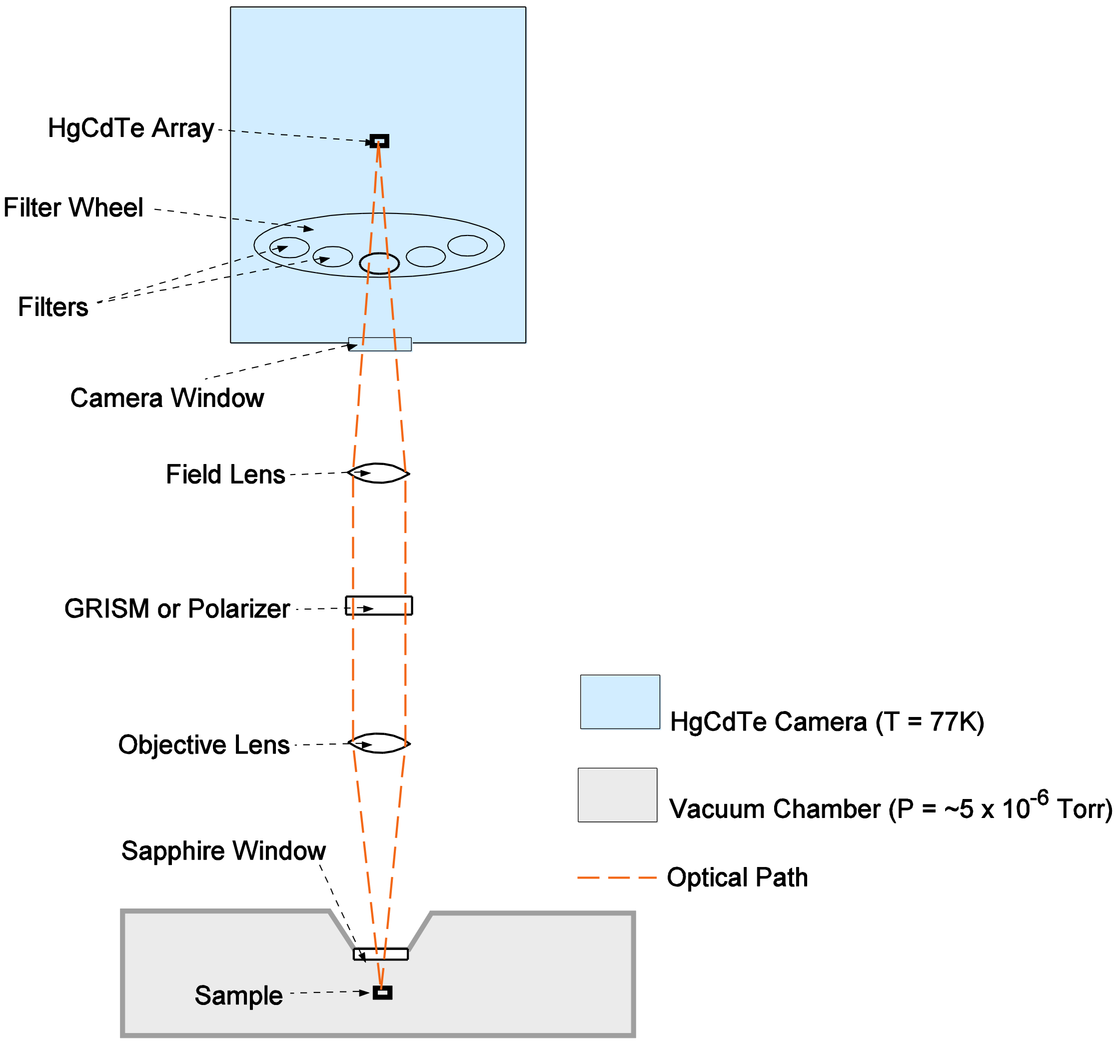

Figure II-3. Schematics of the optics to detect emitted light. The light path is indicated by the dotted line, which goes through various optical components (not to scale).

Emitted photons were collected by a mercury cadmium telluride (MCT) camera manufactured by Infrared Laboratories (Dewar 3592). MCT is a tunable semiconductor alloy whose bandgap depends on the relative amount of cadmium. The 256 × 256 pixel PICNIC IR array manufactured by Rockwell International was mounted in this detector and covers the spectral range of 800 to 2500 nm. The IR detector must operate at low temperature (~77 K) in order to minimize blackbody background radiation. In addition, short-pass filters with the cut-off wavelengths of 2150 nm, 2000 nm and 1800 nm were used to further improve the signal-to-noise ratio. It was found that most pixels on the array saturate after two seconds of integration with the 2150 nm filter. Hence, most measurements were taken with one-second integration time per frame.

The optical system was calibrated for the spectral-dependent transmission or efficiency of all optical components using a black-body source with a known temperature. Spectra were measured by dispersing a point-source emission spatially with the GRISM, which was calibrated by krypton and xenon light sources chosen for their strong spectral lines within the detection window. The resulting wavelength resolution was better than 7 nm, with a systematic measurement error no larger than 7 nm.

4. Electroluminescence measurements

The electrical transport and light emission properties were all measured in vacuum (~5 $\times 10^{-6}$ Torr) to avoid oxidation and burning of the devices at high current. Light emission intensity as a function of applied voltage was measured by sweeping the applied voltage slowly while the IR detector recorded photon counts frame by frame. The total sweeping time was typically about two minutes. Current was measured simultaneously and was synchronized to the photon measurement. Photon signals were integrated spatially from multiple pixels to account for any de-focusing or movement of the stage during the measurement. Finally, the background was subtracted from each frame against neighboring pixels without signals, and also linearly against the beginning and end frames without any applied voltage to correct for any drifting in the response of the chip.

For spectroscopy, it was often necessary to integrate the spatially (i.e. spectroscopically) dispersed signal across many frames in order to obtain a reasonable signal-to-noise ratio. The applied voltage was kept constant throughout the measurement period of tens to hundreds of seconds, while light image frames with one-second integration time were continuously taken. The current was also recorded throughout. Both the spectrum and the current were then averaged for analysis, and the background was subtracted from the spectral data in a similar manner as from the intensity data.

Polarized measurements were taken with a linear polarizer, i.e. a Glan-Taylor prism in the infrared, in the parallel section of the beam bath as indicated in figure 3. The polarizer was rotated normal to the beam path to specific angles with respect to the tube orientation. The CNT orientation was determined by an optical microscope (not shown in figure) using the metal contacts as reference and comparing them to an SEM image of the device.

In low-temperature experiments, the sample stage was first cooled down as much as possible (~20 K). For physical stability, the liquid helium transfer line was subsequently disconnected from the stage in order to mechanically decouple the measurement system from the environment. The probe needles were then lowered onto the contact pads, allowing the temperature to rise and then stabilize around 90 K for the first set of measurements. Since in this set-up, the temperature returns slowly to room temperature over several hours, it was possible to contact probe needles to the contact pads periodically to take a measurement at a given temperature. A resistor heater attached to the cold pad of the sample stage was used to raise the temperature when necessary. Only the sample stage was cooled, while the rest of the optical path remained at room temperature.

Chapter III Unipolar, High-Bias Emission

1. Introduction

Chapter I showed that both ambipolar and unipolar emission has been demonstrated with CNTFET devices [10, 71-74, 76, 85, 97]. In a sense, ambipolar emission gives greater experimental control; one can manage the relative electron and hole injection rates by setting the drain (V_{DS}) and the gate biases (V_{GS}) appropriately [74]. In contrast, in the unipolar scheme we do not know the electric field strength of an emission spot, or the distribution of carrier kinetic energy.

Nevertheless, certain features of ambipolar emission pose practical experimental problems that make it less appropriate for our purposes; to study the electrically-induced emission by investigating intensities and spectra from CNT devices and to build more efficient and robust devices. In order to have a symmetric device with respect to both carriers, the Fermi level needs to align mid-gap, and the device needs to be operated in the "off" state (i.e., at the bottom of the "V" shape in the gate sweep; see Figure III-3 for example) with a large source-drain bias in order to inject enough carriers. In addition, the radiative efficiency of electrical excitation has been shown to be about 10^{-6} at best [76].

Because of the high blackbody background noise from the optical components at ambient temperature (see Method), the long-wavelength limit of the detection window is around 2100 nm, or 0.590 eV. Ambipolar emission requires larger diameter tubes of at least 2 nm or larger for sufficiently thin Schottky barriers, and the corresponding E_{11} energy is around 0.55 to 0.56 eV or lower [15] which lies outside the detection window. In addition, a large source-drain bias means a large stress on the device, leading to heating and/or oxidation/destruction of the device. Since it needs to operate in the "off" state where $V_{GS} \sim V_{DS}/2$, it is difficult to pass large enough currents to obtain intensity-dependent spectra.

For these reasons, for this study the unipolar scheme was chosen where multiple electron-hole pairs can be created from a single injected carrier type. Since only one type of carriers needs to be injected, to facilitate transport the Fermi level of the metal can be aligned to either the conduction or valence band edge. In order to obtain emission intensity comparable to that from an ambipolar device, a larger bandgap tube and therefore a larger E_{11} energy can be used, bringing the lowest energy peak(s) into the detection window. The unipolar emission still requires a high gate and source-drain biases to create a high field within the channel; the emission threshold is typically in the order of 1 μA, often approaching the current carrying limit of CNTs at higher intensities required for spectral analysis. High fields and possible heating effects can become problematic, which we shall examine as part of the high-bias emission.

2. Experimental Results and Discussion

i. Unipolar Electrical Transport Characteristics

For spectroscopic studies, p-type CNTFET devices were created from laser ablation and arc-discharge tubes with a contact metal with a high work function (Pd). Figure III - 1 shows the drain current (I_D) versus the gate voltage (V_{GS}) of a typical p-type CNTFET device as the drain-source bias (V_{DS}) is increased in equal steps from curve to curve. All curves show an "on" behavior at a negative gate voltage, as the Schottky barrier becomes thinner for the valence band and holes are injected into the channel (recall Figure I-8 in Introduction). The total device resistance is in the order of ~10 MΩ at on-state, which is typical for a small-diameter semiconducting CNT device with Pd contacts [56]. The large hysteresis in the DC measurement is due to trap charges in silicon oxide, which is well known and was investigated recently in detail by pulsed characterization [104]. Our EL measurements were taken at a large enough gate voltage to be outside the hysteresis region. Note that for low V_{DS} (-1 V), the ratio of I_{on}/I_{off} is 4 to 5 orders of magnitude, but at a high V_{DS} the on-current saturates while the off-current increases so the I_{on}/I_{off} decreases as $|V_{DS}|$ is increased from 1 V to 7 V, indicating that the Schottky barrier is overcome somewhat even at the off-state at a higher $|V_{DS}|$.

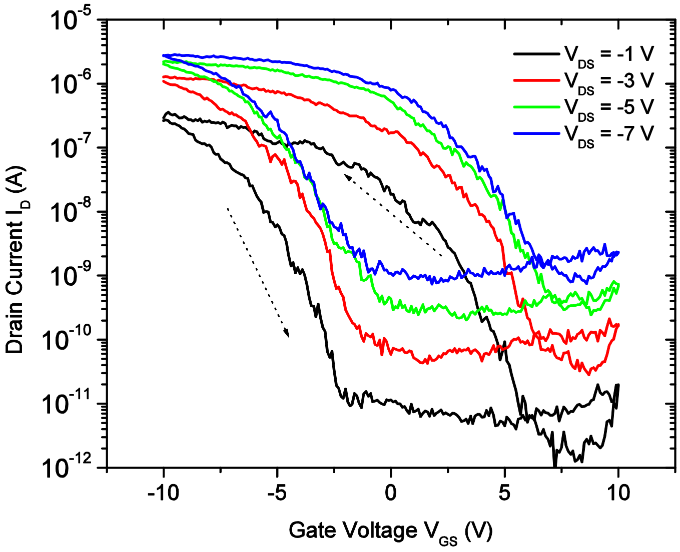

Figure III-1. Semi-log plot of drain current as a function of gate voltage at drain-source biases of -1 V, -3 V, -5 V and -7 V. The dotted arrows indicate the gate sweep direction.

In order to obtain sufficient signal-to-noise ratio, most of our light emission data is taken at a high source-drain bias, so the electrical transport is typically near or in the saturation regime, in the order of 1 to 10 μA. Taking measurements at saturation also makes the data more stable and reproducible because the results are beyond the influence of charge traps in the substrate. A typical saturation behavior of our devices is shown as a function of V_{DS} for different V_{GS} values in Figure III-2. Recall that for metallic SWNTs on a substrate, the saturation current is about 25 μA, while the saturation limit for semiconducting SWNTs depends on the diameter and work function of metal contacts [56] (note: large-diameter tubes have been shown to be similar to metallic tubes [55, 57]). Since we chose small-diameter (i.e., large Schottky-barrier) semiconducting SWNTs for this study, the saturation current varies significantly from device to device. Furthermore, since most of our devices are 1-2 μm long, acoustic phonon scattering (mfp ~ 300-700 nm) and even defects could further reduce the saturation limit.

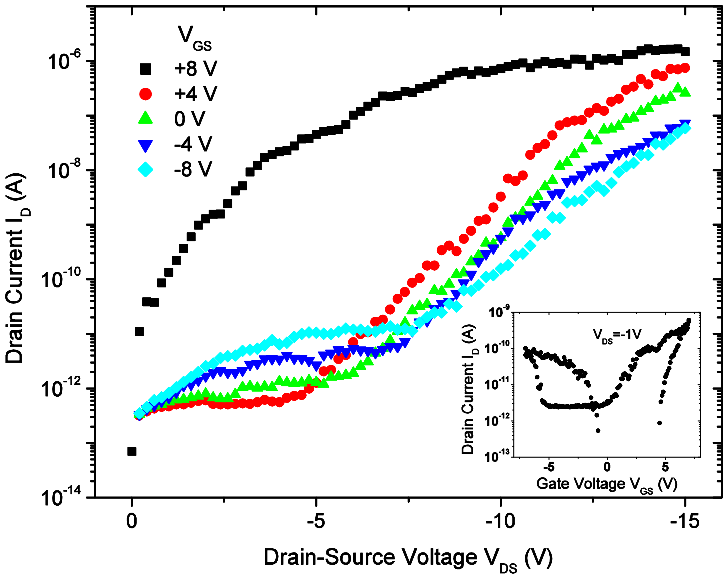

Figure III-2. Source-Drain sweep showing saturation at the current level ~1 μA. The device is mostly ambipolar with a stronger n-branch (inset). The saturation behavior is most clearly demonstrated when the device is in the "on" state (black squares).

It should be noted that the gate voltage dependence tends to change when the device is subjected to high-bias. Most notably, most of them change from p-type to n-type after passing a high current (Figure III-3). Although this phenomenon was not systematically investigated, the change typically lasts for days to weeks in vacuum (~10^{-6} Torr) and gradually reverts to p-type, suggesting that it is affected by adsorbed gas molecules from the environment.

Ohno et al. reported a similar change in transport from p-type to ambipolar after heating at 100 °C in vacuum for 24 hours [105]. They attribute this change to the elimination of adsorbed oxygen and the resulting change in interfacial dipole at the contact, which makes the Fermi level align mid-gap. This is also consistent with previous observations where charge injection occurs either directly into the traps in substrate or into the water molecules surrounding the nanotube and the SiO_2 surface [106-108].

In the current study, Pd was used as a contact throughout (with a very thin layer of Ti for adhesion and capped with Au to facilitate electrical contact to the probes) because of its good wetting with CNTs [57] and a relatively high melting point. The maximum current at a saturation gate voltage did not change significantly as a result of the change in V_{GS} dependence.

In addition, annealing by passing a high current makes the device more stable, so that the current characteristics are less noisy and more repeatable. Figure III-3 shows an example of the change from p-type to n-type FET as a result of passing a current close to 10 μA. Note that III-3 (a) corresponds to the same parameters as in Figure III-2, but from a different device. The n-branch in III-3 (a), i.e., the positive gate voltage side, shows higher current than in III-2, most likely because of the larger tube diameter (see caption). All our measurements at high biases were taken after a few rounds of high-bias (~10 μA) transport until the electric characteristics became stable from sweep to sweep.

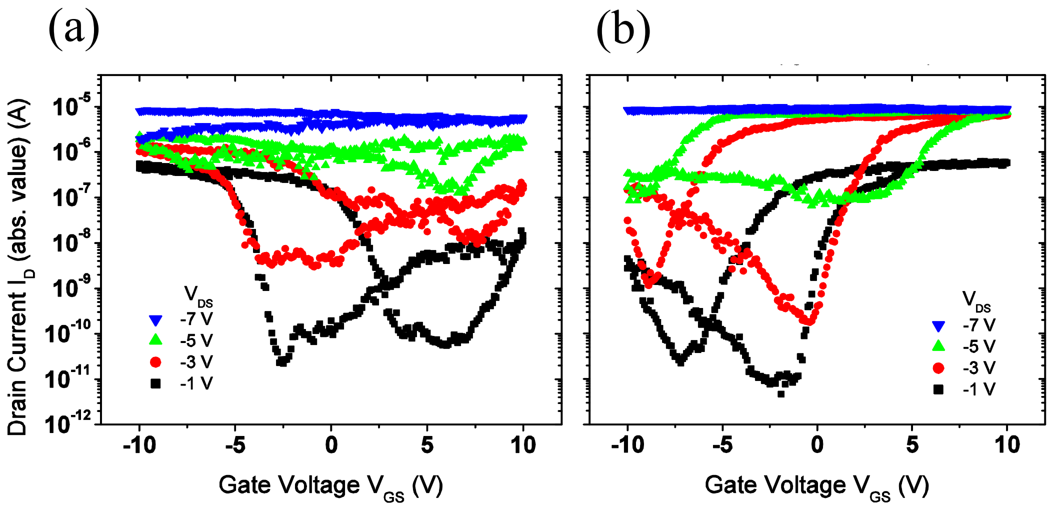

Figure III-3. Change in transport from predominantly p-type FET (a) to n-type FET (b). The sweep was conducted stepwise from -1 V to -7V as shown in (a), followed by the same in (b). This is a larger diameter tube as indicated by the metallic-like transport at V_{DS} = -7 V, and by the electroluminescence spectra in which the E_{11} peak is not observable because it is outside the detection range (not shown).

ii. Electroluminescence Intensity in the Unipolar Regime

Figure III-4 shows an example of EL intensity vs. photon energy as the drain bias is decreased stepwise from -5.0 V to -8.0 V while the device was in an "on" state by keeping V_{GS} at -7 V. One large, broad peak is observed around 0.7 eV that seems to be comprised of three or more different peaks (note the values 0.66 eV, 0.71 eV and 0.88 eV in the figure). The main peak is identified as the emission from E_{11} excitons, given the known diameter distribution of the sample. It also agrees with theoretical predictions [24, 25] and previous two-photon spectroscopy and photoconductivity experiments [26-28] that show that the dominant transition is from the E_{11} excitonic state.

Referring to the PL work by Weisman et al. [15], this E_{11} value suggests a CNT diameter of 1.4 to 1.5 nm, which is on the small-diameter tail of the distribution for this sample which has the average diameter of 1.8 nm. The precise (n, m) assignment is not possible from these data, given the unknown shifts under electric field and/or high temperature, broadening and the limited signal-to-noise ratio. Based on the comparison by Fritag et al. of PL and EL from a same tube [109], it is also likely that this E_{11} peak is already red-shifted from a field-induced doping by tens of meV with respect to the PL peak for the same tube. If this is the case, the corresponding diameter may even be slightly smaller. Most other devices from the same sample showed the main peak closer to 0.6 eV and even lower, sometimes not detectable because of the detection window cut-off (~0.56 eV), which agrees with the average diameter of 1.8 nm.

According to Ref. 18 and assuming the diameter of 1.45 nm, the energy gap (E_g)and the binding energy of E_{11} excitons for this SWNT are expected to be 0.95 eV and 0.23 eV, respectively, giving the E_{11} excitonic transition energy of 0.72 eV [15], which is also in agreement with the main peak position of this device within experimental uncertainty and differences due to dielectric environment. Note that the free-particle recombination peak at 0.95 eV is not detectable because the oscillator strength has been transferred to the excitonic E_{11} peak and because of the large broadening that obscures smaller peaks.

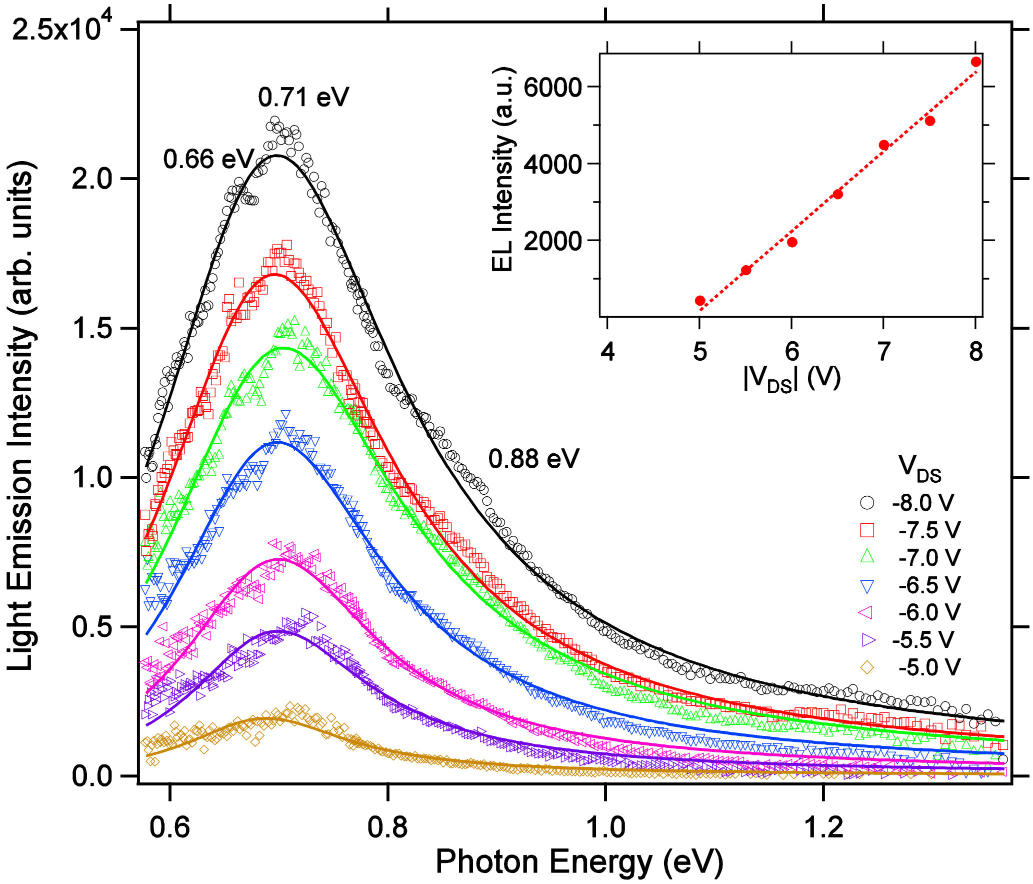

Figure III-4. (Main panel) Electroluminescence intensity as a function of emitted photon energy taken at V_{GS} = -7 V and V_{DS} = -5 V to -8 V in -0.5 V steps. Three peaks are identified with their energy (0.66 eV, 0.71 eV and 0.88 eV), with another very broad peak appearing above 1.2 eV. The fits are modified Lorentz distributions (see text) to account for the asymmetry. (Inset) Intensity of light emission integrated over intensity as a function of applied drain-source voltage (absolute value), shown with a linear fit. There is a threshold voltage (~5 V) below which no light is produced.

Figure III-4 inset shows the total intensity integrated over E_{11} energy from the main panel as a function of drain-source bias (V_{DS}). The emission intensity extrapolated to zero from a linear fit with respect to V_{DS} shows that there is a clear threshold voltage (4.9 V for this device) for light emission. This is most likely because of a combination of two effects: Schottky barrier and the threshold field (i.e., threshold kinetic energy) necessary for exciton production. First, a sufficient drain-source voltage is necessary to overcome the Schottky barriers at the injection site, and second, a high electric field must be created for exciton production.

Even when CNTFETs are in the on state, small Schottky barriers normally remain at contacts and the I-V_{DS} characteristic is not completely ohmic, especially for a small-diameter tube like the one shown in Figure III-5. In this device, which is made of the same SWNT as that in Figure III-4 but from a different segment, a non-ohmic transport behavior is apparent. The absolute value of the threshold voltage is below 2 V, followed by a linear I-V region. A decrease in slope occurs when the V_{DS} is between 3 and 4 V when the current approaches 10 μA, and then the conductance picks up again above V_{DS} = 5 V, a behavior similar to what was observed in Ref. 54. The low conductance (i.e., the small I-V slope) and the non-linearity below 2 V can be attributed to the resistance due to Schottky barriers. A very similar behavior is observed in the opposite polarity as V_{DS} is decreased from 0 V to -7 V, which indicates that the contacts are symmetric in this device.

It should be noted that virtually ohmic behavior within a small V_{DS} range is possible by choosing a larger-diameter semiconducting SWNT, appropriate choice of contact metals, and possibly some annealing. There remains a small intrinsic quantum resistance between the bulk contact and nano-scale SWNT (see Introduction and Ref. 59), but the resistance due to Schottky barrier dominates for our devices at a small V_{DS} value because of the small diameter.

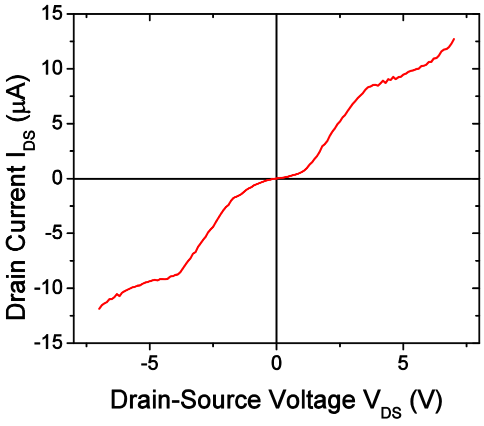

Figure III-5. Drain current (I_{DS}) as a function of applied drain-source voltage (V_{DS}) with the device “on”. V_{DS} was swept from 0 in both positive and negative directions. The device is with the same SWNT as Figure III-4, but from a different pair of source and drain contacts. The device channel length is the same as in Figure III-4.

By plotting the current as a function of V_{DS}, we can estimate the threshold drain voltage necessary to overcome Schottky barriers in this particular device, as in Figure III-6 for the data corresponding to the spectra in Figure III-4, and from which a ~3.5 V threshold voltage is inferred. The non-linear part as V_{DS} approaches zero was not recorded for this device, but is expected to resemble the non-linear behavior at small V_{DS} in Figure III-5.

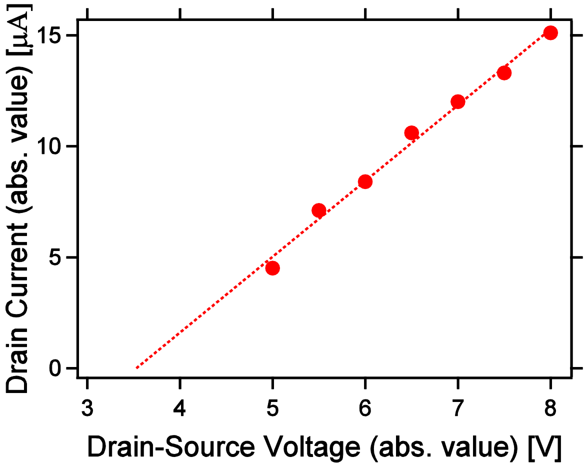

Figure III-6. Average current as a function of applied V_{DS} from the same measurement as in Figure III-4. Both have been converted to absolute values. The dotted line is a linear fit and is extrapolated to zero current to show the threshold voltage of ~3.5 V necessary to overcome the Schottky barrier.

Even though the current threshold is ~3.5 V, the light emission does not occur until $|V_{DS}| = 4.9$ V (see Figure III-4 inset), suggesting that the field strength does not immediately reach the critical value for impact excitation. The field needs to be large enough to accelerate injected carriers to a kinetic energy sufficient for exciton production. The threshold energy should at least be equal to E_{11}, but actually it is higher by a factor of ~1.5 because of the energy-momentum conservation requirement [110] and can be relaxed somewhat depending on the interaction with the environment such as the substrate [111]. Details of the field at Schottky barrier at various applied biases can be mapped by high-resolution photovoltage imaging [70], which is beyond the scope of this work. Given the channel length of ~0.5 µm for this device and the estimated threshold drain voltage of 4.9 V, the onset field is at least 10 V/µm, and most likely higher because the potential drop is not uniformly distributed across the channel in the presence of Schottky barriers. This estimation is consistent with the field strength of 30 to 60 V/µm for the onset of emission has been suggested for 1D CNTs by energetic considerations and optical phonon scattering length [71].

Once the emission threshold field is exceeded, it is reasonable to assume that the emission efficiency increases as the accelerating field is increased. In fact, as observed in Figure III-7 showing the integrated EL intensity as a function of current, a reasonable fit to the nonlinear behavior is obtained by using a polynomial function of the form $y = a + bx^2$. While the functional form of this fit cannot be discussed without knowing details such as the electronic temperature (i.e. Fermi distribution of the charge carriers) and the potential profile at the contacts, it still indicates that the emission is indeed more efficient at a higher V_{DS}, as the accelerating field is increased.

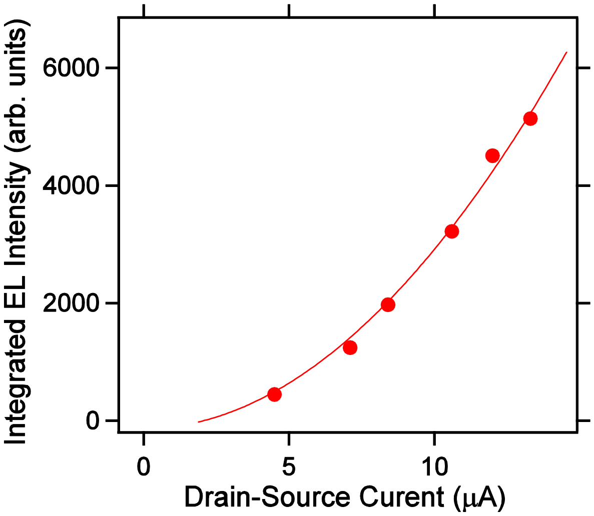

Figure III-7. EL intensity as a function of current. The best fit (solid line) is a polynomial fit with the exponent of 1.98 and no linear component.

iii. Electroluminescence Spectra

To understand the characteristics of electrically-induced emission in greater detail, we now move onto an analysis of the spectral shape. In particular, various peaks and their widths in emission spectra give clues to different mechanisms that influence the emission process. First, we examine the spectral width as a function of input power in order to elucidate the role of phonon temperature in broadening. Steiner et al. found phonon temperatures to be proportional to input power [112], and using this parameter also allows us to compare different devices with different I-V_{DS} characteristics. The spectrum in Figure III-4 is fit with a following equation,

$$f(x) = y_0 + \frac{A\{\Gamma[1+\eta(x-x_0)]\}}{\{\Gamma[1+\eta(x-x_0)]\}^2 + (x-x_0)^2} \quad \text{(Eq. III.1)}$$

where x is the photon energy. Equation III.1 is a modified form of the Lorentz distribution to account for asymmetry in the spectrum with the parameter η [113]. Γ is the equivalent of half-width-at-half-maximum (HWHM) in the Lorentz function. Figure III-8 shows the FWHM as a function of applied power calculated as the product of V_{DS} and I_{DS}. We find that a linear function fits the data reasonable well.

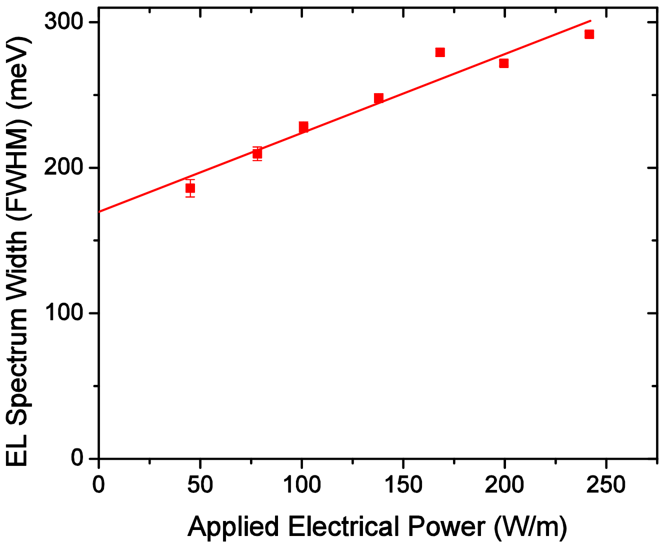

Figure III-8. Electroluminescence spectrum width as a function of power and a linear fit (solid line), showing a minimum width at zero power of 170 meV for this device. The vertical axis corresponds to FWHM(2Γ) from the fit shown in Figure III-4, which comes from Equation III.1.

One of the most salient characteristics of the spectrum is its broad width. In room-temperature photoluminescence experiments, the single-tube width is significantly smaller than k_BT (~25 meV) [114-116], which agrees with the low acoustic phonon scattering rate in CNTs. One would expect the width to be comparable to k_BT if the lattice temperature had a significant effect on the carriers. On the other hand, electroluminescence typically shows much larger widths[71, 73, 76, 85, 87, 97, 109, 111, 117], usually a factor of few larger than PL. When FWHM vs. power is fit with a linear equation and extrapolated to zero intensity (see Figure III-8), the minimum FWHM at zero power is almost 7 times wider than 25 meV, i.e., 170 meV for this device. Other devices also show a minimum width typically between 130 and 200 meV. Although Freitag et al. attribute the fivefold EL broadening compared to PL in their data to high-temperature electrons and phonons, they do not relate the broadening to the temperatures quantitatively. There are actually several possible contributions to the width, such as tube heterogeneity, phonon scattering, external electric field, exciton-exciton annihilation, electronic temperature, and blackbody background, just to name a few. Some of these contributions are now discussed semi-quantitatively.

The minimum width at zero power points to tube heterogeneity as one of the main contributions to the large width. When only a single peak is used to fit the spectra, the sharpness of the main peak is not reproduced by Equation III.1 (0.71 eV in Figure III-4 (a)), and this is always the case with any of our CNTFET EL spectra. This suggests that the “main peak” is actually a combination of multiple peaks that are broadened and combined to form one very broad shape, obscuring the contribution by each peak. By examining Figure III-4 (a) more closely, one can observe at least three peaks, at 0.66 eV, 0.71 eV and 0.88 eV. While the 0.66 eV is most easily seen at V_{DS} = -7.0 eV, it gets obscured somewhat as $|V_{DS}|$ is increased. From observations of double peaks in p-n junctions (see Chapter IV), this lower-energy peak is considered to be a weakly localized excitonic peak, possibly bound to local defect sites. This double-peak feature is discussed in greater detail in the section on single-tube p-n junction diodes where the peaks are observed more distinctly, but suffice it to say that this alone adds 50 meV (i.e., the difference between the peak positions) to the total width, provided that the two peaks are of comparable intensity. The energy difference was even higher in some devices, up to 65 meV.

It also needs to be noted that these peaks are unlikely due to the aggregation of multiple tubes in a bundle. As explained in the Methods section, bulk tubes (which are originally bundled) are sonicated for at least 30 minutes at a high power in dichloroethane before deposited onto the substrate, which is sufficient to separate them into individual tubes, as we have rarely found multiple tubes bound together in numerous AFM measurements and some Raman measurements of our devices. In contrast, very large widths are always observed and multiple peaks are observed very commonly in back-gated devices, suggesting that these are basic features that characterize single-tube, global-gate devices.

The small peak at 0.88 eV in Figure III-4, is observed in some devices, though not all. This peak is interpreted to be the signature of an exciton-optical phonon complex. The peak from optical phonon scattering has been directly observed in photoconductivity[27, 118] and photoluminescence[29, 30, 46, 119] experiments, and provides evidence for the excitonic nature of the dominant lowest-energy peak observed from SWNTs. The energy separation from the main peak (i.e., 0.88 eV – 0.71 eV = 0.17 eV) is somewhat smaller than the 0.18 eV observed in PL studies. However, the main peak is a combination of 0.66 eV and 0.71 eV peaks and the sideband is broadened from 0.88 eV toward lower energy (with possibly another peak around 0.85 eV), suggesting that the latter is also a combination of two optical phonon sidebands. Since we observe two main excitonic transitions at 0.66 eV and 0.71 eV, each one can have its own sideband due to optical phonon scattering.

The optical phonon sideband is also expected to be significantly broader than the main peak because finite-momentum phonons are allowed to contribute to the final excitonic zero-momentum state. The broad width of the absorption spectrum of optical-phonon sideband was indeed observed in a photoconductivity experiment [27], which is the opposite process of electroluminescence. This peak also adds to the asymmetry of the spectral peak as the broad "bump" between 0.8 eV and 1.0 eV.

Aside from optical phonons, exciton dephasing (i.e., changing of the k-state by inelastic scattering with phonons) by acoustic phonons can lead to broadening, as in the case of photoluminescence. Lefebvre et al. measured FWHM of PL spectrum on single SWNTs as a function of temperature, and obtained the linear relationship FWHM = 2 + 0.025T where the width is in meV and T is in Kelvin [115]. 0.025 meV K^{-1} is the coupling constant between acoustic phonons and excitons, which can be also expressed as 0.29 k_B where k_B is the Boltzmann constant. This value reflects a FWHM of the PL spectrum that is significantly below the thermal energy, k_BT, at least down to 50 K, which is expected from the expected weak coupling between acoustic phonons and excitons.

Yoshikawa et al. subsequently obtained the proportionality constant for many SWNTs in a PL experiment and found that this value is diameter-dependent [120]. They fit the FWHM values to the equation

$$FWHM = 2\Gamma_0 + AT + \frac{B}{\exp(\hbar\omega / k_B T) - 1} \text{ (Eq. III.2)}$$

where *A* and *B* are the coupling constants to low-energy and high-energy phonons, respectively. For the temperature range they used (≤ 300 K), it was found that *B* is negligible (i.e., same as the finding by Lefebvre above) and that *A* depends inversely on the tube diameter. They attribute the contribution to the widths in their data to low-energy longitudinal acoustic (LA) and twisting acoustic (TA) modes and rule out RBM phonons because of their higher energies. However, in our case the diameter range is at least 50 % larger, and the RBM phonon of the d = 1.5 nm SWNT has the RBM energy at the Γ point of only about 20 meV (calculated from the diameter-Raman energy relationship), well below room temperature. We do not have an estimate of the coupling constant *B*, but given the "average" temperature between 650 K and 750 K (see the following discussion) which is significantly above 20 meV, we proceed with the assumption that RBM contribution is similar to that of lower energy phonons and contributes linearly with power to the width.

It is reasonable to assume that in Lefebvre and Yoshikawa's work, the phonon modes were in thermal equilibrium, and that the temperature dependence was dominated by acoustic phonon scattering ($\hbar\omega_{ac} \ll k_B T$ at room T, which is the highest temperature used in their experiments). High energy phonon such as optical phonons (~180 meV) are not populated at room temperature (see Figure I-6 of the phonon dispersion relation in Introduction). Now we calculate the effective temperatures of acoustic phonons and apply the linear relationship to estimate their effect on broadening.

Steiner et al. measured effective temperatures of phonons under electrical bias and found that different phonon modes are *not* at an equilibrium temperature because of decay bottlenecks, and that each phonon mode's temperature was proportional to the applied electrical power [112]. They give the phenomenological expression

$$T_i = T_{sub} + P / g_i \text{ (Eq. III.3)}$$

where i is the phonon mode, T_{sub} is the ambient (substrate) temperature, the applied electrical power per unit length is $P = IV_{DS}/L$ (L is the channel length) and g is a parameter that depends on the phonon dynamics and the nanotube-substrate interaction. From a linear fit to their data, Steiner's group obtained the value $g_{RBM} = 0.11$ W m^{-1} K^{-1} for RBM phonons. Note that this is a phenomenological value and therefore includes all the mechanisms that determine the phonon temperature. Using this value and $T_{sub} = 300$K, and applying it to Equation III.2 with an A value of 0.018 meV K^{-1} (extrapolated from the data by Yoshikawa et al. [120]), we obtain the widths of 13 meV at $V_{DS} = -5$ V up to 45 meV at $V_{DS} = -8$ V, or 7 % to 15 % of the total width, respectively.

Note that "temperature" in this case is derived from the occupation number of a phonon mode as measured by the anti-Stokes to Stokes Raman intensity ratio. Since temperatures of different phonon modes are not at thermal equilibrium, there is no well defined lattice temperature at a given power, but this is a more intuitive and useful construct when discussing the energy exchange between hot carriers and phonons.

The acoustic phonon temperatures calculated as indicated above yield values ranging from 710 K to 2500 K, the higher end of which is unreasonably high for carbon nanotubes. In electrically-driven light emission experiments with suspended metallic or quasi-metallic SWNTs, Mann et al. extracted the hot optical phonon temperature of up to 1200 K in the negative differential conductance (NDC) regime [87]. Our devices are on the substrate and NDC behavior is never observed, so they should have a more efficient heat sink. Since hot optical phonon is the dominant scattering mechanism as evidenced by the NDC of their device, it can serve as the ceiling for the acoustic phonon temperature, meaning that it is very unlikely that our acoustic phonon temperatures are as high as 2500 K.

There are also indications that Equation III.2 significantly overestimates the acoustic phonon temperature under very high bias. In the study on phonon populations by Steiner et al., the high end of the power range was 40 W m^{-1}, and the linear fit to the RBM phonon temperature works only below 16 W m^{-1}. The temperature for electrical powers above 25 W m^{-1} shows a sign of saturation (Figure III-9).

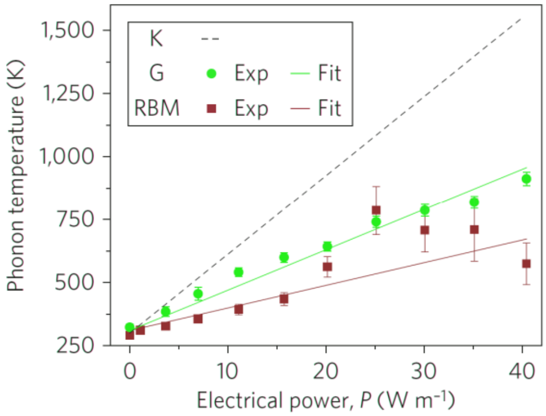

Figure III-9. The temperatures of three different phonon modes as a function of power measured by Steiner et al. K and G are zone-boundary phonons and optical phonons, respectively. Notice the saturation-like behavior for acoustic phonons (red squares) above 25 W m^{-1}. After Ref. 112.

Another clue that suggests temperature saturation in the higher bias regime comes from EL spectra of the high-energy E_{11} peaks (~0.8 eV, see Figure III-10) from two of our CNTFET devices. Judging from the energy of the main peak, the CNTs used for these have smaller diameters than that of Figure III-4. When the main peak is fit as Lorentzian and the background as blackbody, we can extract the temperature corresponding to the blackbody temperature that results from the heating of the nanotubes, which, we assume, represents the "average lattice temperature". Blackbody radiation from CNT heating has been reported by several groups (see, for example, Refs. [86, 121, 122]). Although there is no well-defined lattice temperature in our case because the phonons are not in thermal equilibrium, the kinetic energies of the carbon atoms manifested as the populations of different phonon modes must have an average value. The heating of the lattice results in the blackbody emission in the infrared. Although the dimensions of CNTs are outside the thermodynamic limit for the traditional bulk blackbody, it was recently shown that Planck's Law explains well the blackbody emission intensity of multi-wall nanotubes [121]. Therefore, we assume that this broad background is blackbody emission resulting from the "average temperature" nanotube lattice and investigate the temperature of acoustic phonons at power greater than 40 W m^{-1}.

The main panel of Figure III-10 shows the spectra of a device with a high-energy E_{11} peak that allows us to separate a broad background. The main E_{11} peak is seen on top of a featureless background of the blackbody emission whose peak is well outside of the detection window (0.3 eV at 700 K, for example). The inset shows that the “blackbody” temperature thus extracted falls in the range between low- and high-energy phonons at low power, but it does not increase significantly above 40 W m^{-1}. Furthermore, the effective phonon temperatures calculated using the g-values in Ref. 112 (see Equation III.2 above) are much higher than the temperature extracted from the blackbody spectra (dotted lines in Figure III-10). Therefore, we can assume that Equation III.2 significantly overestimates the contributions from the acoustic phonons to the widths *except* at the lowest-power limit (~45 W m^{-1}) of our data in Figure III-8. It is instructive to extract the experimental background contribution to the width; when the Lorentz width is subtracted, the background adds 17 to 48 meV to the total width for the four spectra with the highest V_{DS}. The three lower intensity spectra do not have a good enough fit to estimate this contribution. The large contribution at the highest bias (i.e., 48 meV) most likely is overestimated since it includes scattering by optical phonons, as seen by a red arrow indicating the exciton-optical phonon scattering at 1.0 eV in Figure III-10.

Given the above considerations, we estimate the acoustic phonon contribution to the total width to be about 20 meV at the lower end of our measurement (P = 45 W m^{-1}) and postulate that it increases only very moderately at higher power. It is unknown why acoustic phonon temperatures level off over 40 W m^{-1}, but the bottleneck in phonon decay from high-energy to low-energy phonons pointed out by Steiner et al. [112] may be a factor. Another strong possibility is the appearance of new decay channels for energy dissipation, such as impact excitation of excitons that give rise to EL. Perebeinos et al. calculated the rate of exciton production by impact excitation and found that once the threshold energy is reached, the pair production is expected to happen extremely fast (~ 1 fs) [84]. This extremely efficient electron-hole pair generation was also observed in a photocurrent experiment with a p-n junction [123]. This is especially interesting since the onset of EL seems to coincide with the beginning of the temperature saturation behavior. The direct temperature measurement of phonon modes at very high bias via Raman spectroscopy is yet to be conducted.

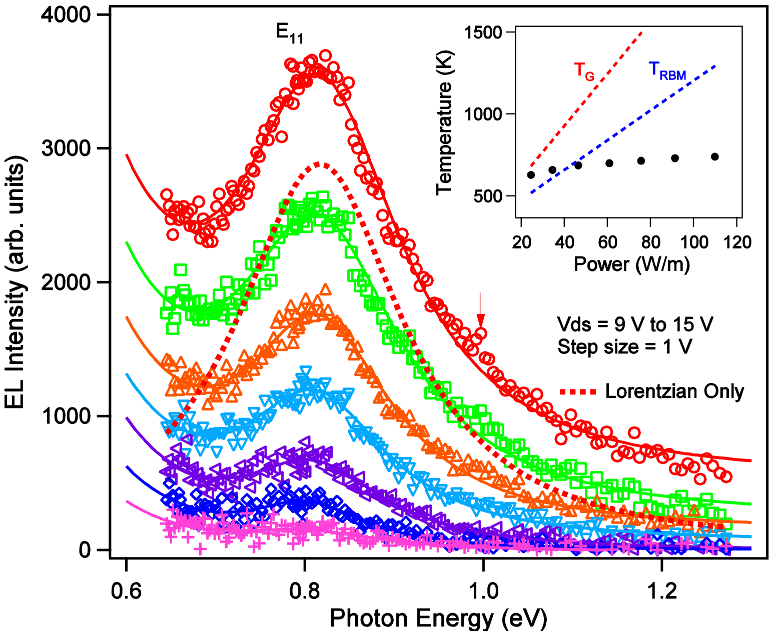

Figure III-10. (Main) EL intensity spectra at V_{DS} of 9 V (lowest intensity) to 15 V (highest intensity) in 1 V steps (empty symbols) as a function of energy. Solid lines are fit functions that are linear combinations of Lorentz and black-body distributions. The dotted line is the Lorentz function for the 15 V spectrum without the blackbody. (Inset) "Blackbody" temperatures as a function of applied electrical power (black circles). The blue and red dotted lines are the calculated effective temperatures of G-phonons and RBM phonons respectively, as in Ref. 115.

Tube heterogeneity and phonon scattering described so far (i.e., at least ~70 meV of the total 190 meV width at $P = 40\ \mathrm{W\ m^{-1}}$) explain the constant floor value of the broadening, but not its increase as a function of applied bias. The increase due to acoustic phonons seems to be modest at best, as explained above; contribution from merging with the broader optical phonon peak is also expected to be small because of the limited weight transfer to this side peak. Other possible broadening mechanisms that increase with applied bias are the effect of longitudinal electric field, the electronic temperature, and shortened lifetime of excitons by exciton-exciton annihilation.

Perebeinos et al. theoretically investigated the effects of longitudinal electric field on the absorption spectrum of SWNTs [124]. Using their formalism, we first calculate the broadening from lifetime shortening by exciton ionization due to an external field. We estimate the size of the effect following Perebeinos' formalism for the exciton dissociation rate as a function of electric field F (motivated by the solution to the hydrogen atom in an electric field),

$$\Gamma(F) = 4.1E_b \frac{F_0}{F} \exp\left(-\frac{F_0}{F}\right) \text{(Eq. III.4)}$$

where $F_0 = 1.74E_b^{3/2}m_{exc}^{1/2}/e\hbar$, and m_{exc} is a reduced exciton mass ($m_{exc}^{-1} = m_e^{-1} + m_h^{-1}$). Here we set $m_e = m_h$, from the symmetrical band structure in single-particle theory. We use $E_b = 0.23$ eV according to Ref. 18, and $m_{\mathrm{exc}} = \Delta/(2\ \upsilon_F{}^2)$ where υ_F is the Fermi velocity ($\sim10^6$ m/s), and Δ ($\sim$0.42 eV/d) is half of the single particle bandgap energy, yielding the F_0 value of 108 V/μm. Using the value of V_{DS} from Figure III-4 and assuming that most of the voltage drop occurs at the Schottky barriers whose length into the channel is in the order of the substrate thickness [125] (100 nm), we obtain Γ values of 54 meV to 171 meV for fields ranging from 25 to 40 V/μm, respectively. Figure III-11 compares the calculated broadening due to the field ionization with the experimental data to show that this effect can account for the change in width. The broadening calculated is actually 12 % greater than the experimental data. However, there is quite a bit of uncertainty in the length of the Schottky barriers, exciton binding energy, and whether the fields are equally distributed between the source and the drain. In our best estimate, we can conclude that the external field is a significant contribution to the spectral broadening.

When the recombination region is not subjected to very high fields, as in the case of ambipolar devices or p-n junction devices, an external electric field can mix the wave functions of exciton and the interband continuum states (i.e., free-carrier recombination) and still broaden the spectrum. The wave mixing also transfers the oscillator strength from the first excitonic state to the free-carrier state so that the latter grows as much as 400 % in strength at just 1/3 of the critical field for full ionization, according to the simulation by Perebeinos et al [124]. This type of broadening will be discussed further in the chapter on p-n junction spectra.

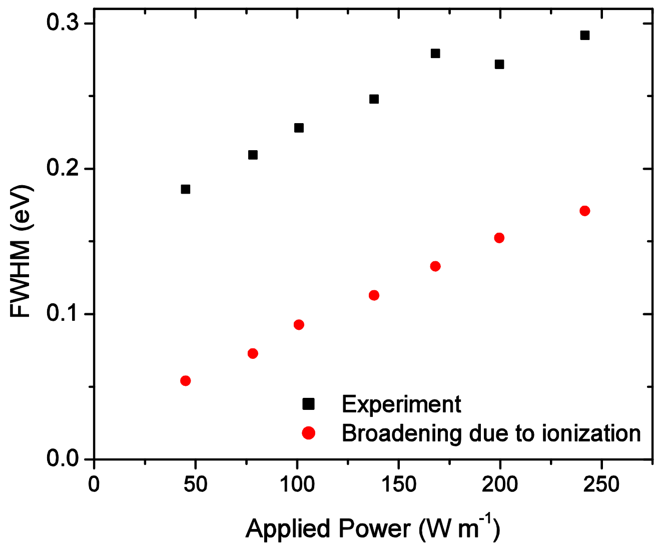

Figure III-11. Comparison between the experimental width (black squares) of the EL spectra in Figure III-4 and the broadening calculated from Equation III.3. Similar slopes indicate that the field ionization effect can account for the change in width.

Having accounted for the double peak, acoustic phonons and broadening due to field ionization, there is still about 60 ± 10 meV of broadening that needs to be explained. This value does not vary as a function of power; power-dependent broadening was already accounted for by the field effect. One possible effect is electron heating. If we follow the linear power-dependence demonstrated by Steiner et al., we arrive at extremely high electron temperatures, in thousands of Kelvin at high power. However, as it has been discussed already, it is likely that the phonon population saturates as the field increases over the impact excitation threshold. Scattering with surface polar optical phonons of the substrate has also been shown to be important as an energy dissipating mechanism [112, 126]. As a more realistic estimate, we can use the temperature of 1200 K in a suspended metallic nanotube as the upper limit of the optical phonon temperature, since this was observed in the NDC regime in Ref. 87. Steiner et al. also found zone boundary K phonons up to 1500 K, and G phonons close to 1000 K on the substrate [112]. We do not observe NDC in our data (see the linear I-V in Figure III-6), so we assume that the optical phonon population is not saturated as in suspended tubes, with the temperature < 1200 K.

As the applied power is increased, the electronic temperature should rise, unless the kinetic energy is dissipated via some other decay channel, which we claimed is the impact excitation mechanism. We have already cited temperature saturation as its supporting evidence. If the impact excitation mechanism is responsible for the lack of electronic temperature increase, that should result in an increase in emission per injected carrier. Figure III-12 shows that emission intensity per injected carrier (i.e., current) does increase almost to the third power as the applied power is increased, indicating that the EL efficiency is much greater at a higher power. If the 60 meV broadening is indeed due to electronic heating at a constant temperature, the figure is much smaller than reported by Freitag et al. where a five-fold broadening has been attributed to electronic heating. The difference, compared to our small electronic heating, is most likely due to the partially suspended nature of their device. Optical phonon saturation has been known to occur in suspended structures [87], leading to a higher electronic temperature in their device.

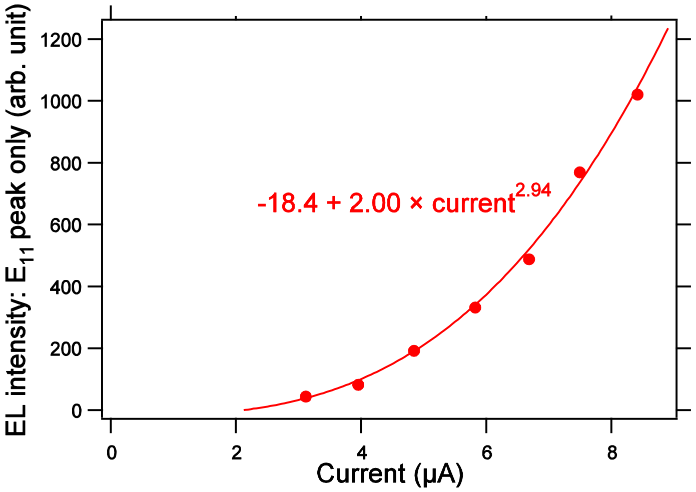

Figure III-12. Integrated Lorentz peak intensity as a function of current. The fit (solid line) shows that there is almost a cubic dependence on the current.

While the EL efficiency increase supports a constant in electronic temperature, it does not guarantee it (electron temperature can still increase in the presence of a greater EL efficiency), and we still do not know the actual temperature. A direct measurement of the electronic temperature, perhaps similar to the method used by Steiner et al. [112], is needed to investigate the degree of contribution to the broadening by electron heating.

Lifetime shortening due to exciton-exciton annihilation (EEA) also needs to be considered. EEA is an interaction process between excitons in which the excitation energy is transferred from one exciton to another, thereby annihilating the first exciton and making the other exciton a higher-energy exciton (from E_{11} to E_{22}, for example). Evidence for EEA in SWNTs has been observed in PL [127, 128] and femtosecond absorption spectroscopy [129]; a saturation in intensity and a sudden increase in the linewidth were observed in PL spectroscopy, for example [127]. Unfortunately, there are too many unknowns (such as the exciton generation rate by impact excitation and the optical phonon scattering rate) to evaluate quantitatively the contribution by this process in our devices. However, the lack of saturation in E_{11} and E_{22} intensity (Figure III-13 (a), inset) suggests that exciton-exciton annihilation is not a major contributor to broadening. Since this is a very fast process (800 fs at the linear exciton density of 2 μm^{-1} [127]) compared to the radiative exciton decay (10 to 100 ns at room temperature [33, 34, 78]) or nonradiative decay due to phonons (20 to 200 ps [130]), if there is Auger-type decay of excitons by another exciton, we expect to see its signature in the saturation of EL intensity, at least for the E_{11} peak (exciton-exciton annihilation of E_{11} excitons can populate the E_{22} peak), which is absent (Figure III-13 (a), inset).

Figure III-13 shows another device in which both E_{11} and E_{22} peaks are observed. As before, we assign E_{11} based on the diameter distribution of the sample and the fact that it is the main peak, and E_{22} from the position of the peak and the fact that it is the second dominant peak in the spectra. Also, the E_{22} peak intensity has a higher power threshold than E_{11}, as expected (see III-13 (a) inset). The energy ratio of E_{22} to E_{11} is about 1.8, similar to what has been observed in PL, which has led to the "ratio problem" discussed in the Introduction. E_{22} peak is broader than E_{11} peak, also expected from a calculation by Qiu et al [27]. E_{22} transition is expected to be much broader than E_{11} because of its coupling to the first free-particle continuum state. The weak peak appearing at higher V_{DS} between the E_{11} and E_{22} peaks is considered to be from the E_{12} and/or E_{21} transitions for the reasons we now examine in the polarization of the EL emission.

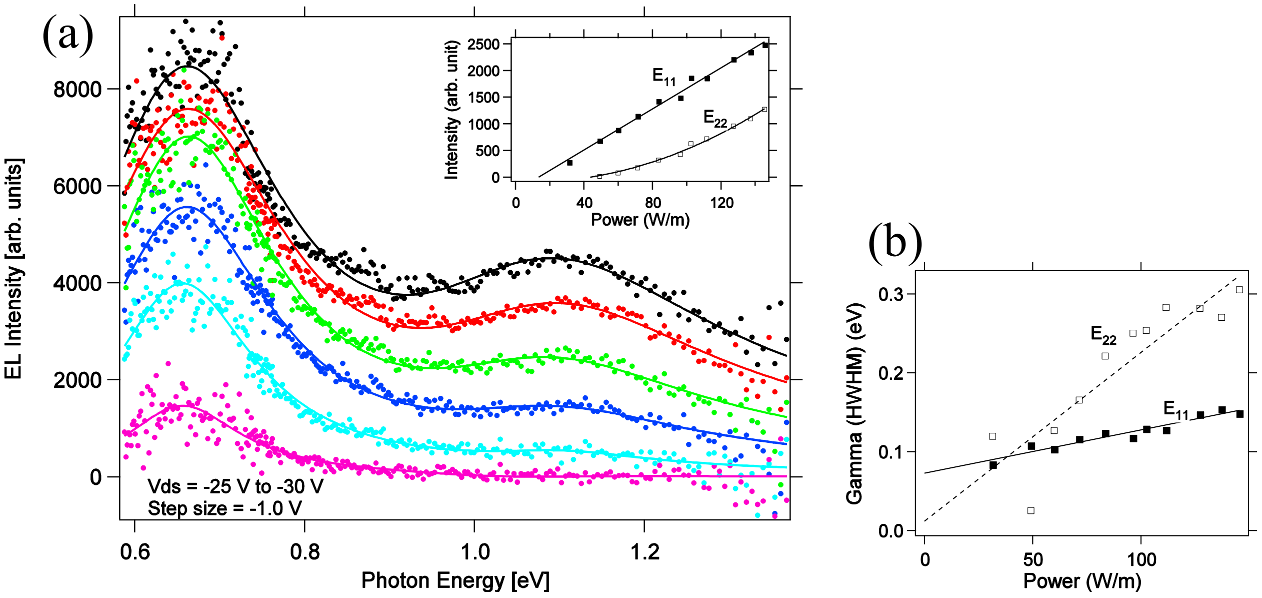

Figure III-13. (a) Spectra from a device showing E_{11} and E_{22} peaks around 0.66 eV and 1.10 eV, respectively. The solid symbols are experimental data which are fitted (lines) with a linear combination of two peaks from Equation III.2. (Inset) Intensity of individual peaks as a function of applied power. (b) Half widths of E_{11} and E_{22} peaks as a function of applied power.

iv. Observation of Polarization Effects in Electroluminescence Spectra

Polarization dependence of the absorption spectrum and emission in carbon nanotubes has been studied both theoretically and experimentally. While it was initially thought under single-electron theory that the absorption of "cross-polarized" light (i.e., perpendicular to the long axis of the tube) should be strongly suppressed due to depolarization [131, 132], a study considering excitonic effects revealed that there is a prominent absorption peak for perpendicular polarization, although it is still considerably weaker than in parallel polarization [133]. For parallel polarization (E_{11}, E_{22}, etc.), selection rules allow only transitions between same sub-bands, while cross-polarized light couples with non-equal sub-band transitions (i.e., E_{12}, E_{21}, etc.) [32].

The polarization dependence of light absorption and emission has been observed experimentally in CNTs. Lefebvre et al. has conducted spectral studies of PL and PLE for different polarizations [119, 134] and EL emission intensity as a function of polarization has also been measured experimentally [73, 87]. The results from the PL/PLE studies agree with the theoretical prediction that light in parallel polarization couples strongly with the E_{11} and E_{22} transitions, while the E_{12} resonance is observed in transverse polarization, although it is much weaker than the E_{11} and E_{22} parallel resonances [119, 134]. A photocurrent study has also shown the maximum excitation when the light is polarized along the direction of the nanotube [27, 135, 136]. However, there has never been a spectral study of polarization dependence in EL, which we now discuss.

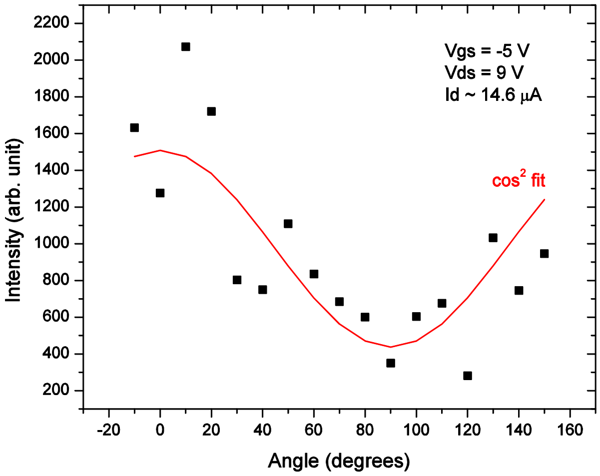

Figure III-14. EL intensity as a function of the angle between the tube direction and a linear polarizer. The ratio of maximum (0 degrees) and minimum (90 degrees) is 3.4 which is extracted from the fit. The large error is mostly due to the instability of the device.

Figure III-14 shows the polarization of emitted light intensity from a CNTFET. Because the channel length is much smaller than the spatial resolution of the equipment, the light appears as a point source and the polarizer transmits the component of the emitted light that aligns with the filter direction. The cosine squared fit gives a maximum (at 0 degrees) to minimum (at 90 degrees) ratio of about 3.4, which is similar to the observation of polarization in EL first reported by Misewich et al. in 2003 [73]. In terms of the degree of polarization (DOP), this translates to

DOP = $I_{\parallel} / (I_{\perp} + I_{\parallel}) = 0.77$. As we have already seen, EL emission is dominated by the E_{11} transition, so the maximum at zero degrees agrees well with theory. It is not completely suppressed at 90 degrees, which is also seen in single-tube PL and/or Raman [137], PLE [119, 134], and PC [27, 135, 136] measurements.

Now we examine the spectra through a polarizer placed in either a parallel or a perpendicular direction relative to the tube. The spectra in Figure III-15 are from the same device as in Figure III-10, where blackbody background could be identified. The most prominent characteristic of the emission is that the E_{11} peak is significantly polarized in the tube's longitudinal direction, as expected from theory. The analysis of E_{11} peaks (without the blackbody signal) from this device gives the range of DOP from 0.67 to 0.76, depending on the power (Figure III-15 (b), inset). The perpendicularly polarized component of the E_{11} peak is not zero; a detailed calculation of optical absorption for 29 different types of CNTs showed that the absorption profile with respect to polarization is highly dependent on the actual tube chirality [138]. Therefore, depending on the structure of this tube, there may be a relatively large perpendicular component of the E_{11} emission. It is also possible that the optical alignment has an error of a few degrees. Nevertheless, E_{11} emission in the perpendicular direction was significantly suppressed for the E_{11} transition in all the devices on which we conducted polarization-dependent measurement.

It should be noted that the blackbody background is also polarized, with a large component in the parallel direction (Figure III-15). This is due to the 1D structure of CNTs, and is consistent with the observation of incandescent emission from aligned multi-wall nanotubes by Li et al. [86]. They found that the emission from electrically heated nanotubes emits light that matches the blackbody radiation spectra very well, and showed via classical electrodynamics that electrons confined in a 1D structure emits light whose electric field vector is parallel to the direction of the said structure. This agrees with our observation that the blackbody radiation originating from the heating of the carriers and the nanotube lattice is also polarized.

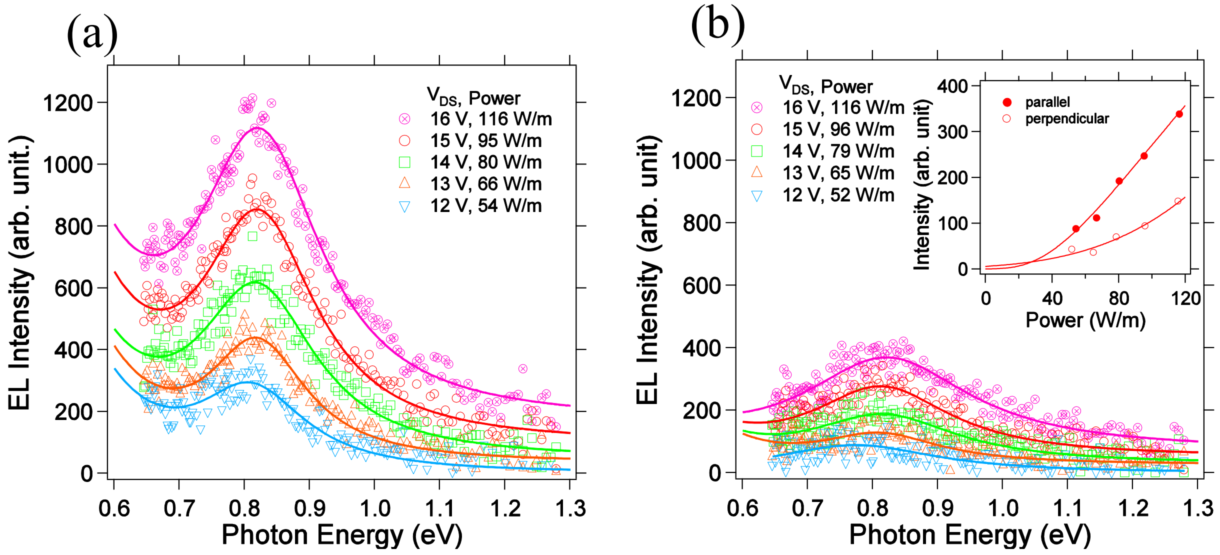

Figure III-15. EL spectra with a polarizer aligned along (a) and normal to (b) the tube direction. Symbols are experimental data and solid lines are linear combinations of Lorentz function and the blackbody spectrum, as in Figure III-10. (Inset) Integrated intensity of Lorentz peaks (without background) as a function of power. The fits are exponential functions.

As we have already seen in Figure III-13, there is evidence for the E_{12} (or combination of E_{12} and E_{21}) transition in some of our EL spectra when both E_{11} and E_{22} are observed. Since the E_{12} state couples more strongly to the perpendicular field and the E_{11} and E_{22} states to the parallel field, one should be able to observe the difference in relative intensities of these three peaks if the polarization is changed. We examined under polarizer the device used for Figure III-13, where there was a very weak emission peak about half way between E_{11} and E_{22} in the unpolarized measurement. The results are shown in Figure III-16 (a) and (b), with just the E_{12} peak extracted and normalized in panels (c) and (d). The E_{12} transition is clearly more prominent in the perpendicular polarization, though it is also seen very weakly in the parallel direction. Also, the overall intensity is weaker than that of E_{11} or E_{22}, as the depolarization effect of the perpendicularly polarized light causes the weak overall coupling between the E_{12} excitons and the light emission.

A large blue shift in the position of E_{12} in optical absorption is expected theoretically [19, 133], which has been observed in PLE experiments. Miyauchi et al. found a smaller exciton binding energy for perpendicular excitation than for parallel excitation, which is responsible for the blue shift [139]. On the contrary, in our data, no blue shift is observed in the E_{12} transition (Figure III-16 (b)). A theoretical work by Uryu et al. predicts a large blue shift of the E_{12} peak that depends on the strength of the Coulomb interaction in SWNTs [133]; their results show that in the absence of a strong Coulomb interaction, E_{12} is close to $(E_{11} + E_{22})/2$. In the PL measurements in which large blue shifts were observed in transverse polarization, the tubes were suspended structurally or kept in a surfactant suspension in order to reduce interaction with the environment. In contrast, our devices are directly on the substrate, which significantly increases the dielectric constant of the environment that screens the Coulomb interaction. In our analysis, $\varepsilon = 3.3$ is used which includes $\varepsilon = 3.9$ of the silicon oxide substrate. This significantly reduces the Coulomb interaction in the CNTs on substrate, which could account for the absence of a blue shift of the E_{12} transition.

Lastly, E_{12} and E_{21} transitions are degenerate in the single-particle framework, but this no longer applies if the asymmetry between valence and conduction bands are taken into account [140]. Miyauchi et al. has found about a 100 meV difference between the two peaks in perpendicular excitations [30]. However, as has been discussed, all excitonic peaks are significantly broadened and we are not able to determine whether what we consider the E_{12} transition is actually a double peak consisting of E_{12} and E_{21} signatures.

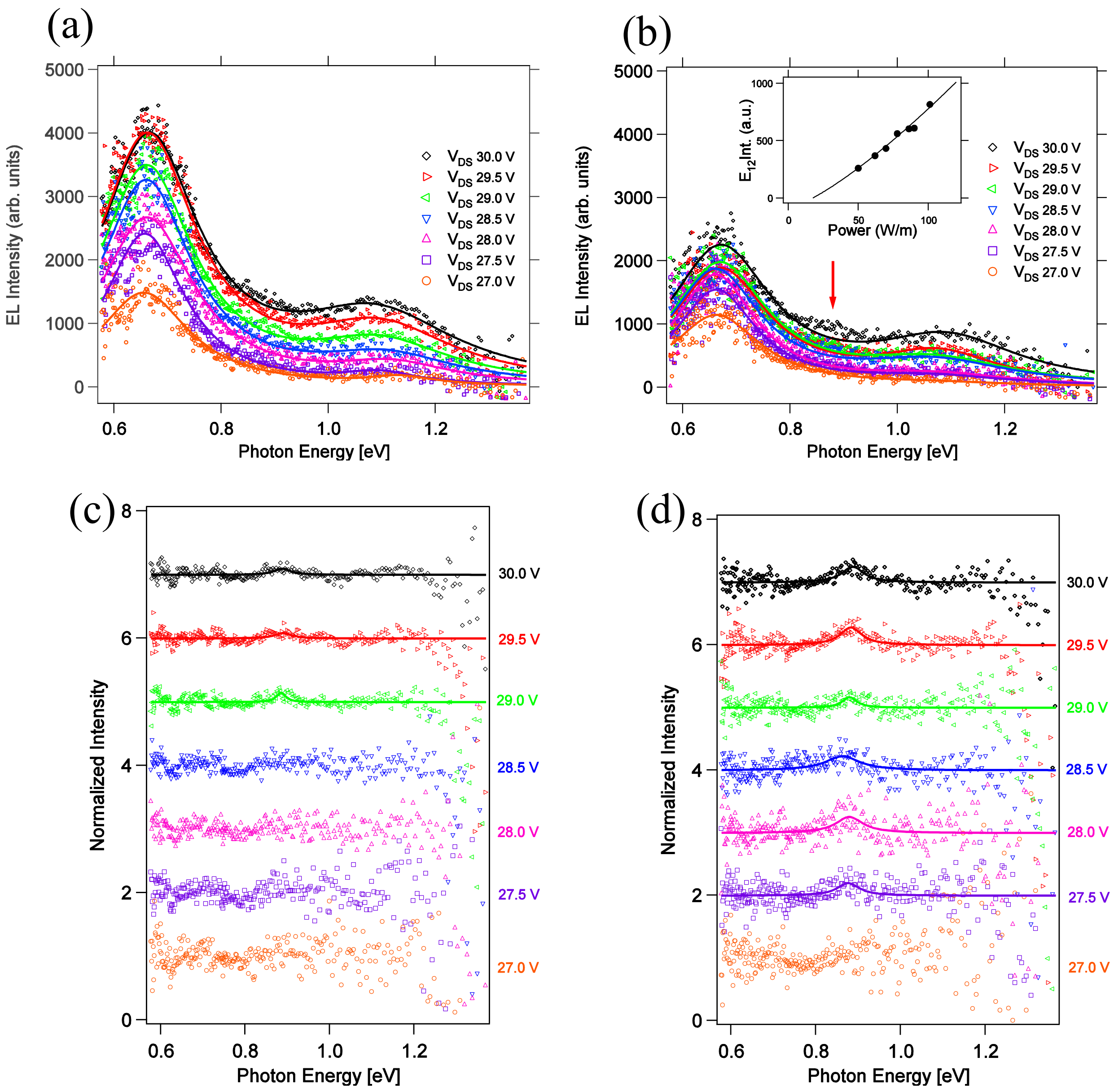

Figure III-16. EL spectra of the double-peak sample (same as in Figure III-13) through a linear polarizer (a) aligned with and (b) perpendicular to the tube direction, respectively. Note the arrow in (b) indicating emission from the E_{12} excitonic transition. (c), (d) Normalized EL intensity from the same data as from (a) and (b) with the E_{11} and E_{22} double-peak fit subtracted. Solid lines are lorentz fits. If there is no solid line, a reasonable Lorentz function could not be determined.

3. Conclusions

We have examined the intensity and spectral shapes of EL from single-tube CNTFETs. From transport measurements, it is seen that their electrical transfer depends on the control of Schottky barriers at metal contacts. In agreement with an impact-excitation process of exciton generation, a threshold behavior is observed at the EL onset. The very broad lineshape of the E_{11} transition is attributed to tube non-homogeneity, phonon scattering, electronic heating, and the effect of external electric field in the longitudinal direction. There is evidence that phonon temperatures (and with it, possibly electron temperatures) saturate at very high input power, possibly because of the energy dissipation by the EL mechanism.

We have observed E_{11} and E_{22} peaks, defect-mediated E_{11} peak, and the E_{11} - optical phonon side band complex. In polarized measurements, a clear suppression of E_{11} and E_{22} peaks is observed in the perpendicular direction. Conversely, we were able to observe the E_{12} transition for the first time in EL by investigating perpendicularly polarized component of the emission.

Our data point to possible future explorations that include phonon and electron temperature measurements, a more detailed investigation of the broadening mechanisms, and a realization of better signal-to-noise ratio for superior spectroscopic data. While polarized EL from CNT may have interesting applications in future nano-scale optoelectronics, there are many issues, especially in carrier and phonon dynamics and their interactions, that still need to be better understood.

Chapter IV Narrow-Band Electroluminescence from a Single Carbon-Nanotube p-n Diode

1. Introduction

In Chapter III, we have reported on the characteristics of EL from single-tube CNTFETs with a single, global back gate in the unipolar, high-bias regime. As we have seen, all electrically-driven CNT light-emitters with a single gate are operated under highly non-equilibrium carrier and phonon distributions. In those devices, high electric fields and currents are either an essential requirement for the light generation process [71, 85, 87, 97, 117], or an undesired side effect [73, 76], leading to high power requirements and low efficiencies. It is difficult to determine the quantum efficiency of unipolar devices that operate by impact excitation since we cannot determine the exciton generation rate, but the operative efficiency, defined as the number of photons emitted per injected carrier, is comparable to that of conventional ambipolar CNTFETs, i.e., 10^{-6} to 10^{-7}. As a result of large applied power, the EL linewidths are broad (80–300 meV, including the results presented in the previous chapter and in literature elsewhere), obscuring the contributions of the individual optical transitions. One way to overcome the above shortcomings is to use a p-n junction to create photons efficiently in a low electric field. In this chapter, we discuss electrically-induced light emission from individual CNT p-n diodes.

P-n junction diodes are fundamental to today's optoelectronic devices, such as photo-detectors, light emitting diodes (LEDs), and lasers. The demonstration of light emission from CNT p-n diodes is thus a fundamental step towards a possible technological use of CNTs as nanometer-scale light sources. A realization of CNT p-n junction was first achieved by Lee et al. as early as 2004 using embedded split-gate structure [80]. As illustrated in Figure IV-1 (a), two separate gate electrodes that couple to two different regions of a SWNT are used. One gate is biased with a negative voltage, drawing holes into the channel, and the other gate is biased with a positive voltage, resulting in an accumulation of electrons in that region of the channel. In this way, a p-n junction can be formed between the two and the devices behave very much like conventional semiconductor diodes. Indeed, Lee et al. showed that an ideal p-n junction transport can be achieved with CNT p-n diodes [80, 81].

In a split-gate scheme, a new level of control over electrical carrier-injection in CNTs is achieved, which allows device operation in a low-power-density regime (~0.1 W/m compared to ~10 W/m) with zero threshold-current, negligible self-heating, and high carrier-to-photon conversion efficiency (~10^{-4}). In this way, we have found that the EL spectra are significantly narrower (observable in our set-up down to ~35 meV) than those in previous studies, allowing the identification of emission from free and localized excitons. This phenomenon was discussed briefly in Chapter III and we now expand upon it with more detailed analysis that is made possible by the narrow linewidth of each peak.

2. Transport characteristics of the single CNT p-n diode

In Fig. IV-1 (b) we present the IV characteristics of a single SWNT diode under two different biasing conditions. The dashed green curve shows the drain-source current I_{DS} versus drain-source voltage V_{DS} when both gate biases are negative: $V_{GS1} = V_{GS2} = -8$ V. The tube then behaves as a p-type resistor and a symmetric, almost ohmic conduction behavior is observed. The deviation from a completely linear IV characteristic (dotted curve) at low V_{DS} is attributed to a voltage drop at the Schottky contacts between the metal electrodes and the CNT. This is analogous to the non-linear I-V_{DS} observed in Schottky-limited CNTFET devices at a low bias, as in Figure III-5. By applying gate biases of opposite polarity a p-i-n diode is realized. The solid red line in Fig. IV-1 (b) shows the IV characteristic recorded with $V_{GS1} = -8$ V and $V_{GS2} = +8$ V. The device now clearly shows rectifying behavior. The corresponding bandstructure is shown in Fig. IV-1 (c).

We found that in short devices (channel length < 4 μm), the diode behavior is often imperfect, with a leakage current on the "off" side. This happens because the formation of the doped regions is incomplete, i.e., Schottky barriers are most likely extending partially into the p- and/or n-doped regions. The solution is to either increase the channel length under the gates, or to improve the coupling between the split gates and the nanotube by employing a thinner and/or a higher-κ dielectric.

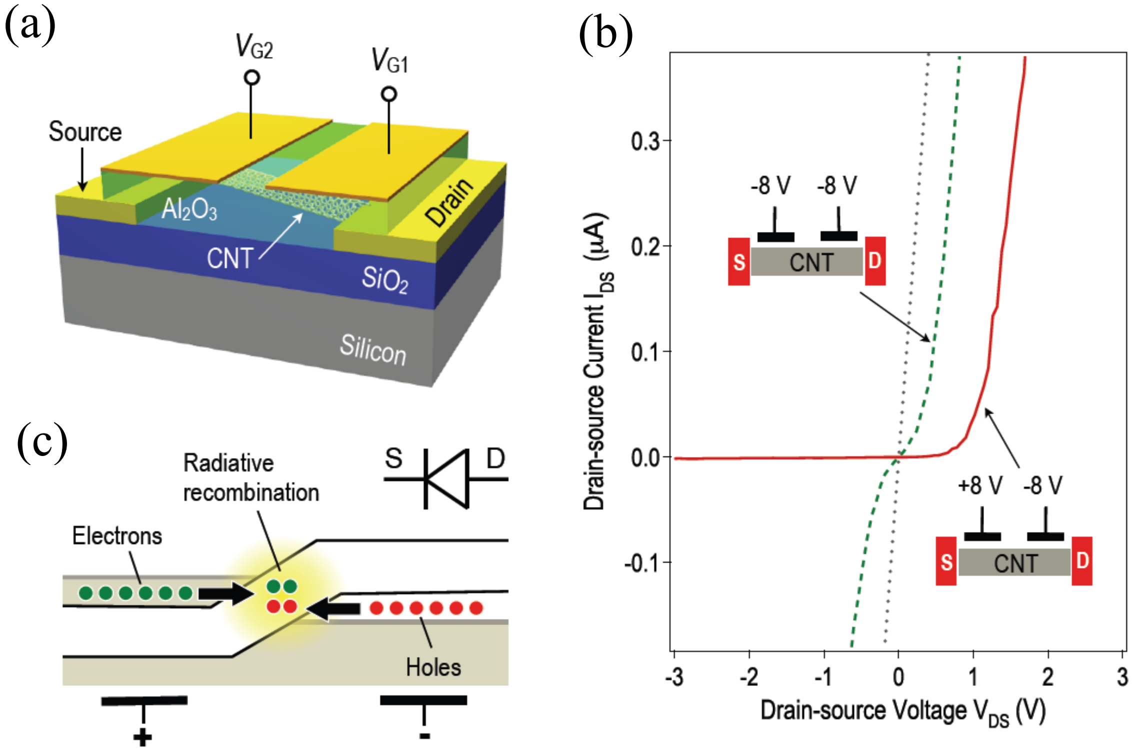

Figure IV-1. Device structure and electronic characteristics. (a) Schematic drawing of the CNT infrared LED. (b) Electrical device characteristics for different biasing conditions. Solid red line: V_{GS1} = -8 V, V_{GS2} = +8 V; The CNT is operated as a diode and shows rectifying behavior. Dashed green line: V_{GS1} = V_{GS2} = -8 V. The CNT behaves as p-type resistor. The silicon bottom-gate was grounded during the measurements. (c) Bandstructure of the CNT diode when it is biased in forward direction (V_{DS} > 0). Electrons and holes are injected into the intrinsic region and recombine partially radiatively and partially non-radiatively. After Ref. 11.

3. Electroluminescence mechanism and characteristics

The left image in Figure IV-2 (a) depicts the infrared emission from a device when the gate electrodes are biased at V_{GS1} = -8 V, V_{GS2} = +8 V and a constant current of I_{DS} = 240 nA is driven through the SWNT. As discussed in the previous chapter, electrically excited light emission from semiconducting CNTs can be produced under ambipolar [73, 76] or unipolar [71, 85] operation. In the former case, both electrons and holes are injected simultaneously into the tube and their radiative recombination generates light. In the second case, a single type of carriers, i.e. either electrons or holes, accumulate kinetic energy in a high-field region within the device to generate excitons by means of impact excitation [71, 84, 85]. The fact that no light is emitted when our devices are operated under unipolar conditions (V_{GS1} = V_{GS2} = -8 V; hole current) – right image in Fig. IV-2 (a) – shows that they are ambipolar light-emitters. This is the behavior we would generally expect an LED to exhibit. It is essential when fabricating devices that the back-gate sweep show a good ambipolar behavior (not shown), i.e., both types of carriers must be injected into the channel efficiently, in order for the devices to show this type of emission. Since the recombination rate in the ambipolar case is limited by minority carriers, this gives additional evidence for the ambipolar nature of our observation.

Figure IV-2 (b) shows that the emission intensity is proportional to the current (i.e. carrier injection rate), which also confirms that the device is operating as an ambipolar emitter. Recall that the EL intensity from impact excitation in unipolar emission grows as the second to third power of the current, as the increased field makes the exciton generation more efficient (Figure III-12). Moreover, the emission threshold with respect to the current is zero, and the signal is still detectable at I_{DS} as low as ~10 nA in many of our devices. This is in contrast to all previous EL studies [71, 76, 83, 111], where typically two orders of magnitude higher current levels are required to obtain light emission of comparable intensity. Moreover, the voltage drop across the intrinsic region is in the order of the bandgap (~1 V; see Figure IV-1 (c)), and therefore also 5–10 times smaller than in other devices, resulting in an up to 1000 times smaller power dissipation overall. Under typical operation conditions, we estimate a power density of only ~0.1 W/m in the tube, compared to 10–100 W/m in other devices. It is hence clear that the CNT diodes are operated in an entirely different regime from all other electrically-driven CNT light-emitters to date. In fact, the power density is comparable to what is typically used in photoluminescence (PL) experiments [6], and thermal heating, which strongly influences the EL of metallic as well as semiconducting SWNTs [87], does not play a role.

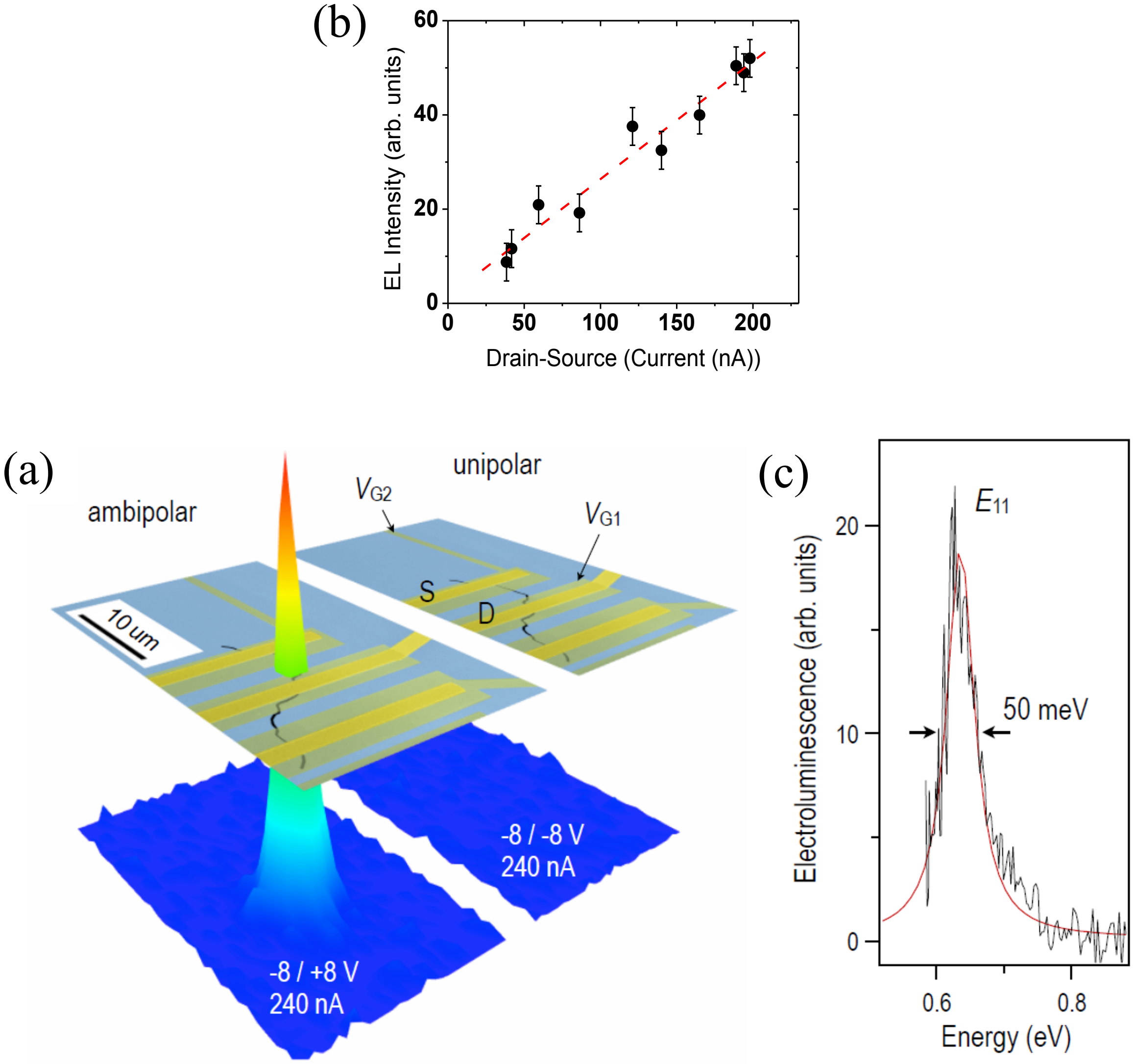

Figure IV-2. Identification of the light emission mechanism. (a) The upper plane is an SEM image of a CNT diode. The lower plane is a surface plot of the infrared emission. A microscopy image of the device (not shown) was taken under external illumination in order to verify that the emission is localized at the position of the CNT. Infrared emission is observed at the position of the tube when the device is operated as a LED (V_{GS1} = -8 V, V_{GS2} = +8 V; left image). In contrast, no emission is observed when a unipolar current of equal magnitude is driven through the nanotube (V_{GS1} = -8 V, V_{GS2} = -8 V; right image). (b) Integrated EL intensity as a function of current. The linear fit indicates that the mechanism is threshold-less and that the emission is proportional to the carrier injection rate. (c) EL spectrum of a SWNT diode at I_{DS} = 200 nA. The red line is a Lorentz fit. After Ref. 11.

After calibrating our detection system against the infrared emission from a known black-body emitter and taking into account its collection efficiency, we estimate an EL efficiency of ~0.5–1 × 10^{-4} photons per injected electron-hole pair. Given a radiative carrier lifetime of 10–100 ns in CNTs [33, 34, 78], we obtain a non-radiative lifetime τ_L in the order of a few picoseconds. This value is smaller than what is typically observed in PL measurements [130] (~20–200 ps). However, our value for τ_L appears reasonable because of the interaction with the environment and a higher concentration of carriers, both of which cause an increase of the non-radiative decay rate [141]. In normal PL measurements, the tube is suspended while our tube is directly on a SiO_2 substrate and is covered by a layer of ALD-deposited Al_2O_3, for the estimated dielectric constant of $\varepsilon_{eff} = 5.7$.

Fig. IV-2 (c) shows the spectrally dispersed emission of a SWNT diode at I_{DS} = 200 nA. It is composed of a single, narrow peak centered at ~0.635 eV, with a spectral width of ~50 meV. Note that this is much narrower than the widths discussed in Chapter III. Based on a correlation between the EL results with PL and Raman data [109, 142], we assign the EL peak to emission from the lowest-energy bright exciton state E_{11} in the CNT. The E_{11} designation is also consistent with the known diameter distribution of the sample (see also the discussion of E_{11} peak assignment in Chapter III).

Now we touch on the double-peak feature in emission spectra that was observed in many CNTFETs (Chapter III) and also evident in some of CNT diodes. We now have much narrower linewidth which allows us to analyze these two peaks quantitatively. In Figure IV-3 (a) we present the results obtained from another device. Besides the dominant emission at ~0.755 eV (labeled X), a weaker luminescence band is observed at ~65 meV lower energy (LX). We can rule out the possibility that X and LX are originating from two separate tubes in a multi-walled CNT. The small energy spacing translates into a diameter difference which is much less than twice the graphite lattice-plane distance. In order to further confirm that both emission peaks do not stem from a small bundle of CNTs, we characterized the tube by resonance Raman spectroscopy and atomic force microscopy (AFM). In the Raman measurements, we tune the excitation laser energy between 2.0 and 2.5 eV, i.e. across the E_{33}-range that corresponds to the diameter-range of our CNT sample. Only one single radial-breathing-mode (RBM), centered at $\omega_{RBM} \sim 200\ cm^{-1}$, was observed, from which the CNT diameter is determined to be [37] $d_t =$

$248/\omega_{RBM} \sim 1.24$ nm for this tube. From the AFM cross-section we extract a similar diameter. Those measurements, and the fact that double-peak spectra similar to the one in Figure IV-3 have also been observed in other devices, support our claim that both emission features originate from a single SWNT.

The two peaks in Figure IV-3 cannot be identified as the E_{11} exciton transition and the E_{11} continuum. The exciton binding energy that we estimate for a 1.24-nm-diameter tube embedded in SiO_2/Al_2O_3 ($\varepsilon_{eff} \sim 5.7$) is $E_b \sim 0.12$ eV [24], i.e. almost twice as large as the observed splitting. More importantly, the continuum transition carries only a small fraction of the spectral weight [24] (see also Figure IV-5). We can also exclude phonon-assisted emission, because of the different current-dependencies of the two peaks. Phonon assisted peaks are also not expected to be of comparable intensity to the main peak, and the energy separation does not correspond to any phonons that would couple strongly to excitons.

Low-energy satellite peaks have repeatedly been observed in PL measurements and have been attributed to localized exciton states [129, 130, 143-145]. We thus assign the peak X to “free” exciton emission and LX to emission from weakly localized excitons. It is not possible to determine from our optical measurements the physical mechanism of the exciton localization. It might be due to environmental fluctuations, leading to the formation of quantum-dot-like states, or brightening of intrinsic dark CNT states at structural defect sites. We note that in one of our devices, the low-energy emission feature LX was initially not present, but developed after stressing the tube by passing a high current through the device. This observation also supports the assignment of LX to emission from a defect site.

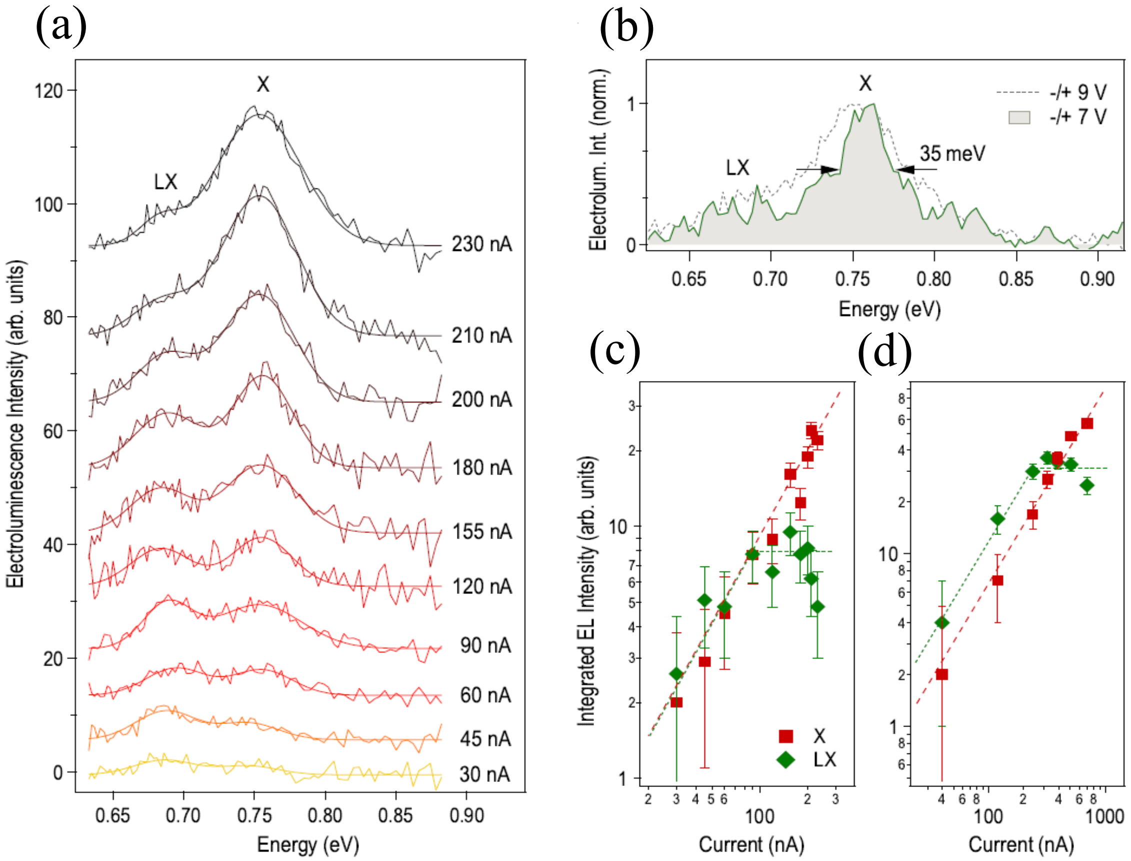

Figure IV-3. Electroluminescence spectra. (a) EL spectrum of a CNT diode recorded at different drain-source currents I_{DS} between 30 and 230 nA. Gate biases of V_{GS1} = -9 V and V_{GS2} = +9 V were applied. The data can be fitted well with two Gaussians and, at low currents, we extract widths of ~45 meV (FWHM) for the individual contributions. Besides the strong exciton emission (labeled X), a weaker satellite peak at lower energy is observed (LX). It is attributed to localized exciton emission. (b) Comparison between EL spectra at two different gate biases (normalized). Solid green line: V_{GS1} = -7 V, V_{GS2} = +7 V; dashed grey line: V_{GS1} = -9 V, V_{GS2} = +9 V. The spectral width of the -/+ 7 V measurement is only ~35 meV (FWHM). (c) Red symbols: The free exciton emission (X) shows an approximately linear increase with current. Green symbols: Localized exciton emission (LX). The EL saturates as the current exceeds ~100 nA. The EL versus current dependence shows no threshold behavior (see also Figure IV-2 (b)). The dashed lines are guides to the eye. (d) Same as (c), but for a different device. After Ref. 11.

Figure IV-3 (c) depicts the current dependence of the X and LX emission intensity as extracted from Figure IV-3 (a). The free exciton emission X shows a linear increase with current (see also Figure IV-2 (b)). This is in contrast to previous studies of EL from CNTs [71, 73, 76, 85, 87, 97, 111, 117], which exhibit current thresholds of >1 μA for light emission. The CNT diodes thus constitute threshold-less nano-scale light-emitters. The localized exciton LX also rises linearly at low currents but saturates as the current exceeds ~100 nA. Saturation of exciton emission in CNTs is a characteristic signature of Auger-mediated exciton-exciton annihilation [79, 129, 146], which is known to be strongly enhanced in tightly confined 1D systems [147]. It sets in when more than one exciton is present in the tube, i.e. when the electron-hole pair injection rate $I_{DS}/2q$ (q is the electron charge) exceeds the inverse carrier lifetime τ_L^{-1}. Therefore, $\tau_L = 2q/100\ \mathrm{nA} \sim 3$ ps, which is in agreement with the τ_L estimated from the EL efficiency above. The sudden saturation further suggests that $\tau_A^{LX} \ll \tau_L$, with τ_A^{LX} being the LX–LX annihilation lifetime. From the absence of any noticeable X saturation, on other hand, we expect the X–X annihilation lifetime τ_A^X to be much longer than τ_L. In fact, following Ref. [147], we estimate ($E_b = 0.12$ eV, $E_g = 0.755$ eV + E_b) $\tau_A^X \sim 12$ ps. The fact that the emission from defect sites is of comparable strength as the emission from the rest of the tube further points toward a strong exciton nucleation (i.e. locally increased exciton density) at the low-energy defect sites. Figure IV-3 (d) depicts the results from another device. A similar behavior is observed, but the onset of saturation now occurs at higher current (~250 nA), suggesting a higher concentration of defects in this tube. This is also consistent with a ~2 times stronger LX emission as compared to X emission at low currents. It might also be interesting to investigate the photon statistics of the LX emission using a time-resolved technique, since it is believed that exciton localization plays an important role in the generation of quantum light from CNTs [129].

Upon decreasing the gate bias voltages from -/+ 9 V to -/+ 7 V, the doping in the CNT p- and n-regions decreases and so does the infrared emission intensity (for same V_{DS}). However, as shown in Figure IV-3 (b), we also observe an even further reduction of the spectral width. We now extract a linewidth of only ~35 meV (FWHM). This value is ~2 to 8 times smaller than what has been reported in all previous EL measurements to date [71, 73, 76, 85, 87, 97, 111, 117], and approaches that typically observed in room-temperature PL [6] (~25 meV). Figure IV-4 shows more detailed statistics of X and LX peaks from another double-peak device. From IV-4 (b), the slope of the fit for both X and LX widths extrapolate to ~ 30 meV at 0 V drain-source bias, comparable to the values above. The increase in width with V_{DS} is roughly equal in magnitude to the increase observed by increasing the V_{GS} values, although a large uncertainty in both peaks does not allow us to draw conclusions from quantitative analysis.

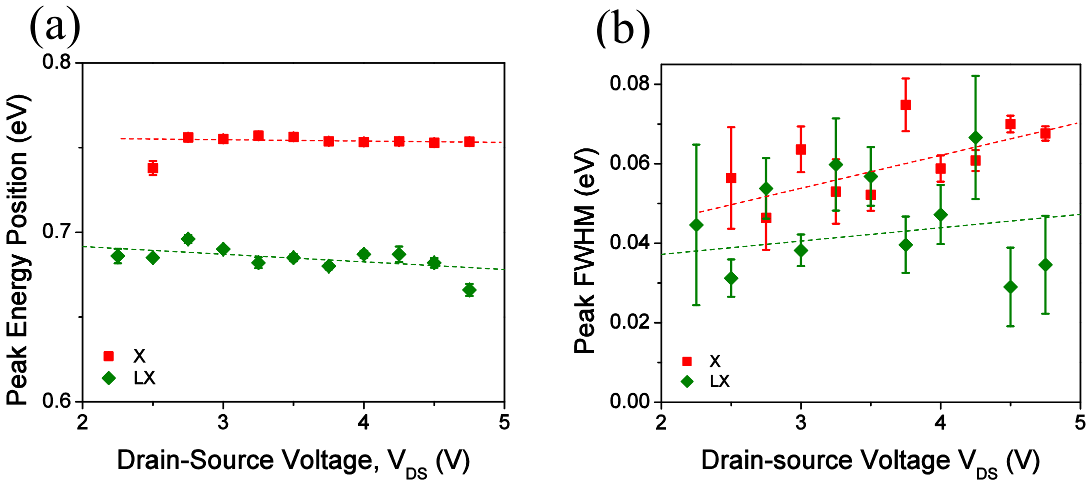

Figure IV-4. Characteristics of a two-peak CNT p-n junction device. The dotted lines are a linear fit for each peak in both figures. (a) Peak positions for X and LX peaks as a function of V_{DS}. The X position changes less than 1 meV per 1 V in V_{DS}. (b) FWHM for X and LX peaks as a function of V_{DS}. The difference between the slopes is not statistically significant.

Figure IV-4 (a) shows the change in peak position for X and LX as V_{DS} is increased. We see that there is little change for X ($\Delta E_X/\Delta V_{DS}$ = - 0.8 ± 0.6 meV/V), whereas LX red-shifts somewhat with respect to V_{DS} ($\Delta E_{LX}/\Delta V_{DS}$ = -4.5 ± 1 meV/V). Red-shifts of PL and EL peaks as a result of drain-induced doping was also observed by Freitag et al. [109]. This is analogous to the red-shifts of E_{33} excitation energy observed under gate field in Ref. [148]. Doping within the channel is thought to change the dielectric screening between electrons and results in bandgap renormalization and a change in exciton binding energy. According to the study by Walsh et al. using different dielectric materials ($\varepsilon = 1$ to 1.78), the increased screening results in the reduction of both of these effects, leading to the combined effect of tens of meVs in red-shift for the E_{22} transition [149]. A similar effect was observed by Steiner et al. for the E_{33} excitation energy reduction of up to 20 meV at $|V_{GS}|$ = 4 V, corresponding to the induced charge density of $|\rho|$ = 0.2 e/nm [148]. The red-shift for E_{11} is expected to be slightly smaller, [150] but the effect should also be an over all reduction in transition energy and by the same order of magnitude. In fact, Freitag et al. also observed a linear red-shift in E_{11} emission corresponding to $|\rho| = 0.25$ e/nm at $|V_{DS}| = 6$ V [109].

As seen in the schematic in Figure IV-1 (c), the recombination region is un-gated and is therefore undoped. We are keeping the back gate at 0 V and we attempt to inject both types of carriers at roughly equal rates in order to maximize the emission, so to the first approximation, the total charge carrier density is kept zero, leading to the absence of a peak shift for the "free-exciton" peak. On the other hand, we observe the total red-shift of 23 meV for the LX peak. Using the scaling relation between ΔE_{11} and $\Delta|\rho|$ derived from the PL data in Ref. 109, we obtain the local charge carrier density increase of $\Delta|\rho| = 0.19$ e/nm, comparable to the global gate effect observed by Steiner et al. and Freitag et al. mentioned above. While we presently do not know the physical details of the localization potential, this information may help eliminate certain types of local fluctuations in future study. In addition, emission peak shift in EL has never been investigated systematically. Our devices show no E_{11} peak shift for the free excitons, which should enable future studies to explore the effect of dielectric environment and of electrostatic doping in EL. In fact, we have some preliminary data (not shown) showing that tuning the global back gate could change the E_{11} emission intensity in EL from CNT p-n junction by up to an order of magnitude.

In Figure IV-5 we compare the ambipolar emission from a diode with the unipolar emission from a back-gated field-effect transistor (FET) made out of the same (long) SWNT. The FET emission amplitude is ~ 4 times smaller than the emission from the diode, although I_{DS} is 12.5 times higher. It is also much broader (~180 meV) and exhibits a slightly asymmetric lineshape, consistent with our unipolar emission characteristics from Chapter III. The FET device was operated in the reverse bias regime, with $V_{GS} < 0 < V_{DS}$ and $|V_{GS}| > |V_{DS}|$. (See Figure IV-5 inset for the schematic band structure of the operating condition.) In this regime, holes are the majority carriers and generate electron-hole pairs by impact excitation. Most electron-hole pairs are generated at the peak field F_{max} near the drain electrode (see inset) and we estimate a lower limit of $F_{max} > V_{DS}/t_{ox} \sim 25$ V/μm, where we use the gate oxide thickness t_{ox} as the screening length [125]. When estimating the contribution of different broadening mechanisms to the emission linewidth we find that, under those biasing conditions, the dominant contribution is due to mixing of exciton and continuum states in the high electric field.

We claimed in Chapter III that in the unipolar case discussed, the lifetime shortening due to the field ionization was the dominant mechanism for the bias-dependent part of broadening. Using the same formalism and the values d = 1.4 nm and F = 25 V/µm, the effect of ionization is estimated to be 38 meV, which comprises only a small fraction of the 180 meV width observed in this case.

The inset of Figure IV-5 shows a simulation [124] of the field dependence of the optical absorption of a 1.4 nm diameter tube. At zero field (0 V/µm; green line), as it is approximately the case in the CNT diodes, there is no absorption in the energy range between the E_{11} exciton and the onset of the weak band-to-band absorption. The absorption and hence the emission are dominated by the E_{11} excitonic transition. In the FET (25 V/µm; red line), however, due to the high electric field, the exciton wavefunction mixes with the band-to-band continuum, which leads to spectral weight transfer from the excitonic peak to the continuum. The band-to-band absorption moves into the forbidden region and merges with the E_{11} exciton peak, resulting in a strongly broadened, asymmetric lineshape. At 25 V/µm, the simulated absorption extends over an energetic range of more than 150 meV. Due to the high electron temperatures in those devices [87], we expect the emission spectrum to be of comparable width as the absorption. Additional broadening mechanisms, such as field ionization already discussed, Auger recombination [79, 129, 146] and phonon broadening [115, 120], will increase the width even further.

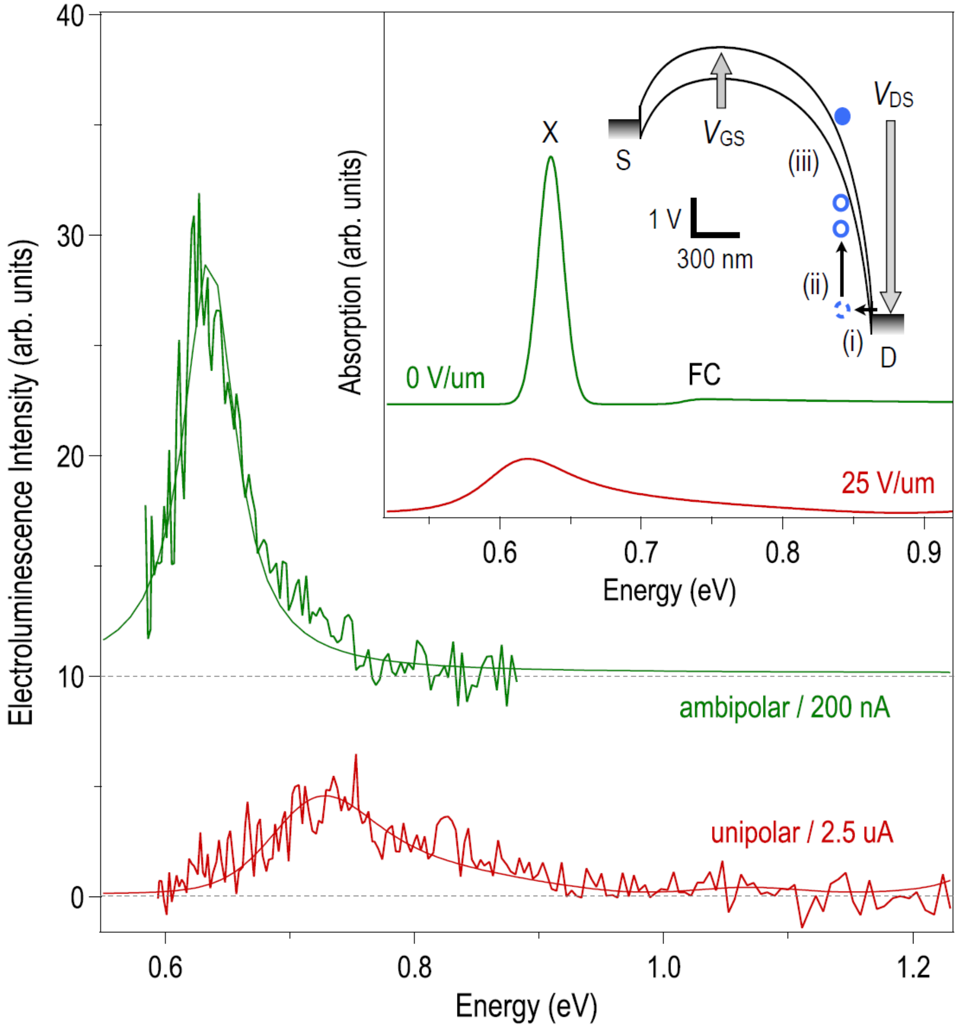

Figure IV-5. Comparison between ambipolar and unipolar light emission. Green line: EL of a CNT diode. Red line: EL emission from a FET device. The upper curve is offset for clarity. Both devices undergo the same processing steps with the only difference being the absence of top-gate electrodes in the FET. Inset: In the FET emission measurements, biases of V_{DS} = +5 V and V_{GS} = -20 V were applied to the drain- and (silicon) back-gate electrodes, respectively. An electric field of >25 V/µm occurs near the drain electrode. Electron-hole pairs are generated by impact excitation. Green line: Calculated absorption spectrum of a 1.4 nm diameter tube (ε_{eff} = 6.0) at zero field. X is the exciton transition, FC denotes the band-to-band (free carrier) transitions. Red line: Calculated absorption spectrum for a field of 25 V/µm. After Ref. 11.

Let us finally comment on the efficiency of the CNT LEDs. Measurements of the PL efficiency of SWNTs yielded values up to [77, 79] ~1 × 10^{-2}, whereas in our devices we obtain at most ~10^{-4} photons per injected electron-hole pair. This difference of about two orders of magnitude can be understood by taking the following two factors into account. First, only a fraction of electrically induced electron-hole pairs possesses the right spin to populate radiative singlet exciton states; $[1+3\cdot\exp(\Delta/kT)]$ times as many populate non-radiative triplet states (k is the Boltzmann constant, $T = 300$ K, and Δ is the singlet-triplet splitting). Using literature values [33, 34] for Δ, we estimate that this effect reduces the efficiency by about an order of magnitude. Second, the short non-radiative lifetime leads to an efficiency reduction by another order of magnitude. Possible routes for improving the efficiency hence would be brightening of the triplet states – for example, by adding magnetic nanoparticles [143] – and/or suspending the CNT to increase the non-radiative lifetime.

4. Conclusions

P-n junction devices were created with single carbon nanotubes using top split gates that electrostatically control spatially-separated p- and n- regions. The transport shows a clear rectifying behavior when the gates are biased in opposite voltages. Compared to conventional ambipolar devices as seen in devices with a global back gate [73, 74], the p-n junction thus created and controlled emits light much more efficiently and at low input power, leading to a narrow linewidth that approaches that of photoluminescence.

The narrow spectra allow us to analyze emission characteristics in greater detail than was previously possible. In some devices, two peaks associated with the E_{11} transition were observed, separated by ~65 meV. We assign the higher-energy peak to free excitons and the lower-energy peak to weakly localized excitons. The latter may be bound to local potential fluctuations, such as defects. As we increase current, we observe a saturation of emission intensity from such localized excitons, suggesting a higher exciton density and a local annihilation mechanism by exciton-exciton interaction. We also observe no shift in the free exciton peak, which indicates a constant local charge density as expected in the recombination region of the p-i-n structure. Conversely, the lower-energy peak red-shifts with increased current, suggesting a local increase in the charge density and an accompanying increase in screening.

We were also able to compare unipolar emission and emission from a p-n junction from the same tube. The unipolar emission shows a characteristic spectrum that was discussed in Chapter III, i.e., an inefficient emission and a large width with a slightly asymmetrical shape. Since ionization by the external field (which explained the broadening at a very high bias employed in Chapter III) only accounts for a small fraction of the total width, we calculated the wave function mixing by Franz-Keldysh oscillation [11, 124]. The effect transfers some of the oscillator strength to the free-carrier interband transition and mixes this state with the excitonic wave function. The calculated result reasonably reproduces the experimental spectrum (Figure IV-5, inset).

While the efficiency was two orders of magnitude greater than what has been observed from conventional CNTFETs, it is still about two orders of magnitude lower than what has been reported in photoluminescence. This is attributed to the fact that unlike photo-excitation, electrical excitation populates dark E_{11} excitons as well as bright excitons, and that the non-radiative lifetime is comparatively short because of mechanisms such as exciton-exciton annihilation and the interaction with the substrate and the top dielectric. Nonetheless, a suspended, bottom-gated CNT p-n junction should be able to show improved the efficiency. Our work also marks an important step toward realization of nano-scale device application in carbon nanotube optoelectronics.

Chapter V The Polarized Carbon Nanotube Thin Film LED

1. Introduction

In the previous chapter, a light-emitting CNT p-i-n junction was demonstrated with a single CNT. Such a device is a basic photonic building block and paves the way for application of CNTs in nano-optics and photonics [111]. The possibility of using a single CNT device as a quantum light source has also been explored [151]. The high quantum efficiency of our devices made it possible to produce narrow emission lines that in turn enabled us to analyze individual emission peaks in detail. While the single-tube LED has such advantages when studying the underlying physics of electrical emission, the likelihood of a device failure is understandably high. Moreover, light output is limited by the maximum current a single CNT can carry. Small-diameter CNTs (d ~1 nm), when aligned at mid-gap with the Fermi level of the metal, have a typical device resistance in the order of 1 to 10 MΩ, which sets the current level at a few hundred nanoamperes at normal operating voltages. The operating drain-source and gate voltages are mostly limited by the breakdown of the gate dielectric and cannot be increased beyond a certain level, typically a few volts in the geometry used. One solution is to increase the number of channels so that the total current-carrying capacity is increased while the load per tube is decreased. This reduces the probability of a tube failure, and even in the event of a single tube breakdown, the device can continue to function.

Consequently, the light emission properties of CNT films and networks [10, 97, 99] have been attracting recent interest beyond single CNT applications. CNT films can be readily assembled from solution and allow for the possibility of scaling up both the current and the amount of light. In addition, CNT films achieve more consistent and stable output among devices by "averaging-out" the heterogeneities of individual CNTs. Furthermore, self-assembled and highly aligned arrays with many CNTs in parallel are expected to preserve the polarization provided by the one-dimensional character of individual CNTs. Since emission and absorption of light that is polarized parallel to the long axis of a CNT occurs with higher efficiency, an aligned CNT film could be a promising building block for future laser applications.

In this chapter, we report on the realization of a light emitting p-i-n diode from a highly aligned film of semiconducting carbon nanotubes that emits light in the near-infrared spectral range. A split gate design similar to the single-tube CNT diode allows for tuning both the rectifying electrical behavior of the diode and its light generation efficiency. The CNT film diode produces light that is polarized along the device channel, a direct consequence of the high degree of CNT alignment in the film that reflects the polarization property of the 1D nature of individual tubes.

2. Physical characteristics of CNT films and top-gated devices

We deposited CNT thin films on a Si(p++)/SiO_2(100nm) substrate from a suspension of 99% semiconducing (arc discharge) carbon nanotubes with diameters ranging from 1.3 to 1.7 nm, separated by density-gradient ultracentrifugation [98]. With this desposition technique, CNTs align in parallel at the contact line between the solution and a vertically immersed planar substrate. The slip-stick motion of the contact line during evaporation produces periodic arrays of regular CNT thin film stripes that cover a large area of the substrate, each stripe having a width of about 10 μm and a height of 1 to 8 nm, depending on the degree of CNT bundling (see Figure V-1 (c)). The CNT stripe formation relies solely on self organization without the need for etching or lithography to obtain the patterns. These CNT films have been extensively characterized by optical and electrical techniques as well as by SEM and AFM (see Ref. 99 and Figure V-1). Further details on the assembly technique and its mechanism are available in Ref. 99.

We first contacted sections of a stripe by source and drain electrodes (Ti = 1 nm/Pd = 40 nm/Au = 20 nm, Figure V-1 (a)), and then deposited 30 to 50 nm of Al_2O_3 by means of atomic layer deposition. Ti top gates (thickness: 15 to 35 nm) were then defined by e-beam lithography and deposited by e-beam evaporation (Figure V-1 (b) and V-2 (a)).

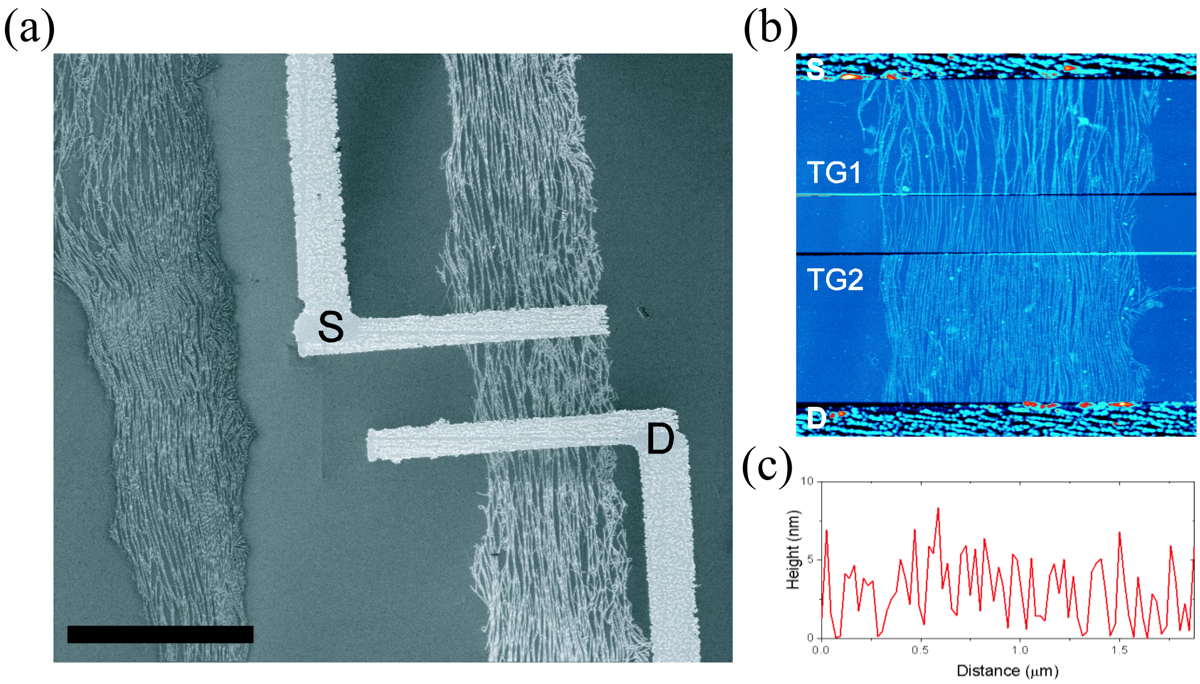

Figure V-1. (a) SEM image of self-assembled CNT stripes, one of which is contacted with metal contacts. The two L-shaped objects marked “S” (source) and “D” (drain) are the electrodes. The middle stripe appears brighter because of local charging from the metal under the SEM beam. The length of the black scale bar corresponds to 10 μm. (b) AFM image of a fabricated top-gated device. “TG1” and “TG2” denotes the top gates. (c) Height profile of an ungated section between “TG1” and “TG2” from (b).

As sketched in Figure V-2 (a), the operating principle of diode is the same as in single-tube diodes (Chapter IV); the top gates control the electrostatic doping of the CNT film segments underneath to create a p-n junction. Applying different voltages to the gates creates p- and n-doped segments and a recombination region in-between with a potential drop (~1 μm, see Fig. 1(b)). The channel length L_C between the source and drain contacts varied from 4 μm to 10 μm and exceeds the average CNT length of around 1 μm in order to avoid shorting the channel with residual metallic nanotubes. The channel length was found to be critical for having a good on/off ratio when the back gate is swept, even though the amount of metallic tubes was only 1 % (details in Ref. 99), since metallic tubes contact metal much better. In order to avoid creating short circuits in the device with metallic tubes, L_C needs to be significantly greater than the average CNT length, which means that electronic transport along the channel relies on percolation instead of direct conduction between the drain and the source. Figure V-2 (b) shows an SEM image of a CNT film diode with L_C = 10 μm. In the following, we investigate the electrical transport behavior of the devices thus fabricated.

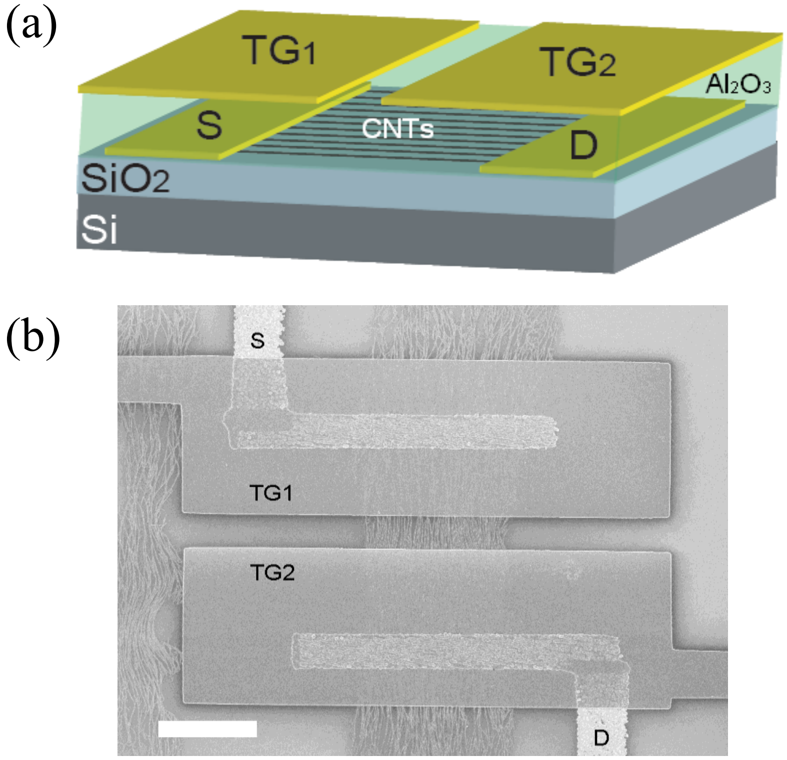

Figure V-2. (a) Schematic illustration and (b) scanning electron microscope image of CNT film diodes with split top gates (TG1 and TG2). The white scale bar on lower left is 5 µm long.

3. Transport characteristics of the CNT film diode

As we saw in the case of the single-tube CNT diode, good transport behavior is critical for efficient light emission. This is not surprising since the radiative recombination rate of excitons in CNTs is much smaller than the non-radiative recombination rate. Here, we discuss electronic transport of CNT film devices with top-split gate to confirm that they do indeed behave as diodes.

The electrical transfer characteristics of two devices with different channel lengths (4 µm and 6 µm) are shown in Figure V-3 (a) and (b). We see that the fundamental requirement for CNT diode construction, namely the ambipolar behavior upon gate-sweeping, is satisfied in these devices. The almost symmetric, ambipolar transfer characteristics of the devices indicate that both electrons and holes can be injected into the channel with similar efficiencies. We also see that there is much less noise in current compared to single-tube devices under similar conditions (compare to Figure III-3, for example), because multiple channels cancel fluctuations from individual tubes. The sheet resistances was found to be around 1 MΩ/□ and the on/off current ratios is about 100 for V_{DS} = 1 V. The performance is somewhat degraded both in conductivity and in the on/off ratio compared to the global bottom-gated devices in Ref. 99. This is partly due to the fact that the global gate covers the entire device channel while our split gates have only partial channel coverage. More significantly, we re-used the same material, and re-processing the same film multiple times degrades the performance by introducing defects and impurities. It has also been observed in single-tube devices that applying high bias seems to damage CNTs. The D-line (i.e. defect induced; see Introduction) intensity from Raman measurement in a single tube increases after we applied high bias/current repeatedly. In addition, as described in Chapter IV, we have observed that the defect-bound E_{11} peak developed after measurements in a single CNT p-n junction.

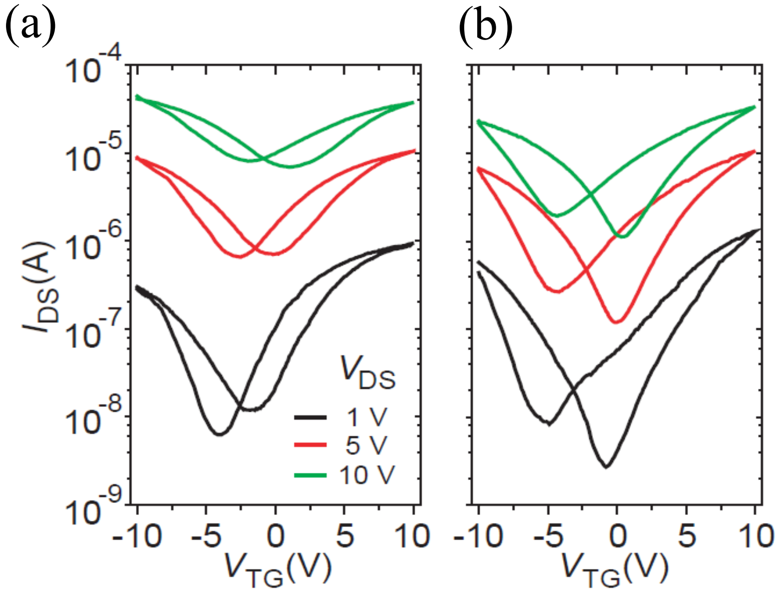

Figure V-3. (a, b) Source-drain electrical current transfer as a function of the top-gate voltage measured for CNT film diodes with a channel length (a) L_C=4 μm and (b) L_C=6 μm, respectively, where $V_{TG} = V_{TG1} = V_{TG2}$. V_{TG} was swept in both directions, resulting in hysteresis that is typical in on-substrate CNT devices. The bottom gate was floating. After Ref. 152.

The decreased on/off ratio at a higher V_{DS} is thought to be analogous to the higher off-current for single-tube devices (see Figure III-1 and III-3, for example), which is due to the bias-assisted tunneling though Schottky barrier at the injection site at "off-state" V_{TG}. As for the effect of the channel length, we observe that as L_C increases from 4 to 6 μm, the split gate effect becomes more pronounced and the attainable on-current decreases. This is similar in principle to the observation of an increasing on/off current ratio and a decreasing on-current with increasing L_C in devices made out of the same film but equipped with a single global top gate [99]. The on-current decrease is simply a function of overall channel resistance, which comes from diffusive transport under percolation and a channel length greater than the electron scattering length. The inferior on-off ratio of the shorter channel arises from the incomplete turn-off due to a small residual amount of metallic tubes in the film. The effect and the probability of a (at least partially) short-circuit created by metallic tubes decrease as the entire channel length is increased, leading to a better off-state in Figure V-3 (b) than in (a).

Now we examine transport by applying a differential voltage between V_{TG1} and V_{TG2} to see if they operate as p-n junction diodes. In Figure V-4 (a) and (b), we show the electrical output characteristics of the same two devices (with different channel lengths) already shown in Figure V-3 above. We swept V_{DS} between -10 V and +10 V while keeping the split gate voltages at specific values. First, we focus on the transport when it is forward-biased, i.e. positive V_{DS} in this case in the right half of each figure. By stepping up voltages of opposite polarity to the two split gates from 0V/0V (black) to -10V/+10V (magenta), we observe that the forward-biased transport becomes more efficient for a given V_{DS}. It is also interesting that the increase in current is more prominent for the longer-channel device as the split gate voltage difference is increased. For example, compare the differences in I_{DS} at maximum V_{DS} between the minimum split gate (0V/0V, black) and the maximum (-10V/10V, magenta) between the panels. The 4 μm device shows only a factor of two increase in current from 16 μA to 32 μA (Figure V-4 (a)), but the 6 μm devices sees an increase greater than an order of magnitude from 1.9 μA to 20 μA (Figure V-4 (b)). As we saw in the ambipolar top-gate sweeps of the same devices, the longer diode has a better on/off ratio, which means that we can control the accumulation of p- and n-doped carriers more effectively. Hence, it is reasonable that the longer-channel device has a better diode behavior.

In the reverse direction (i.e., negative V_{DS} in this case; the left half of each panel in Figure V-4), split gate voltage has the opposite effect, namely suppression of electronic transport resulting from the increase between the top gates. This is precisely what is expected from a diode that is reverse-biased (unless it is in the avalanche regime). At 0V/0V, it works more like a regular resistor, although the effect of Schottky barriers is evident at small V_{DS} from the nonlinearity of I_{DS}-V_{DS} near zero. As the voltage between the split gates is increased in magnitude, the device becomes more resistive. Again this effect is more pronounced in the longer-channel diode with a better on-off ratio. In summary, by increasing the potential drop between the split gates, we obtain a gradual improvement of the rectifying behavior in the CNT film diode.

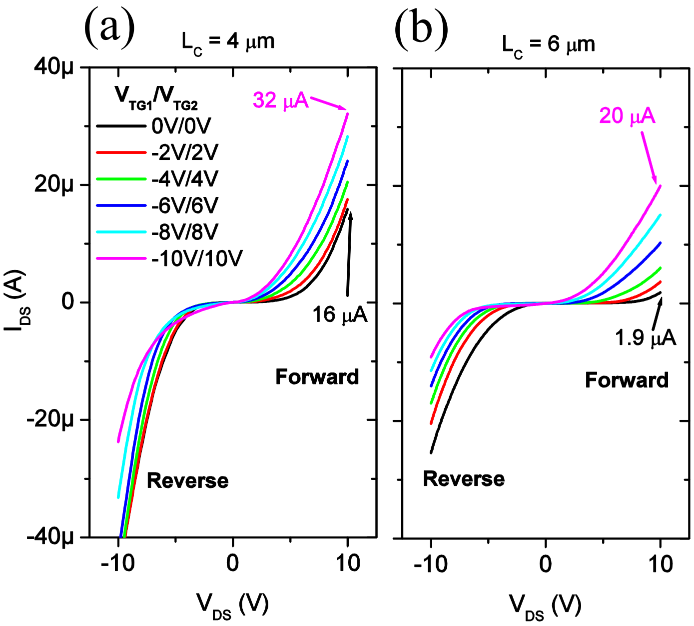

Figure V-4 (a, b) Electrical output characteristics measured for the same devices as in Figure V-3 (a, b), respectively. In the forward bias direction (marked "Forward": positive V_{DS}), the electrical output increases as a function of the difference between the two split gate voltages from 0V/0V (black) to -10V/10V (magenta).(potential drop), while the output is generally suppressed in the reverse direction (marked "Reverse") as a function of greater split-gate voltage. After Ref. 152.

We should emphasize here that we use the terms "forward bias" and "reverse bias" as they are used in conventional p-n diodes. Indeed, we applied drain-source and split-gate voltages following that convention and observed that "forward" and "reverse" biases create p-n junction and a diode behavior that we expect from just such biasing schemes. However, potential fluctuations in conduction and valence bands in these devices are far more complex than in a standard p-n diode, and we do not expect the almost ideal behavior that is observed in p-i-n diodes made of single CNTs [11, 80, 81]. In the present case, multiple CNTs with different diameters and chiralities are contacted, with many of them bundled, and charge carriers have to overcome various tube-to-tube contacts in order to cross the channel. Also, the height of Schottky barriers between the metallic source/drain contacts and the CNTs are highly variable between the tubes as external electric fields are applied because of different diameters and varying quality of individual contacts [99]. Nevertheless, if the voltage range is restricted to moderate values of V_{DS} between -5 V and +5 V, for example, the CNT film diodes can be operated more closely as rectifiers, as shown in Figure V-5 for CNT film diode with two different channel lengths, 6 µm and 10 µm. In the reverse direction, the current flow is very limited, although not completely suppressed. Again, we see that the attainable on-current is smaller, but the rectifying behavior is slightly better (i.e., the suppression is more complete) for the longer-length device.

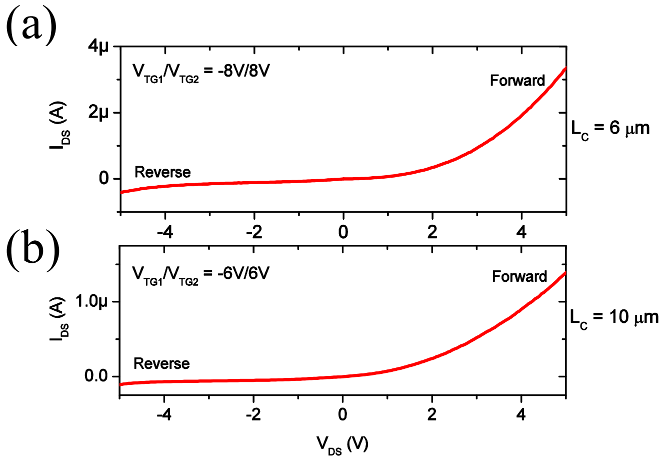

Figure V-5. Examples of two diodes with rectifying characteristics for CNT film devices with (a) L_C = 6 µm and (b) L_C = 10 µm. The vertical axis scales are different between the two.

4. Electroluminescence characteristics of the CNT film diode

Next, we discuss the EL properties of the CNT thin film devices. In general, the radiative decay of excitons is responsible for light emission in CNTs. Excitons can be electrically generated in CNTs via (i) simultaneous injection of electrons and holes that form excitons and radiatively recombine (giving rise to threshold-less ambipolar electroluminescence), or (ii) accelerating electrons or holes to energies sufficient to create excitons, i.e., the so-called impact excitation (giving rise to unipolar electroluminescence with threshold characteristics) [111]. By using a p-i-n design, we aim to improve the control of simultaneous injection of electrons and holes in order to increase the efficiency of the threshold-less ambipolar electroluminescence, making the CNT film a more efficient light emitter.

Figure V-6 (a) and (b) show images from optical reflection and an EL signal detected by the infrared camera, and an overlay of the two images (c,d) to demonstrate that the signal is coming from between the top gates. Given enough input power (power $P_{EL} = I_{DS} \cdot V_{DS}$), we find that the devices emit infrared light in both non-diode mode (unipolar) and diode mode (ambipolar). Since the top gates are covering the areas near contacts (Figure V-2 (b)), we can only detect signals from between the top gates, as shown in Figure V-6 (d). Compared to single-tube FETs, we find that even unipolar devices luminesce in the middle part of the channel as opposed to near contacts. While Figure V-6 (d) may hint at a more localized emission character for the ambipolar emission (red line and symbols), the limited spatial resolution does not allow us to draw any conclusions on the differences between unipolar and ambipolar emission from the spatial data. Given the distance between the top gates (~1 μm) and the EL peak wavelength (~2 μm), we are at the theoretical resolution limit.

Does a film LED produce more light than a single-tube LED? Figure V-7 compares the total light output from the two different types of devices under the same source-drain bias. Clearly, the overall light output of the film LED is far superior to that of the single-tube LED, showing that we can indeed "scale up" carbon-nanotube devices in terms of light emission. At V_{DS} = 10V, the single tube and the film are carrying 350 nA and 18 μA, with the light output yield of 4900 and 76000 in arbitrary units, respectively. On the other hand, this translates to 14,000 a.u. of emission per μA for the single-tube device versus 4,200 a.u. per μA for the film. It is not surprising that the single tube diode is a more efficient emitter; after all, the CVD-grown tube has been subjected to much less chemical processing, and it does not rely on percolation for conduction. But we can never achieve significant total light output with the single device because we cannot pass more than about 1 μA of current without destroying the tube itself. Ideally, parallel single-tube devices with good quality, long small-diameter CNTs that are almost exclusively semiconducting would be ideal for the maximum light output, but there is much technical challenge before such a device can be constructed. Our parallel-tube, percolation-driven devices are the best CNT electrical emitter to date in terms of total light intensity.

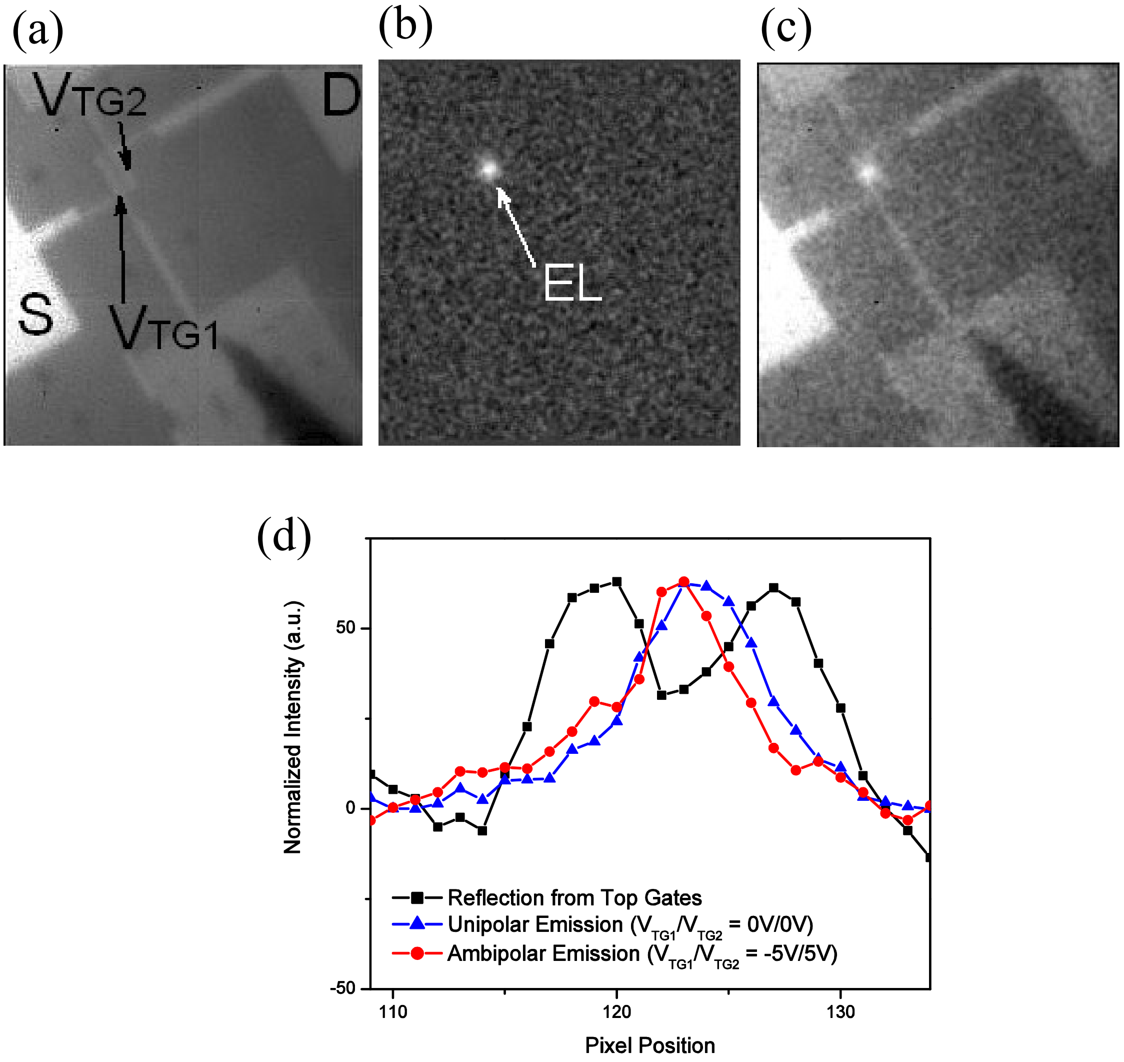

Figure V-6. Spatial characteristics of EL from a 4-μm CNT light emitting diode taken at the same sample position. Note that the device dimensions are close to the resolution limit (~1 μm) of the optical measurement due to both the wavelength of the detected light and the pixel size. (a) Reflected image of a device showing the source and drain pads (marked “S” and “D” respectively) and the top gates (marked “V_{TG1}” and “V_{TG2}”). (b) EL signal from the same device as in (a). (c) Combined image of (a) and (b), showing that the EL signal is located between the two top gates. (d) Spatial cross sections of a reflection as in (a) against a unipolar and ambipolar emission signals across the device channel. The two top gates (lateral spacing = 1 μm) can be recognized as double-peak feature. Detectable EL emission originates from the device area between the two split gates (unipolar: split gate voltages off; ambipolar: split gate voltages on).

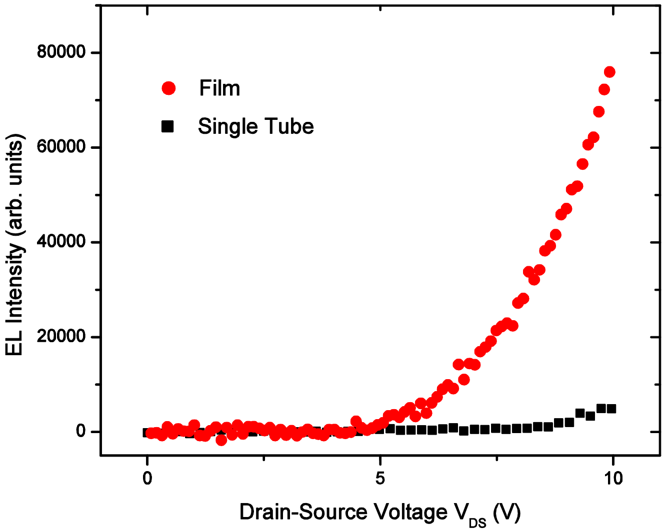

Figure V-7. Light output characteristics (spectrally integrated EL intensity) of both a CNT thinfilm LED (red circles) and a single-tube diode (black squares). Both devices are biased in the forward mode. The corresponding split gate voltages V_{TG1}/V_{TG2} are -5V/+5V for the film device and -20V/+20V for the single-tube device. After Ref. 152.

Figure V-8 (a) shows the EL intensity of a device integrated over wavelength as a function of source-drain voltage. As a reference, we plot in the inset of Figure V-8 (a) the electrical transport characteristics of the same device. We see from the I_{DS}–V_{DS} curves that this device has the same type of top-gate dependence as the devices in Figure V-4. In the forward-bias direction (i.e., positive V_{DS} in Figure V-8 (a)), we observe a substantial increase of light intensity up to a factor of 16 for a fixed V_{DS} as we increase V_{TG1}/V_{TG2} from 0V/0V to +5V/-5V. In the reverse-bias direction, despite the high currents achieved (see the negative V_{DS} side in inset Figure V-8 (a)), we only observe relatively weak electroluminescence if we increase $|V_{DS}|$.

We also note that the onset of the forward-biased emission coincides with the current onset, while the onset of the reverse-biased emission lags behind the current onset. This is discussed in more detail for V-8 (b) inset below, and additionally in the investigation of electroluminescence width.

It should be noted that we do not observe a significant influence of the split gate in the intensity characteristics of the emitted light in the reverse direction; on the negative V_{DS} side, the intensity is almost identical for all the split-gate settings at any given V_{DS} value. Although there is a potential drop between the top gates, the field created by the V_{TGS} biasing does not appear to be greater than the impact excitation threshold, since there is little dependence on that parameter. In contrast, a single-tube device operated as a unipolar emitter shows a clear dependence on bottom global gate voltage (not shown), which is reasonable because the light generation depends of the degree of band bending at contacts that controls the carrier injection rate (see Figure IV-5 inset for schematics). From such split-gate effects and the differences between the forward and reverse biases, we can conclude that the CNT film device functions as a light-emitting diode.

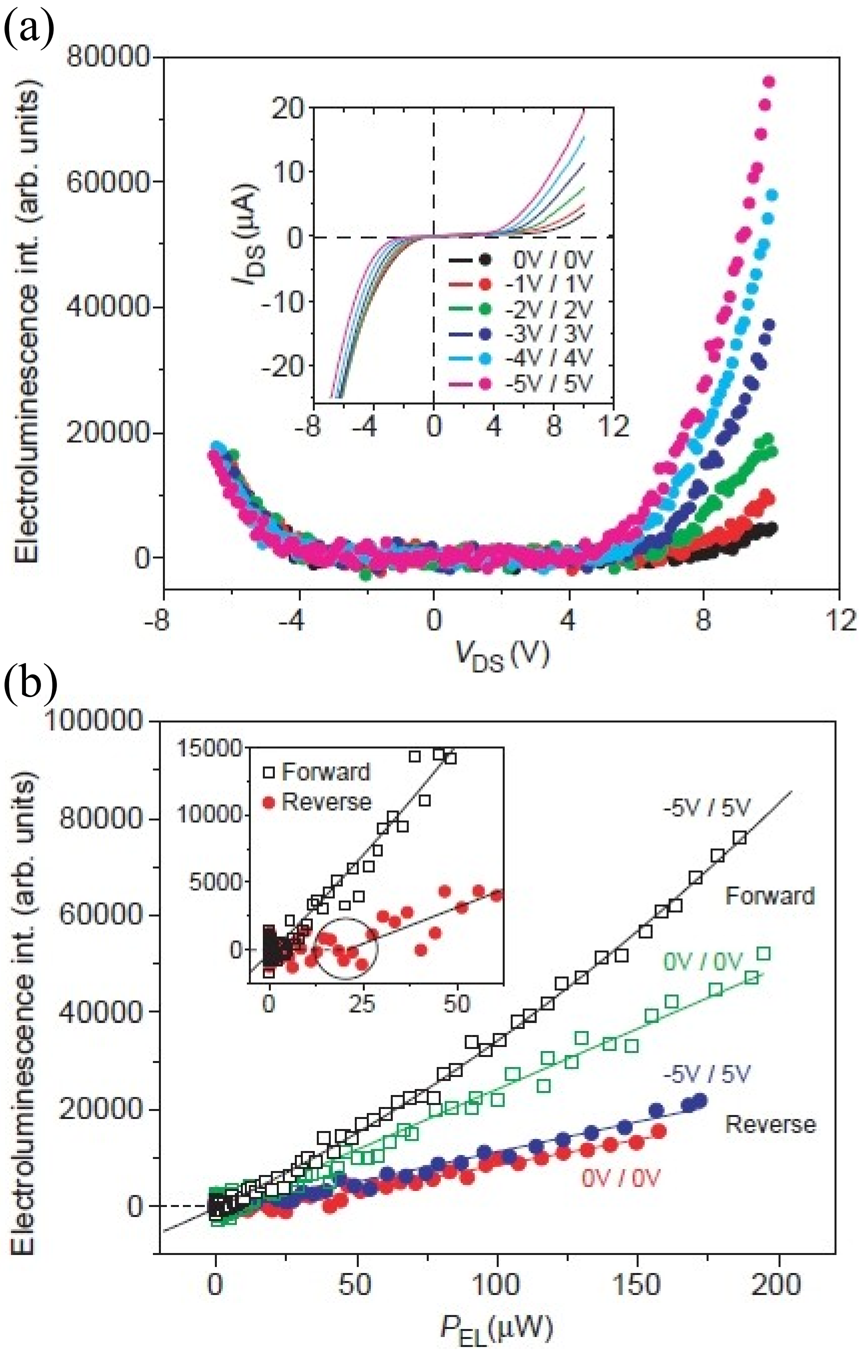

Figure V-8. (a) EL intensity and corresponding drain-source current characteristics (inset) as a function of source-drain voltage. The associated top gates voltages V_{TG1}/V_{TG2} are denoted in the inset. Positive V_{DS} indicates the forward-bias direction. (b) Electroluminescence intensity plotted as a function of electrical power $P_{EL}=V_{DS}\cdot I_{DS}$. Experimental data points are represented by symbols (open symbols: forward bias, solid symbols: reverse bias), the lines represent best fits to the experimental data points. The corresponding top gate voltages V_{TG1}/V_{TG2} are also indicated. (Inset) The zoom reveals the threshold behavior. After Ref. 152.

In order to investigate whether the light generation efficiency is improved by the use of a p-n junction, we plot in Figure V-8 (b) the integrated EL intensity as a function of the injected electrical power, $P_{EL} = I_{DS} \cdot V_{DS}$ for several voltage configurations. With the device biased in the reverse direction, we obtain linear power dependency with almost identical slopes, independent of the split gate voltages applied (Figure V-8 (b), solid blue and red circles). Again, we see little effect of the split gates in the reverse mode. If the device is biased in the forward direction (Figure V-8 (b), open squares), we observe that the slope of the intensity curve is steeper than the curves in the reverse mode. This indicates a greater efficiency with which the device generates light when biased in the forward direction.

More importantly and perhaps more interestingly, if the split gate voltages are tuned from 0V/0V to +5V/-5V and the device is swept in the forward direction, we observe a strong increase of light generation efficiency (Figure V-8 (b)). The power dependence can be captured adequately by fitting a quadratic form to the data points. The somewhat greater-than-linear power dependence observed might be due to either higher order electrostatic field contributions (across the junction) or higher order excitonic effects (in the CNTs); the investigation of both effects is beyond the scope of this study. At P_{EL} = 150 μW, the light generation efficiency has increased by a factor of 4 as compared to the reverse mode.

We found that the “forward” bias is more efficient than in “reverse” bias, even without split gate voltages applied. Here, “forward” and “reverse” simply refer to the polarity of V_{DS} as in Figure V-8 (a); since the top gates are not biased, there are no p- and n- segments created, at least in theory (there may be some residual doping of the substrate, as is typically evidenced in the hysteresis discussed in Chapter III). By switching the source and the drain, we find that the efficiency changes significantly; compare the 0V/0V curves in Figure V-8 (b), for example. This effect is associated with built-in non-uniformities of the CNT film and the potential profile of individual devices. We found that a certain level of asymmetry almost always exists in the electrical transport behavior (see for example the transport at 0V/0V, solid red circles vs. open green squares, in Figure V-4 (b)), making devices operate more efficiently for a certain choice of (source/drain) bias conditions. This is not surprising since the respective carrier injection rate from each contact depends on the details of the tube-metal interfaces. Although the diode behavior was also observable in the non-ideal source/drain choice, we consistently chose the better source/drain assignment for diode in order to observe the split-gate effect more clearly.

We attribute the observation of the improved light generation efficiency in the forward mode to an enhancement of ambipolar recombination in the intrinsic CNT film segment. The threshold characteristics of the device are consistent with our interpretation. While the CNT film diode generates light virtually threshold-less in the forward mode (see inset Figure V - 7(b)), it displays the threshold behavior when biased in the reverse mode. This could be interpreted as an impact excitation signature; however, in the present case, high fields are expected to be next to the contacts where the top gate is blocking the light, while the light generation is in the middle of the channel. Exciton diffusion length in CNTs has been estimated to be about 100 to 200 nm by various groups, with the largest estimate being 1 μm using mostly time-resolved photoluminescence techniques [77, 130, 153-156]. It is not yet clear what parameter(s) affect the differences among the groups. Nonetheless, the emission region on our sample is at minimum a factor of few longer than the diffusion length, so excitons created at contacts would not contribute to the emission observed from these devices. By comparing to single CNT diodes attaining conversion efficiencies in the order of 10^{-4} photons per electron-hole pair (exciton) [11], we estimate that the conversion efficiency of the CNT film diode is lowered by at least one order of magnitude. This result can be understood by considering that: (i) the CNT film diode is a percolation device relying on non-ideal nanotube-nanotube contacts; (ii) the CNT material has a much higher defect density because it has been solution-processed and (iii) the presence of remaining metallic nanotubes in the film effectively quench light emission due to non-radiative energy transfer. Techniques such as aligned CVD [157] with preferential growth for semiconducting tubes [158] may provide solutions to these problems in the future. However, the long radiative lifetime and the existence of a lower-energy dark exciton are basic properties of excitons in carbon nanotubes [33, 34], and overcoming the competing decay processes poses a significant challenge in improving the efficiency of CNT-based LEDs beyond a certain limit.

5. Investigation of Electroluminescence Spectra

We also measured EL intensity as a function of emitted photon energy to further explore the characteristics of emission. Figure V-9 shows EL spectra for forward (a) and reverse (b) biases from the same device. Recall that forward bias shows a more efficient ambipolar recombination behavior from the p-n junction than in the reverse bias. We kept the top gate biases constant at -5V and +5 V, and stepped up the V_{DS} in the positive (a) and negative (b) directions to induce the two different modes similar to Figure V-8. We fit Gaussian distributions to the spectra to extract the peak positions and the widths under the assumption that the emission comes from a collection of multiple tubes with a distribution of diameters. As we shall see in the following, the emission is not a simple reflection of the diameter distribution; however there is still a multiple-tube effect and the Gaussian function fits the emission profile quite adequately (Figure V-10 (b), inset).

The device emits electroluminescence in the near infrared with a maximum spectral intensity at about 0.58 eV in the forward direction and 0.60 eV in reverse. There was no measurable peak shift observed as the input power was increased. Given the diameter range of 1.3 nm to 1.7 nm and referring to the Kataura plot [15], the intensity peaks are at the lowest edge of the E_{11} energy range for the sample, in agreement with Ref. 97. As Engel et al. suggests [99], this is expected since larger diameter tubes have smaller Schottky barriers which is critical for carrier injection, and excitons efficiently relax into lower-energy states in large-diameter tubes [159, 160]. Adam, et al. found a similar effect in their carbon-nanotube network FETs operated with a global gate [97]. An efficient energy transfer mechanism, Förster Resonance Energy Transfer, has been suggested as the major contributor because of the aligned orientation of dipoles between exciton donors and acceptors [160]. Qian et al. obtained the maximum transfer rate of 0.5 ps^{-1} in their DNA-wrapped CNT sample [159], which is even faster than the nonradiative decay rate in our single-tube LEDs (a few ps). As we saw in the AFM profile of our sample (Figure V-1 (c)), the tubes are largely in bundles; furthermore, most of our tubes are in good alignment with each other (Figures V-1 and V-2), making the Förster interaction a very likely mechanism responsible for the observation of energy peaks at the lowest-energy edge of our diameter range.

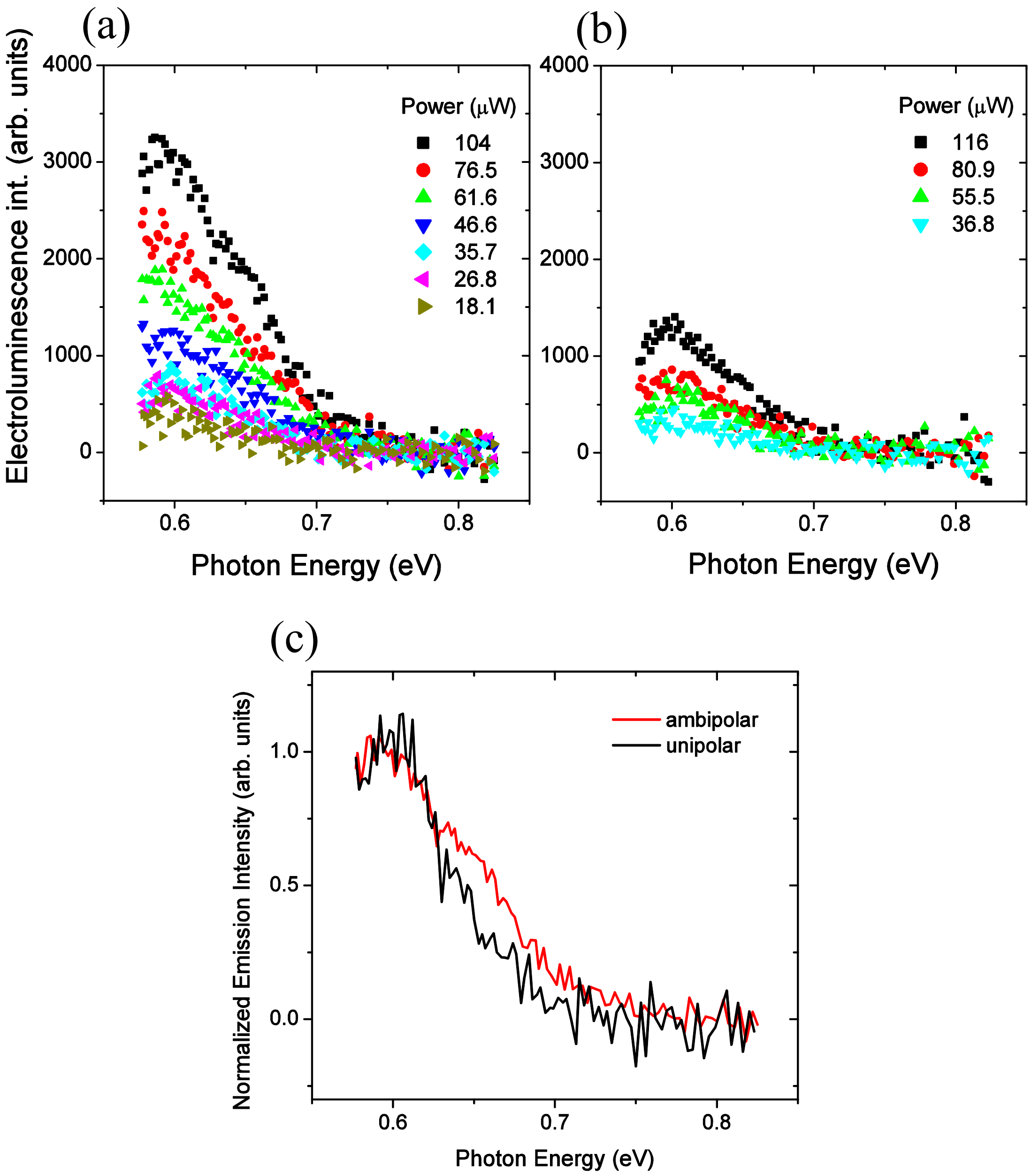

Figure V-9. Electroluminescence spectra of a CNT film light emitting diode with channel length $L_C = 4\mu m$ biased in (a) forward (ambipolar) and (b) reverse (unipolar) mode. The device used was the same as in Figure V-8. The top gate values used were $V_{TG1} = -5$ V and $V_{TG2} = +5$ V. The same symbols and colors are used for relatively comparable P_{EL} between (a) and (b). (c) Comparison of forward (ambipolar) and reverse (unipolar) mode, respectively. The electrical parameters during data acquisition are $V_{TG1} = -5$ V, $V_{TG2} = +5$ V, $V_{DS} = 10$ V, $P_{EL} = 104$ μW (forward mode) and $V_{TG1} = 0$ V, $V_{TG2} = 0$ V, $V_{DS} = -6$ V, $P_{EL} = 152$ μW (reverse mode).

In the previous study which examined global bottom-gated transistor behavior from the identical raw material [99], EL and PL intensity maximum of another device was found at 0.64 eV. Referring to the empirical Kataura plot by Weisman et al. [15], we see that different chiralities for the same diameter could easily differ in emission energy by about 100 meV in this diameter range. If only a limited number of tubes are involved in emission, as discussed above, statistical averaging between samples is limited; the difference of 40 meV in peak positions between devices is entirely possible. Since we do not have enough spatial resolution to identify the tubes participating in emission (let alone determine diameters and chiralities of those tubes), it is not possible to make any meaningful conclusions based on the comparison between the two unipolar emission peaks, other than suggesting that that number of tubes involved in conduction and emission may be small.

On the other hand, the ambipolar and unipolar emissions in our data are from the same device and from the same measurement session, which makes them more directly comparable. Figure V-9 (c) compares normalized intensities of the two modes. In addition to the small difference in the maximum intensity energies, we see that in forward bias, there is a greater spectral weight of higher-energy emission. This was not observed in reverse bias, even when the intensity was comparable (when the intensity is increased, the broadening obscures the difference somewhat, but there is no feature around 0.65 eV). This would not be the signal from exciton-optical phonon coupling, since the optical phonon energy is about 180 meV, much larger than the signal-main peak separation observed. The difference in energy suggests the separation between the defect-bound and the “free exciton” states in single-tube CNT diodes. While it may seem unlikely that one observes spectral features in electroluminescence signal from such an ensemble of CNTs with a range of diameter and various chiralities which undoubtedly lead to a wide range of E_{11} transition energies [15]. However, existing literature on tube-tube energy transfer suggests that the long channel length ensures that lower energy states dominate, since energy relaxation to tubes with lower-energy E_{11} states happens very fast, within 3 ps. In that case, it is reasonable that the defect-bound states and free-exciton states can show up as two peaks at least to some extent.

We have seen during single-tube LED measurements that the lower-energy, defect-bound state sometimes appears after the tube has been stressed with higher levels of current. The films devices have already gone through higher-current measurements and “recycling” from previous measurements (i.e. additional chemical processing), so the dominant peak (around 0.60 eV) is assumed to be from the defect-bound states. For current film LED spectra, we took the spectral data in forward bias first, followed by the reverse bias involving higher currents, which would explain that the free-energy states are still observable in the spectra for the former during which up to 10.4 μA was passed through the device. By the time the second spectral measurements were conducted, there was hardly any emission from free-exciton states, although there was still a hint of it around 0.65 eV at a higher intensity (Figure V-9 (b)).

Figure V-10 shows the widths (FWHMs) of the same spectral data as a function of applied power and of emission intensity. The devices were operated in three different modes; as a split-gate diode LED, as a resistor (i.e., no applied gate voltage), and as a global back-gated FET. We found that the Gaussian functional form fits our data well (Figure V-10, inset), from which to extract the widths. There are several features in the plots that distinguish the emission behaviors of film devices that we can compare to spectral characteristics of single-tube devices.

First, the overall widths are much larger than in single-tube LEDs in which we achieved the smallest width observed in carbon-nanotube electroluminescence. Film LEDs are constructed of tubes with a range of diameters and are operated at much higher overall power, so the larger width is not particularly surprising. The single-tube LED is constructed from a clean CVD-grown nanotube and is operated at the level 0.01 W/m. The film device is fabricated with many chemically-processed nanotubes deposited onto a substrate and requires at least 100 times larger power input to observe luminescence with the same sensitivity. This means that we do not have sufficient data at the lower end of the power range to extrapolate the behavior of luminescence intensity in film devices to that of single-tube devices. Since one of the objectives of constructing the film LED is to scale up the light output of nanotube-based devices rather than to elucidate fundamental principles of the emission process, the comparison between the single-tube and film LEDs is not particularly useful.

Consequently, we discuss here some of the mechanisms that are relevant to the spectral width in film devices, with an emphasis on the effect of the electric field, which was found to be the dominant source of bias-dependent broadening in single-tube FET emission. Figure V-10 (a) shows a width of ~135 meV for the FWHM in the film device operating as a single-gate FET at the input power of 250 W/m. Let us recall that the FWHM was about 300 meV at the same input power for a single-tube unipolar FET emitter (Figure III-8). In the film device, there is a brief rise in width to ~ 50 W/m, followed by a more or less constant width, even up to a power input of 500 W/m. This trend does not depend on the operating mode; top gate biasing has little effect on the way the width increases as a function of power.

Given the fabrication and operation of the film device, we can safely assume that some of the mechanisms discussed in Chapter III are also at work here. In Chapter III, we estimated that about 70 meV was due to tube heterogeneity and phonon scattering at a power as low as 40 W/m, of which at least 20 meV is due to temperature-dependent acoustic phonons. We do not have enough data points to extrapolate the width reliably to zero power, but the minimum width is at least 100 meV (see Figure V-10). We assume that the degree of tube heterogeneity should be comparable to that of single tubes (i.e., the same raw material and similar fabrication processes). The effect of high-energy optical phonon scattering, which result in multiple-peak effect that contribute to overall width, should be less film devices, since current per tube is much lower.

Since exciton-exciton annihilation does not seem to play a significant role in single tube devices, it is unlikely that it plays a role here where we have even smaller exciton density per channel. While we do not have information on the current load per channel, it is undoubtedly much smaller than on a single-tube device carrying the same magnitude of current. Therefore, other effects such as temperature-based broadening and exciton-exciton annihilation effects, both of which do not make a significant contribution to the width in a single-tube device, should also be quite limited.

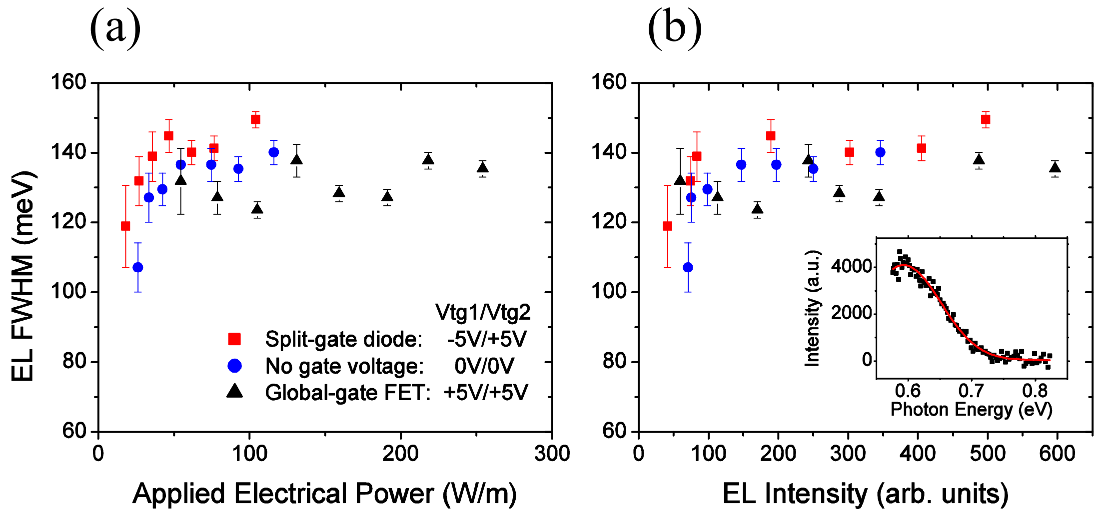

Figure V-10. Full-width at half maximum of electroluminescence spectra as a function of (a) applied power and (b) light emission intensity. The device was operated in the diode (red squares), resistor (blue circles) and single-gate FET (black triangles) modes by changing top-gate voltages. The inset in (b) shows the example of a typical Gaussian fitting with data taken with the device operating in the global gate FET mode (V_{TG1}/V_{TG2} = +5V/+5V) at the drain-source bias of 12 V. The data correspond to Figure V-9 (c). The widths were extracted by fitting the Gaussian function on each spectrum. Since the spectral peak is near the edge of the detection range and widths depend sensitively on the peak position, the average peak position was determined first and used as a fixed peak position (no statistically significant peak shift was observed) before the fittings were performed.

We attribute the small and rapid rise in width we see at a low power (up to ~50 W/m) to the multiple-tube effect. While Adam et al. found that only 4 % of the largest diameters contribute to emission in carbon-nanotube network FETs, our parallel-tube film FETs, with distinctly separate channels, are statistically more likely to involve a somewhat wider range of diameters that participate in conduction. We can think of a parallel-tube film as a collection of many networks, each with a limited number of tubes. Depending on the degree of bundling, the conducting path in any given channel can involve smaller-diameter tubes in the emitting region than the largest diameter tubes in the sample. To find the distribution of conductive paths would require a statistical analysis of devices made with different widths from the same film (since the film thickness varies), which is beyond the scope of this study. However, the very rapid rise in the width seen at low electrical power can be attributed to this effect. At the lowest bias/power, only the paths with largest diameter tubes can contribute to conduction. As the source-drain bias is increased, contacts to smaller diameter tubes become transparent so they can carry current and emit light as well, which adds to the spectral width. This explanation also agrees with the fact that the Gaussian distribution fits the spectra better than the Lorentz function. Once all the possible channels are participating in conduction, there is little temperature effect and other mechanisms do not increase the width further, so the width saturates fairly quickly.

Perhaps more remarkably, we observe that the width saturates above a certain input power, above ~ 50 W/m, regardless of the operating mode. We saw in single-tube unipolar CNTFETs that there is significant broadening due to field-induced ionization in the recombination region. Compared to the single-tube CNTFET operated as a unipolar emitter that requires a high electric field (e.g. 25 to 40 V/μm) for exciton production, the film LED has a much lower field in the emitting region, i.e., in the middle of the channel. This broadening effect was estimated to be 60 meV at the low end of the field (Figure III-11). The first-order approximation gives the maximum field of less than 7 V/μm due to the split gates; this of course is zero if different voltages are not applied to the gates. Given the device geometry, the middle of the channel is about two orders of magnitude farther away from the contacts than from the top gates, so the field changes little when the drain bias is increased. This can explain why the overall width is much smaller than in single unipolar devices, even when the film is operated as a regular FET. Furthermore, bias-dependent broadening is practically non-existent because there is no change in electric field between the gates, leading to the observed saturation behavior. The width is slightly greater for split-gate mode, where there does exist a small field (~7 V/μm as estimated above). Thus, the spectral width in the film device operated in different modes gives strong evidence for the field-induced broadening explained in Chapter III.

Even when the film device is operated as a global-gate FET (the black triangles in Figure V-10), the emission mechanism itself is still ambipolar recombination in the middle of the channel, where the field is too small for exciton production by impact excitation. Figure V-11 shows the emission intensity as a function of current for the three different modes. It shows clearly that much higher total current is required in the unipolar operating mode (black triangles), because it is the number of the minority carriers that limits emission by recombination. Since emission originates mid-channel, where the field is small, the overall width is much smaller than in unipolar single-tube devices, where exciton production and recombination occur in high fields. The width is comparable to those of the other two operating modes, since broadening mechanisms are the same for different operating modes, other than the small field that exists between the top gates in the diode mode.

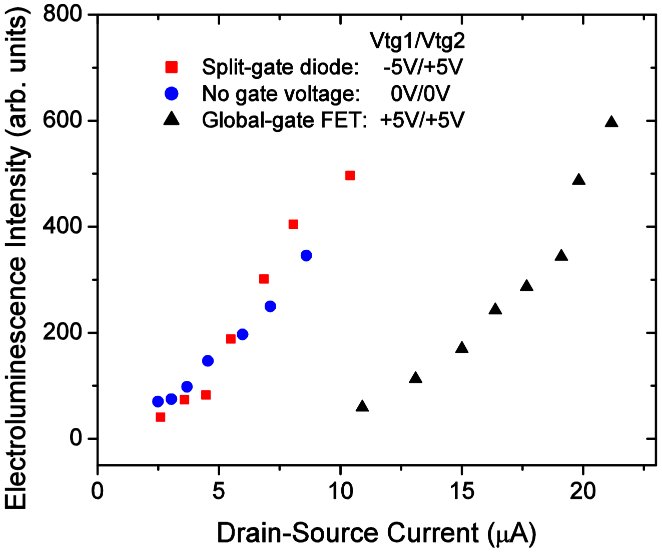

Figure V-11. Total electroluminescence intensity as a function of current, i.e., injected carriers. The intensity is extracted as the area of the Gaussian fit (see Figure V-10, inset). The graph shows that the emission originates from carrier recombination that requires a higher total current in the unipolar mode (black triangles) in which the number of minority carriers per unit current is small. Emission per current is comparable for split-gate and zero-gate modes because the ratio of majority to minority carriers is similar. See Figure V-10 captions for procedural details of fitting Gaussian function.

Finally, we investigate the polarization dependence of the electroluminescence emission of the CNT film diode. Based on SEM (see Figure V-1 (a)) and Raman imaging, individual CNTs (mostly in bundles) forming the film have been measured to lie almost parallel, within a range of 5° with respect to one another [99]. Since single CNTs are known to emit light that is strongly polarized in the direction of their long axes, we expect that the high degree of CNT alignment in the film translates into a pronounced light polarization effect. We inserted a linear polarizer in the optical path (Figure II-3) and measured the transmitted intensity as a function of the angle between the tube direction and the polarizer. We should point out that this measures the polarization property of the light itself, not the intensity as a function of the collection angle with respect to the device position and orientation, as in the dipole radiation. Based on the numerical aperture of the objective lens, we are collecting in the solid angle that covers about 4% at 90-degree angle to the tube direction.

Figure V - 12 clearly shows that the electroluminescence is linearly polarized in such a way that intensity maxima are obtained if the transmission direction of the polarizer is aligned with the CNT direction. The cosine-squared fits reveal intensity ratios I_{max}/I_{min} (i.e. ratios with polarizer at 0°/180° over 90°/270° in Figure V-12) close to 3.5. The degree of polarization is of the same order as those obtained in electroluminescence [73, 87], photoluminescence and Raman [137] as well as photoconductivity measurements [135, 136] performed on *single* nanotubes, demonstrating the extraordinary level of alignment in the CNT film.

We did not observe any statistically significant difference in the degree of light polarization when the CNT film diode is operated in the reverse mode (see Figure V-12 (b)). This is not unexpected, since the polarization dependence of the electroluminescence measurement reflects the nature of exciton recombination rather than exciton creation. Since we do not observe light emission from the CNT-metal-contacts that are covered by the metallic gates (see Figure V-6 (d)), the polarization dependence in both forward and reverse mode reflects solely the alignment of the CNTs in the "active area" between the split gates (see Figure 1).

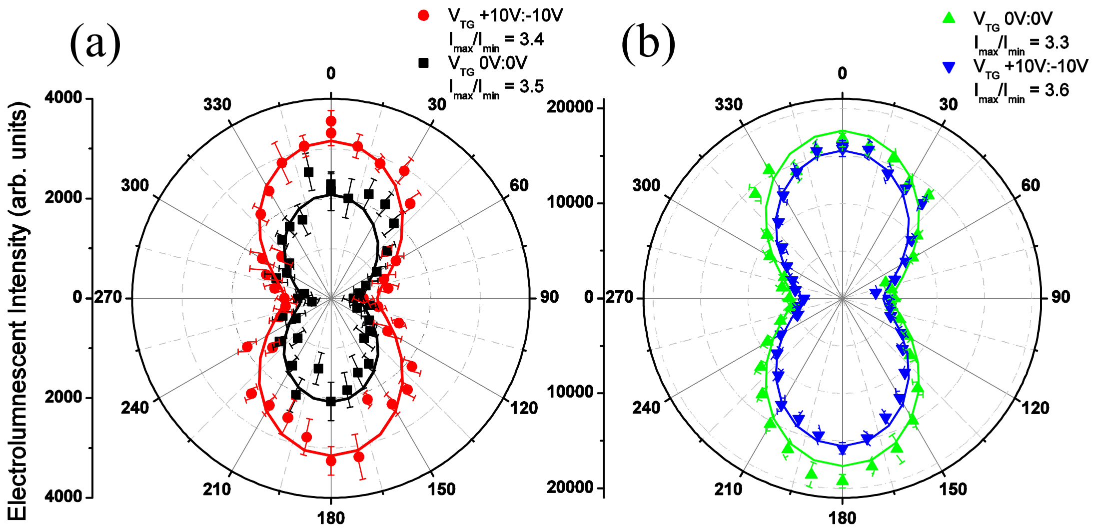

Figure V-12. Polarization dependence of the electroluminescence intensity from a CNT thin film diode in the (a) forward mode and (b) reverse mode (V_{DS}=10V for both (a) and (b)) for two different split gate settings V_{TG1}/V_{TG2} (solid symbols:

experiment, solid line: cosine squared fit). I_{max}/I_{min} is the ratio of the intensity maximum to the minimum from the fit. The overall intensity is much higher for the reverse mode (note the scale) because of the high current at the same V_{DS} (e.g. Figure V-8 (a) inset). The total intensity difference as a function of the top gate is smaller for the reverse mode, in agreement with Figure V-8 (a). The CNTs forming the film are aligned along the 0^o – 180^o marks.

6. Conclusions

We have realized polarized light-emitting diodes from highly aligned, separated semiconducting carbon nanotube films that show tunable light generation efficiencies and threshold-less light emission characteristics. Additional improvement in device performance can be expected by superior enrichment of the solution-processed CNT. Reduction of metallic tubes in the raw material will enable shorter device channels for better transport, or even eliminate percolation altogether, which means one can create devices equivalent to single-tube CNT LEDs in parallel. Also, avoidance of excess chemical treatment and processing will decrease the defect concentration of the CNT material and help to further improve the light generation efficiency.

Summary

There have been intense research efforts on carbon nanotubes ever since their discovery because of their unique physical, electronic, and optical properties. Their small size is ideally suited for use in nano-scale electronics, and their nearly perfect one-dimensional structure has interesting consequences in their electronic and optical characteristics, which were discussed in Chapter I. However, despite the considerable progress that has been made in the field, there are still many unanswered questions regarding their properties and emission mechanisms, especially in electroluminescence.

Although carbon nanotubes are a direct bandgap material, their radiative decay rate is quite low, limiting their usefulness in optical applications. The dominant mechanism of nonradiative decay has been the subject of debate, but it most likely depends on many variables (such as the tube species, environmental effects, temperature, doping, etc.), and therefore depends on the kind of experiment performed. Indeed, we found that a combination of multiple mechanisms seems to account for the very broad lineshape observed in the typical EL emission. In particular, the data on bias-dependent broadening agrees well with the exciton ionization model that points to high electric fields at emission sites as the origin of the broadening. We also observed emission from E_{12} and/or E_{21} states, which do not couple to photons in parallel polarization to the direction of the nanotube axis and is therefore not normally observed in PL. Our observation clearly shows that the emitted photons from these states are polarized in transverse direction to the nanotube axis.

We improved the emission efficiency considerably by fabricating single-tube p-n junction diodes made from long, small-diameter semiconducting carbon nanotubes. It circumvents the problem of high-fields by using the ambipolar emission scheme with a split-gate configuration that effectively controls space-dependent carrier concentration. The emission was found to be threshold-less with respect to current with an efficiency at least two orders of magnitude greater than in conventional CNT emitter, and the narrow linewidth yielded a much superior signal-to-noise ratio in the spectra, allowing us to explore the details of different peaks. In particular, we observed defect-induced localization of excitons about 65 meV below the free exciton state, which may further be contributing to the low emission efficiency rate [141]. The saturation of emission observed at higher current hints at an annihilation of these localized excitons, possibly by exciton-exciton interaction.

Finally, CNT film diodes were fabricated using a thin film of purified and aligned CNTs. Although the efficiency is limited in these devices because they rely on percolation for carrier transport, it showed a clear rectifying behavior and a very strong threshold-less emission that is tunable by the top gate. The polarization of the emission from film diodes was comparable to that of single tube CNTFETs.

Going forward, there is much that still needs to be addressed in electroluminescence from carbon nanotubes to understand its fundamental physics. For example, temperature measurements of phonons by Raman spectroscopy during transport could yield more precise information on relative populations of different phonons, although Raman spectroscopy from a single tube on a substrate is notoriously difficult. The situation can be improved by suspending CNTs across a trench to decrease signal quenching by the substrate, but the device would in turn be far more likely to fail from high temperature and oxidation. Another problem with this method is that the dielectric environment would no longer be the same (i.e., it changes the bandgap, excitonic binding energy and the phonon relaxation pathways), so the results would need to be interpreted with care to be applicable to on-substrate devices. Nonetheless, suspended CNTs are a promising structure for investigating their basic physics, especially in optics, because of the CNT's extreme sensitivity to extrinsic effects.

Another area that needs further exploration is the effect of external electric fields on the luminescence process. Electric fields all along the channel can be measured directly using photocurrent, which would provide a much more accurate estimate of its effects on exciton production and on broadening. The challenge is that the spatial resolution of such measurement is limited by the spot size of the excitation laser [70], so a significant improvement in the technique is needed to map out the details of Schottky barriers and other potential fluctuations along the channel.

From the applications point of view, the CNT film diode is perhaps the most promising type of device. The averaging effects that arise from using many tubes lead to reliable, robust and consistent performance. Advances in CNT purification techniques can create raw materials with even lower percentage of metallic nanotubes and perhaps even a very narrow range of diameters. Such CNTs, aligned and contacted so that each channel is comprised of just one tube instead of a series of tubes, could combine the benefits of the single-tube and film diodes and create efficient nano-scale light sources with high output in the near-infrared that would prove useful in many technological applications.

Bibliography

1.Avouris, P.; Chen, Z.; Perebeinos, V., Carbon-based electronics. *Nat. Nanotechnol.* **2007,** *2* (10), 605-615.

2.Iijima, S., Helical microtubules of graphitic carbon. *Nature* **1991,** *354* (6348), 56-58.

3.Iijima, S.; Ichihashi, T., Single-shell carbon nanotubes of 1-nm diameter. *Nature* **1993,** *363* (6430), 603-605.

4.Dresselhaus, M. S.; Dresselhaus, G.; Avouris, P., *Carbon Nanotubes : Synthesis, Structure, Properties, and Applications*. Springer: Berlin ; New York, 2001; Vol. 80, p xv, 447 p.

5.Jorio, A.; Dresselhaus, G.; Dresselhaus, M. S., *Carbon Nanotubes: Synthesis, Structure, Properties and Applications*. Springer: Berlin / Heidelberg, 2001; Vol. 80.

6.Jorio, A.; Dresselhaus, G.; Dresselhaus, M. S., *Carbon Nanotubes: Advanced Topics in the Synthesis, Structure, Properties and Applications*. Springer: Berlin / Heidelberg, 2008; Vol. 111.

7.Tans, S. J.; Verschueren, A. R. M.; Dekker, C., Room-temperature transistor based on a single carbon nanotube. *Nature* **1998,** *393* (6680), 49-52.

8.Martel, R.; Schmidt, T.; Shea, H. R.; Hertel, T.; Avouris, P., Single- and multi-wall carbon nanotube field-effect transistors. *Appl. Phys. Lett.* **1998,** *73* (17), 2447-2449.

9.Avouris, P.; Appenzeller, J.; Martel, R.; Wind, S. J., Carbon Nanotube Electronics. *Proc. IEEE* **2003,** *91* (11), 1772-1784.

10.Zaumseil, J.; Ho, X.; Guest, J. R.; Wiederrecht, G. P.; Rogers, J. A., Electroluminescence from Electrolyte-Gated Carbon Nanotube Field-Effect Transistors. *ACS Nano* **2009,** *3* (8), 2225-2234.

11.Mueller, T.; Kinoshita, M.; Steiner, M.; Perebeinos, V.; Bol, A. A.; Farmer, D. B.; Avouris, P., Efficient narrow-band light emission from a single carbon nanotube p-n diode. *Nat. Nanotechnol.* **2009,** *5* (1), 27-31.

12.Wallace, P. R., The Band Theory of Graphite. *Phys. Rev.* **1947,** *71* (9), 622.

13.Saito, R.; Dresselhaus, G.; Dresselhaus, M. S., Trigonal warping effect of carbon nanotubes. *Phys. Rev. B* **2000,** *61* (4), 2981.

14.Kataura, H.; Kumazawa, Y.; Maniwa, Y.; Umezu, I.; Suzuki, S.; Ohtsuka, Y.; Achiba, Y., Optical properties of single-wall carbon nanotubes. *Synth. Met.* **1999,** *103*, 2555-2558.

15.Weisman, R. B.; Bachilo, S. M., Dependence of Optical Transition Energies on Structure for Single-Walled Carbon Nanotubes in Aqueous Suspension: An Empirical Kataura Plot. *Nano Lett.* **2003,** *3* (9), 1235-1238.

16.O'Connell, M. J.; Bachilo, S. M.; Huffman, C. B.; Moore, V. C.; Strano, M. S.; Haroz, E. H.; Rialon, K. L.; Boul, P. J.; Noon, W. H.; Kittrell, C.; Ma, J.; Hauge, R. H.; Weisman, R. B.; Smalley, R. E., Band Gap Fluorescence from Individual Single-Walled Carbon Nanotubes. *Science* **2002,** *297* (5581), 593-596.

17.Capaz, R. B.; Spataru, C. D.; Ismail-Beigi, S.; Louie, S. G., Diameter and chirality dependence of exciton properties in carbon nanotubes. *Phys. Rev. B* **2006,** *74* (12), 121401.

18.Dukovic, G.; Wang, F.; Song, D.; Sfeir, M. Y.; Heinz, T. F.; Brus, L. E., Structural Dependence of Excitonic Optical Transitions and Band-Gap Energies in Carbon Nanotubes. *Nano Lett.* **2005,** *5* (11), 2314-2318.

19.Zhao, H.; Mazumdar, S., Electron-Electron Interaction Effects on the Optical Excitations of Semiconducting Single-Walled Carbon Nanotubes. *Phys. Rev. Lett.* **2004,** *93* (15), 157402.

20.Lin, H.; Lagoute, J.; Repain, V.; Chacon, C.; Girard, Y.; Lauret, J. S.; Ducastelle, F.; Loiseau, A.; Rousset, S., Many-body effects in electronic bandgaps of carbon nanotubes measured by scanning tunnelling spectroscopy. *Nat. Mater.* *9* (3), 235-238.

21.Hybertsen, M. S.; Louie, S. G., Electron correlation in semiconductors and insulators: Band gaps and quasiparticle energies. *Phys. Rev. B* **1986,** *34* (8), 5390.

22.Kane, C. L.; Mele, E. J., Electron Interactions and Scaling Relations for Optical Excitations in Carbon Nanotubes. *Phys. Rev. Lett.* **2004,** *93* (19), 197402.

23.Ando, T., Excitons in Carbon Nanotubes. *J. Phys. Soc. Jpn.* **1997,** *66*, 1066-1073.

24.Perebeinos, V.; Tersoff, J.; Avouris, P., Scaling of Excitons in Carbon Nanotubes. *Phys. Rev. Lett.* **2004,** *92* (25), 257402.

25.Spataru, C. D.; Ismail-Beigi, S.; Benedict, L. X.; Louie, S. G., Excitonic Effects and Optical Spectra of Single-Walled Carbon Nanotubes. *Phys. Rev. Lett.* **2004,** *92* (7), 077402-4.

26.Maultzsch, J.; Pomraenke, R.; Reich, S.; Chang, E.; Prezzi, D.; Ruini, A.; Molinari, E.; Strano, M. S.; Thomsen, C.; Lienau, C., Exciton binding energies in carbon nanotubes from two-photon photoluminescence. *Phys. Rev. B* **2005,** *72* (24), 241402-4.

27.Qiu, X.; Freitag, M.; Perebeinos, V.; Avouris, P., Photoconductivity Spectra of Single-Carbon Nanotubes: Implications on the Nature of Their Excited States. *Nano Lett.* **2005,** *5* (4), 749-752.

28.Wang, F.; Dukovic, G.; Brus, L. E.; Heinz, T. F., The Optical Resonances in Carbon Nanotubes Arise from Excitons. *Science* **2005,** *308* (5723), 838-841.

29.Plentz, F.; Ribeiro, H. B.; Jorio, A.; Strano, M. S.; Pimenta, M. A., Direct Experimental Evidence of Exciton-Phonon Bound States in Carbon Nanotubes. *Phys. Rev. Lett.* **2005,** *95* (24), 247401.

30.Miyauchi, Y.; Maruyama, S., Identification of an excitonic phonon sideband by photoluminescence spectroscopy of single-walled carbon-13 nanotubes. *Phys. Rev. B* **2006,** *74* (3), 035415.

31.Scholes, G. D.; Tretiak, S.; McDonald, T. J.; Metzger, W. K.; Engtrakul, C.; Rumbles, G.; Heben, M. J., Low-Lying Exciton States Determine the Photophysics of Semiconducting Single Wall Carbon Nanotubes. *J. Phys. Chem. C* **2007,** *111* (30), 11139-11149.

32.Kilina, S.; Tretiak, S.; Doorn, S. K.; Luo, Z.; Papadimitrakopoulos, F.; Piryatinski, A.; Saxena, A.; Bishop, A. R., Cross-polarized excitons in carbon nanotubes. *Proc. Natl. Acad. Sci. U. S. A.* **2008,** *105* (19), 6797-6802.

33.Perebeinos, V.; Tersoff, J.; Avouris, P., Radiative Lifetime of Excitons in Carbon Nanotubes. *Nano Lett.* **2005,** *5* (12), 2495-2499.

34.Spataru, C. D.; Ismail-Beigi, S.; Capaz, R. B.; Louie, S. G., Theory and Ab Initio Calculation of Radiative Lifetime of Excitons in Semiconducting Carbon Nanotubes. *Phys. Rev. Lett.* **2005,** *95* (24), 247402.

35.Mortimer, I. B.; Nicholas, R. J., Role of Bright and Dark Excitons in the Temperature-Dependent Photoluminescence of Carbon Nanotubes. *Phys. Rev. Lett.* **2007,** *98* (2), 027404.

36.Spataru, C. D.; Léonard, F., Tunable Band Gaps and Excitons in Doped Semiconducting Carbon Nanotubes Made Possible by Acoustic Plasmons. *Phys. Rev. Lett.* **2010,** *104* (17), 177402.

37.Jorio, A.; Saito, R.; Hafner, J. H.; Lieber, C. M.; Hunter, M.; McClure, T.; Dresselhaus, G.; Dresselhaus, M. S., Structural (n, m) Determination of Isolated Single-Wall Carbon Nanotubes by Resonant Raman Scattering. *Phys. Rev. Lett.* **2001,** *86* (6), 1118.

38.Saito, R.; Fantini, C.; Jiang, J., Excitonic States and Resonance Raman Spectroscopy of single-Wall Carbon Nanotubes. In *Carbon Nanotubes: Advanced Topics in the Synthesis, Structure, Properties and Applications*, Jorio, A., Dresselhaus, M. S., Dresselhaus, G., Ed. Springer-Verlag: Berlin, Heidelberg, 2008; Vol. 111.

39.Perebeinos, V.; Tersoff, J.; Avouris, P., Effect of Exciton-Phonon Coupling in the Calculated Optical Absorption of Carbon Nanotubes. *Phys. Rev. Lett.* **2005,** *94* (2), 027402.

40.Piscanec, S.; Lazzeri, M.; Robertson, J.; Ferrari, A. C.; Mauri, F., Optical phonons in carbon nanotubes: Kohn anomalies, Peierls distortions, and dynamic effects. *Phys. Rev. B* **2007,** *75* (3), 035427.

41.Jorio, A.; Souza Filho, A. G.; Dresselhaus, G.; Dresselhaus, M. S.; Swan, A. K.; Ünlü, M. S.; Goldberg, B. B.; Pimenta, M. A.; Hafner, J. H.; Lieber, C. M.; Saito, R., G-band resonant Raman study of 62 isolated single-wall carbon nanotubes. *Phys. Rev. B* **2002,** *65* (15), 155412.

42.Doorn, S. K.; Zheng, L.; O'Connell, M. J.; Zhu, Y.; Huang, S.; Liu, J., Raman Spectroscopy and Imaging of Ultralong Carbon Nanotubes. *J. Phys. Chem. B* **2005,** *109* (9), 3751-3758.

43.Htoon, H.; O'Connell, M. J.; Doorn, S. K.; Klimov, V. I., Single Carbon Nanotubes Probed by Photoluminescence Excitation Spectroscopy: The Role of Phonon-Assisted Transitions. *Phys. Rev. Lett.* **2005,** *94* (12), 127403.

44.Chou, S. G.; Plentz, F.; Jiang, J.; Saito, R.; Nezich, D.; Ribeiro, H. B.; Jorio, A.; Pimenta, M. A.; Samsonidze, G. G.; Santos, A. P.; Zheng, M.; Onoa, G. B.; Semke, E. D.; Dresselhaus, G.; Dresselhaus, M. S., Phonon-Assisted Excitonic Recombination Channels Observed in DNA-Wrapped Carbon Nanotubes Using Photoluminescence Spectroscopy. *Phys. Rev. Lett.* **2005,** *94* (12), 127402.

45.Yu, G.; Liang, Q.; Jia, Y.; Dong, J., Phonon sidebands of photoluminescence in single wall carbon nanotubes. *J. Appl. Phys.* **2010,** *107* (2), 024314-4.

46.Zeng, H.; Zhao, H.; Zhang, F.-C.; Cui, X., Observation of Exciton-Phonon Sideband in Individual Metallic Single-Walled Carbon Nanotubes. *Phys. Rev. Lett.* **2009,** *102* (13), 136406.

47.Collins, P. G.; Arnold, M. S.; Avouris, P., Engineering Carbon Nanotubes and Nanotube Circuits Using Electrical Breakdown. *Science* **2001,** *292* (5517), 706-709.

48.Wei, Y.; Xie, C.; Dean, K. A.; Coll, B. F., Stability of carbon nanotubes under electric field studied by scanning electron microscopy. *Appl. Phys. Lett.* **2001,** *79* (27), 4527-4529.

49.Yao, Z.; Kane, C. L.; Dekker, C., High-Field Electrical Transport in Single-Wall Carbon Nanotubes. *Phys. Rev. Lett.* **2000,** *84* (13), 2941.

50.Pop, E.; Mann, D. A.; Goodson, K. E.; Dai, H., Electrical and thermal transport in metallic single-wall carbon nanotubes on insulating substrates. *J. Appl. Phys.* **2007,** *101* (9), 093710.

51.Javey, A.; Guo, J.; Paulsson, M.; Wang, Q.; Mann, D.; Lundstrom, M.; Dai, H., High-Field Quasiballistic Transport in Short Carbon Nanotubes. *Phys. Rev. Lett.* **2004,** *92* (10), 106804.

52.Park, J.-Y.; Rosenblatt, S.; Yaish, Y.; Sazonova, V.; Uestuenel, H.; Braig, S.; Arias, T. A.; Brouwer, P. W.; McEuen, P. L., Electron-Phonon Scattering in Metallic Single-Walled Carbon Nanotubes. *Nano Lett.* **2004,** *4* (3), 517-520.

53.Pop, E.; Mann, D.; Cao, J.; Wang, Q.; Goodson, K.; Dai, H., Negative Differential Conductance and Hot Phonons in Suspended Nanotube Molecular Wires. *Phys. Rev. Lett.* **2005,** *95* (15), 155505.

54.Liao, A.; Zhao, Y.; Pop, E., Avalanche-Induced Current Enhancement in Semiconducting Carbon Nanotubes. *Phys. Rev. Lett.* **2008,** *101* (25), 256804.

55.Javey, A.; Qi, P.; Wang, Q.; Dai, H., Ten- to 50-nm-long quasi-ballistic carbon nanotube devices obtained without complex lithography. *Proc. Natl. Acad. Sci. U. S. A.* **2004,** *101* (37), 13408-13410.

56.Chen, Z.; Appenzeller, J.; Knoch, J.; Lin, Y.-m.; Avouris, P., The Role of Metal-Nanotube Contact in the Performance of Carbon Nanotube Field-Effect Transistors. *Nano Lett.* **2005,** *5* (7), 1497-1502.

57.Javey, A.; Guo, J.; Wang, Q.; Lundstrom, M.; Dai, H., Ballistic carbon nanotube field-effect transistors. *Nature* **2003,** *424* (6949), 654-657.

58.Chen, Y.-F.; Fuhrer, M. S., Electric-Field-Dependent Chrage-Carrier Velocity in Semiconducting Carbon Nanotubes. *Phys. Rev. Lett.* **2005,** *95*, 236803.

59.Datta, S., *Electronic Transport in Mesoscopic Systems*. Academic Press: New York, 1997.

60.Kong, J.; Yenilmez, E.; Tombler, T. W.; Kim, W.; Dai, H.; Laughlin, R. B.; Liu, L.; Jayanthi, C. S.; Wu, S. Y., Quantum Interference and Ballistic Transmission in Nanotube Electron Waveguides. *Phys. Rev. Lett.* **2001,** *87* (10), 106801.

61.Liang, W.; Bockrath, M.; Bozovic, D.; Hafner, J. H.; Tinkham, M.; Park, H., Fabry - Perot interference in a nanotube electron waveguide. *Nature* **2001,** *411* (6838), 665-669.

62.Purewal, M. S.; Hong, B. H.; Ravi, A.; Chandra, B.; Hone, J.; Kim, P., Scaling of Resistance and Electron Mean Free Path of Single-Walled Carbon Nanotubes. *Phys. Rev. Lett.* **2007,** *98* (18), 186808.

63.Durkop, T.; Getty, S. A.; Cobas, E.; Fuhrer, M. S., Extraordinary Mobility in Semiconducting Carbon Nanotubes. *Nano Lett.* **2003,** *4* (1), 35-39.

64.Heinze, S.; Tersoff, J.; Martel, R.; Derycke, V.; Appenzeller, J.; Avouris, P., Carbon Nanotubes as Schottky Barrier Transistors. *Phys. Rev. Lett.* **2002,** *89* (10), 106801.

65.Léonard, F.; Tersoff, J., Role of Fermi-Level Pinning in Nanotube Schottky Diodes. *Phys. Rev. Lett.* **2000,** *84* (20), 4693.

66.Appenzeller, J.; Knoch, J.; Derycke, V.; Martel, R.; Wind, S.; Avouris, P., Field-Modulated Carrier Transport in Carbon Nanotube Transistors. *Phys. Rev. Lett.* **2002,** *89* (12), 126801.

67.Nosho, Y.; Ohno, Y.; Kishimoto, S.; Mizutani, T., n-type carbon nanotube field-effect transistors fabricated by using Ca contact electrodes. *Appl. Phys. Lett.* **2005,** *86* (7), 073105.

68.Lide, D. R., *CRC Handbook of Chemistry and Physics*. 2006.

69.Appenzeller, J.; Radosavljevic, M.; Knoch, J.; Avouris, P., Tunneling Versus Thermionic Emission in One-Dimensional Semiconductors. *Phys. Rev. Lett.* **2004,** *92* (4), 048301.

70.Freitag, M.; Tsang, J. C.; Bol, A.; Yuan, D.; Liu, J.; Avouris, P., Imaging of the Schottky Barriers and Charge Depletion in Carbon Nanotube Transistors. *Nano Lett.* **2007,** *7* (7), 2037-2042.

71.Chen, J.; Perebeinos, V.; Freitag, M.; Tsang, J.; Fu, Q.; Liu, J.; Avouris, P., Bright Infrared Emission from Electrically Induced Excitons in Carbon Nanotubes. *Science* **2005,** *310* (5751), 1171-1174.

72.Freitag, M.; Tsang, J. C.; Kirtley, J.; Carlsen, A.; Chen, J.; Troeman, A.; Hilgenkamp, H.; Avouris, P., Electrically Excited, Localized Infrared Emission from Single Carbon Nanotubes. *Nano Lett.* **2006,** *6* (7), 1425-1433.

73.Misewich, J. A.; Martel, R.; Avouris, P.; Tsang, J. C.; Heinze, S.; Tersoff, J., Electrically Induced Optical Emission from a Carbon Nanotube FET. *Science* **2003,** *300* (5620), 783-786.

74.Freitag, M.; Chen, J.; Tersoff, J.; Tsang, J. C.; Fu, Q.; Liu, J.; Avouris, P., Mobile Ambipolar Domain in Carbon-Nanotube Infrared Emitters. *Phys. Rev. Lett.* **2004,** *93* (7), 076803.

75.Tersoff, J.; Freitag, M.; Tsang, J. C.; Avouris, P., Device modeling of long-channel nanotube electro-optical emitter. *Appl. Phys. Lett.* **2005,** *86* (26), 263108.

76.Freitag, M.; Perebeinos, V.; Chen, J.; Stein, A.; Tsang, J. C.; Misewich, J. A.; Martel, R.; Avouris, P., Hot Carrier Electroluminescence from a Single Carbon Nanotube. *Nano Lett.* **2004,** *4* (6), 1063-1066.

77.Lefebvre, J.; Austing, D. G.; Bond, J.; Finnie, P., Photoluminescence Imaging of Suspended Single-Walled Carbon Nanotubes. *Nano Lett.* **2006,** *6* (8), 1603-1608.

78.Wang, F.; Dukovic, G.; Brus, L. E.; Heinz, T. F., Time-Resolved Fluorescence of Carbon Nanotubes and Its Implication for Radiative Lifetimes. *Phys. Rev. Lett.* **2004,** *92* (17), 177401.

79.Tsyboulski, D. A.; Rocha, J.-D. R.; Bachilo, S. M.; Cognet, L.; Weisman, R. B., Structure-Dependent Fluorescence Efficiencies of Individual Single-Walled Carbon Nanotubes. *Nano Lett.* **2007,** *7* (10), 3080-3085.

80.Lee, J. U.; Gipp, P. P.; Heller, C. M., Carbon nanotube p-n junction diodes. *Appl. Phys. Lett.* **2004,** *85* (1), 145-147.

81.Lee, J. U., Photovoltaic effect in ideal carbon nanotube diodes. *Appl. Phys. Lett.* **2005,** *87*, 073101.

82.Lee, J. U., Band-gap renormalization in carbon nanotubes: Origin of the ideal diode behavior in carbon nanotube p-n structures. *Phys. Rev. B* **2007,** *75* (7), 075409.

83.Lee, J. U.; Codella, P. J.; Pietrzykowski, M., Direct probe of excitonic and continuum transitions in the photocurrent spectroscopy of individual carbon nanotube p-n diodes. *Appl. Phys. Lett.* **2007,** *90* (5), 053103.

84.Perebeinos, V.; Avouris, P., Impact excitation by hot carriers in carbon nanotubes. *Phys. Rev. B* **2006,** *74* (12), 121410.

85.Marty, L.; Adam, E.; Albert, L.; Doyon, R.; Menard, D.; Martel, R., Exciton Formation and Annihilation during 1D Impact Excitation of Carbon Nanotubes. *Phys. Rev. Lett.* **2006,** *96* (13), 136803.

86.Li, P.; Jiang, K.; Liu, M.; Li, Q.; Fan, S., Polarized incandescent light emission from carbon nanotubes. *Appl. Phys. Lett.* **2003,** *82* (11), 1763-1765.

87.Mann, D.; Kato, Y. K.; Kinkhabwala, A.; Pop, E.; Cao, J.; Wang, X.; Zhang, L.; Wang, Q.; Guo, J.; Dai, H., Electrically driven thermal light emission from individual single-walled carbon nanotubes. *Nat. Nanotechnol.* **2007,** *2* (1), 33-38.

88.Wang, X.; Zhang, L.; Lu, Y.; Dai, H.; Kato, Y. K.; Pop, E., Electrically driven light emission from hot single-walled carbon nanotubes at various temperatures and ambient pressures. *Appl. Phys. Lett.* **2007,** *91* (26), 261102.

89.Deshpande, V. V.; Hsieh, S.; Bushmaker, A. W.; Bockrath, M.; Cronin, S. B., Spatially Resolved Temperature Measurements of Electrically Heated Carbon Nanotubes. *Phys. Rev. Lett.* **2009,** *102* (10), 105501.

90.Artukovic, E.; Kaempgen, M.; Hecht, D. S.; Roth, S.; Grüner, G., Transparent and Flexible Carbon Nanotube Transistors. *Nano Lett.* **2005,** *5* (4), 757-760.

91.Cao, Q.; Kim, H.-s.; Pimparkar, N.; Kulkarni, J. P.; Wang, C.; Shim, M.; Roy, K.; Alam, M. A.; Rogers, J. A., Medium-scale carbon nanotube thin-film integrated circuits on flexible plastic substrates. *Nature* **2008,** *454* (7203), 495-500.

92.Cao, Q.; Rogers, J. A., Ultrathin Films of Single-Walled Carbon Nanotubes for Electronics and Sensors: A Review of Fundamental and Applied Aspects. *Adv. Mater.* **2008,** *21* (1), 29 - 53.

93.Hu, L.; Hecht, D. S.; Grüner, G., Percolation in Transparent and Conducting Carbon Nanotube Networks. *Nano Lett.* **2004,** *4* (12), 2513-2517.

94.LeMieux, M. C.; Roberts, M.; Barman, S.; Jin, Y. W.; Kim, J. M.; Bao, Z., Self-Sorted, Aligned Nanotube Networks for Thin-Film Transistors. *Science* **2008,** *321* (5885), 101-104.

95.Snow, E. S.; Campbell, P. M.; Ancona, M. G.; Novak, J. P., High-mobility carbon-nanotube thin-film transistors on a polymeric substrate. *Appl. Phys. Lett.* **2005,** *86* (3), 033105.

96.Snow, E. S.; Novak, J. P.; Campbell, P. M.; Park, D., Random networks of carbon nanotubes as an electronic material. *Appl. Phys. Lett.* **2003,** *82* (13), 2145-2147.

97.Adam, E.; Aguirre, C. M.; Marty, L.; St-Antoine, B. C.; Meunier, F.; Desjardins, P.; Ménard, D.; Martel, R., Electroluminescence from Single-Wall Carbon Nanotube Network Transistors. *Nano Lett.* **2008,** *8* (8), 2351-2355.

98.Arnold, M. S.; Green, A. A.; Hulvat, J. F.; Stupp, S. I.; Hersam, M. C., Sorting carbon nanotubes by electronic structure using density differentiation. *Nat. Nanotechnol.* **2006,** *1* (1), 60-65.

99.Engel, M.; Small, J. P.; Steiner, M.; Freitag, M.; Green, A. A.; Hersam, M. C.; Avouris, P., Thin Film Nanotube Transistors Based on Self-Assembled, Aligned, Semiconducting Carbon Nanotube Arrays. *ACS Nano* **2008,** *2* (12), 2445-2452.

100.Liu, C.; Cheng, H.-M.; Cong, H. T.; Li, F.; Su, G.; Zhou, B. L.; Dresselhaus, M. S., Synthesis of Macroscopically Long Ropes of Well-Aligned Single-Walled Carbon Nanotubes. *Adv. Mater.* **2000,** *12* (16), 1190-1192.

101.Huang, L.; Cui, X.; White, B.; O`Brien, S. P., Long and Oriented Single-Walled Carbon Nanotubes Grown by Ethanol Chemical Vapor Deposition. *J. Phys. Chem. B* **2004,** *108* (42), 16451-16456.

102.Scott, C. D.; Arepalli, S.; Nikolaev, P.; Smalley, R. E., Growth mechanisms for single-wall carbon nanotubes in a laser-ablation process. *Applied Physics A: Materials Science & Processing* **2001,** *72* (5), 573-580.

103.Bethune, D. S.; Klang, C. H.; de Vries, M. S.; Gorman, G.; Savoy, R.; Vazquez, J.; Beyers, R., Cobalt-catalysed growth of carbon nanotubes with single-atomic-layer walls. *Nature* **1993,** *363* (6430), 605-607.

104.Estrada, D.; et al., Reduction of hysteresis for carbon nanotube mobility measurements using pulsed characterization. *Nanotechnology* **2010,** *21* (8), 085702.

105.Ohno, Y.; Kishimoto, S.; Mizutani, T., Photoluminescence of single-walled carbon nanotubes in field-effect transistors. *Nanotechnology* **2006,** *17*, 549-555.

106.Kim, W.; Javey, A.; Vermesh, O.; Wang, Q.; Li, Y.; Dai, H., Hysteresis Caused by Water Molecules in Carbon Nanotube Field-Effect Transistors. *Nano Lett.* **2003,** *3* (2), 193-198.

107.Ong, H. G.; Cheah, J. W.; Chen, L.; TangTang, H.; Xu, Y.; Li, B.; Zhang, H.; Li, L.-J.; Wang, J., Charge injection at carbon nanotube-SiO[sub 2] interface. *Appl. Phys. Lett.* **2008,** *93* (9), 093509.

108.Vijayaraghavan, A.; Kar, S.; Soldano, C.; Talapatra, S.; Nalamasu, O.; Ajayan, P. M., Charge-injection-induced dynamic screening and origin of hysteresis in field-modulated transport in single-wall carbon nanotubes. *Appl. Phys. Lett.* **2006,** *89* (16), 162108.

109.Freitag, M.; Steiner, M.; Naumov, A.; Small, J. P.; Bol, A. A.; Perebeinos, V.; Avouris, P., Carbon Nanotube Photo- and Electroluminescence in Longitudinal Electric Fields. *ACS Nano* **2009,** *3* (11), 3744-3748.

110.Okuto, Y.; Crowell, C. R., Energy-Conservation Considerations in the Characterization of Impact Ionization in Semiconductors. *Phys. Rev. B* **1972,** *6*, 3076-3081.

111.Avouris, P.; Freitag, M.; Perebeinos, V., Carbon-nanotube photonics and optoelectronics. *Nat. Photonics* **2008,** *2* (6), 341-350.

112.Steiner, M.; Freitag, M.; Perebeinos, V.; Tsang, J. C.; Small, J. P.; Kinoshita, M.; Yuan, D.; Liu, J.; Avouris, P., Phonon populations and electrical power dissipation in carbon nanotube transistors. *Nat. Nanotechnol.* **2009,** *4* (5), 320-324.

113.Ueta, M.; Kanzaki, H.; Kobayashi, K.; Toyozawa, Y.; Hanamura, E., *Excitonic Processes in Solids*. Springer-Verlag: 1986; Vol. 60.

114.Htoon, H.; O'Connell, M. J.; Cox, P. J.; Doorn, S. K.; Klimov, V. I., Low Temperature Emission Spectra of Individual Single-Walled Carbon Nanotubes: Multiplicity of Subspecies within Single-Species Nanotube Ensembles. *Phys. Rev. Lett.* **2004,** *93* (2), 027401.

115.Lefebvre, J.; Finnie, P.; Homma, Y., Temperature-dependent photoluminescence from single-walled carbon nanotubes. *Phys. Rev. B* **2004,** *70* (4), 045419.

116.Lefebvre, J.; Fraser, J. M.; Finnie, P.; Homma, Y., Photoluminescence from an individual single-walled carbon nanotube. *Phys. Rev. B* **2004,** *69* (7), 075403.

117.Xie, L.; Farhat, H.; Son, H.; Zhang, J.; Dresselhaus, M. S.; Kong, J.; Liu, Z., Electroluminescence from Suspended and On-Substrate Metallic Single-Walled Carbon Nanotubes. *Nano Lett.* **2009,** *9* (5), 1747-1751.

118.Mohite, A. D.; Gopinath, P.; Shah, H. M.; Alphenaar, B. W., Exciton Dissociation and Stark Effect in the Carbon Nanotube Photocurrent Spectrum. *Nano Lett.* **2008,** *8* (1), 142-146.

119.Lefebvre, J.; Finnie, P., Polarized Photoluminescence Excitation Spectroscopy of Single-Walled Carbon Nanotubes. *Phys. Rev. Lett.* **2007,** *98* (16), 167406.

120.Yoshikawa, K.; Matsunaga, R.; Matsuda, K.; Kanemitsu, Y., Mechanism of exciton dephasing in a single carbon nanotube studied by photoluminescence spectroscopy. *Appl. Phys. Lett.* **2009,** *94* (9), 093109.

121.Fan, Y.; Singer, S. B.; Bergstrom, R.; Regan, B. C., Probing Planck's Law with Incandescent Light Emission from a Single Carbon Nanotube. *Phys. Rev. Lett.* **2009,** *102* (18), 187402.

122.Sveningsson, M.; Jonsson, M.; Nerushev, O. A.; Rohmund, F.; Campbell, E. E. B., Blackbody radiation from resistively heated multiwalled carbon nanotubes during field emission. *Appl. Phys. Lett.* **2002,** *81* (6), 1095-1097.

123.Gabor, N. M.; Zhong, Z.; Bosnick, K.; Park, J.; McEuen, P. L., Extremely Efficient Multiple Electron-Hole Pair Generation in Carbon Nanotube Photodiodes. *Science* **2009,** *325* (5946), 1367-1371.

124.Perebeinos, V.; Avouris, P., Exciton Ionization, Franz-Keldysh, and Stark Effects in Carbon Nanotubes. *Nano Lett.* **2007,** *7* (3), 609-613.

125.Heinze, S.; Radosavljevic, M.; Tersoff, J.; Avouris, P., Unexpected scaling of the performance of carbon nanotube Schottky-barrier transistors. *Phys. Rev. B* **2003,** *68* (23), 235418.

126. Wang, S. Q.; Mahan, G. D., Electron Scattering from Surface Excitations. *Phys. Rev. B* **1972,** *6* (12), 4517.

127. Matsuda, K.; Inoue, T.; Murakami, Y.; Maruyama, S.; Kanemitsu, Y., Exciton dephasing and multiexciton recombinations in a single carbon nanotube. *Phys. Rev. B* **2008,** *77* (3), 033406.

128. Murakami, Y.; Kono, J., Nonlinear Photoluminescence Excitation Spectroscopy of Carbon Nanotubes: Exploring the Upper Density Limit of One-Dimensional Excitons. *Phys. Rev. Lett.* **2009,** *102* (3), 037401.

129. Ma, Y.-Z.; Valkunas, L.; Dexheimer, S. L.; Bachilo, S. M.; Fleming, G. R., Femtosecond Spectroscopy of Optical Excitations in Single-Walled Carbon Nanotubes: Evidence for Exciton-Exciton Annihilation. *Phys. Rev. Lett.* **2005,** *94* (15), 157402.

130. Hagen, A.; Steiner, M.; Raschke, M. B.; Lienau, C.; Hertel, T.; Qian, H.; Meixner, A. J.; Hartschuh, A., Exponential Decay Lifetimes of Excitons in Individual Single-Walled Carbon Nanotubes. *Phys. Rev. Lett.* **2005,** *95* (19), 197401.

131. Ajiki, H.; Ando, T., Aharonov-Bohm effect in carbon nanotubes. *Physica B* **1994,** *201*, 349-352.

132. Ajiki, H.; Ando, T., Carbon Nanotubes: Optical Absorption in Aharonov-Bohm Flux. *Jpn. J. Appl. Phys. Suppl.* **1995,** *34-1*, 107-109.

133. Uryu, S.; Ando, T., Exciton absorption of perpendicularly polarized light in carbon nanotubes. *Phys. Rev. B* **2006,** *74* (15), 155411.

134. Lefebvre, J.; Finnie, P., Excited Excitonic States in Single-Walled Carbon Nanotubes. *Nano Lett.* **2008,** *8* (7), 1890-1895.

135. Balasubramanian, K.; Fan, Y.; Burghard, M.; Kern, K.; Friedrich, M.; Wannek, U.; Mews, A., Photoelectronic transport imaging of individual semiconducting carbon nanotubes. *Appl. Phys. Lett.* **2004,** *84* (13), 2400-2402.

136. Freitag, M.; Martin, Y.; Misewich, J. A.; Martel, R.; Avouris, P., Photoconductivity of Single Carbon Nanotubes. *Nano Lett.* **2003,** *3* (8), 1067-1071.

137. Hartschuh, A.; Pedrosa, H. N.; Novotny, L.; Krauss, T. D., Simultaneous Fluorescence and Raman Scattering from Single Carbon Nanotubes. *Science* **2003,** *301* (5638), 1354-1356.

138. Milosevic, I.; Vukovic, T.; Dmitrovic, S.; Damnjanovic, M., Polarized optical absorption in carbon nanotubes: A symmetry-based approach. *Phys. Rev. B* **2003,** *67* (16), 165418.

139. Miyauchi, Y.; Oba, M.; Maruyama, S., Cross-polarized optical absorption of single-walled nanotubes by polarized photoluminescence excitation spectroscopy. *Phys. Rev. B* **2006,** *74* (20), 205440.

140. Grüneis, A.; Saito, R.; Samsonidze, G. G.; Kimura, T.; Pimenta, M. A.; Jorio, A.; Filho, A. G. S.; Dresselhaus, G.; Dresselhaus, M. S., Inhomogeneous optical absorption around the K point in graphite and carbon nanotubes. *Phys. Rev. B* **2003,** *67* (16), 165402.

141. Perebeinos, V.; Avouris, P., Phonon and Electronic Nonradiative Decay Mechanisms of Excitons in Carbon Nanotubes. *Phys. Rev. Lett.* **2008,** *101* (5), 057401.

142. Xia, F.; Steiner, M.; Lin, Y.-m.; Avouris, P., A microcavity-controlled, current-driven, on-chip nanotube emitter at infrared wavelengths. *Nat. Nanotechnol.* **2008,** *3* (10), 609-613.

143. Harutyunyan, H.; Gokus, T.; Green, A. A.; Hersam, M. C.; Allegrini, M.; Hartschuh, A., Defect-Induced Photoluminescence from Dark Excitonic States in Individual Single-Walled Carbon Nanotubes. *Nano Lett.* **2009,** *9* (5), 2010-2014.

144. Kiowski, O.; Arnold, K.; Lebedkin, S.; Hennrich, F.; Kappes, M. M., Direct Observation of Deep Excitonic States in the Photoluminescence Spectra of Single-Walled Carbon Nanotubes. *Phys. Rev. Lett.* **2007,** *99* (23), 237402.

145. Steiner, M.; Freitag, M.; Tsang, J.; Perebeinos, V.; Bol, A.; Failla, A.; Avouris, P., How does the substrate affect the Raman and excited state spectra of a carbon nanotube? *Appl. Phys. A* **2009,** *96*, 271-282.

146. Wang, F.; Dukovic, G.; Knoesel, E.; Brus, L. E.; Heinz, T. F., Observation of rapid Auger recombination in optically excited semiconducting carbon nanotubes. *Phys. Rev. B* **2004,** *70* (24), 241403.

147. Wang, F.; Wu, Y.; Hybertsen, M. S.; Heinz, T. F., Auger recombination of excitons in one-dimensional systems. *Phys. Rev. B* **2006,** *73* (24), 245424.

148. Steiner, M.; Freitag, M.; Perebeinos, V.; Naumov, A.; Small, J. P.; Bol, A. A.; Avouris, P., Gate-Variable Light Absorption and Emission in a Semiconducting Carbon Nanotube. *Nano Lett.* **2009,** *9* (10), 3477-3481.

149. Walsh, A. G.; Vamivakas, A. N.; Yin, Y.; Cronin, S. B.; Unlu, M. S.; Goldberg, B. B.; Swan, A. K., Screening of Excitons in Single, Suspended Carbon Nanotubes. *Nano Lett.* **2007,** *7* (6), 1485-1488.

150. Jiang, J.; Saito, R.; Samsonidze, G. G.; Jorio, A.; Chou, S. G.; Dresselhaus, G.; Dresselhaus, M. S., Chirality dependence of exciton effects in single-wall carbon nanotubes: Tight-binding model. *Phys. Rev. B* **2007,** *75* (3), 035407.

151. Hogele, A.; Galland, C.; Winger, M.; Imamoglu, A., Photon Antibunching in the Photoluminescence Spectra of a Single Carbon Nanotube. *Phys. Rev. Lett.* **2008,** *100* (21), 217401.

152. Kinoshita, M.; Steiner, M.; Engel, M.; Small, J. P.; Green, A. A.; Hersam, M. C.; Krupke, R.; Mendez, E. E.; Avouris, P., The polarized carbon nanotube thin film LED. *Opt. Express* **2010,** *18* (25), 25738-25745.

153. Cognet, L.; Tsyboulski, D. A.; Rocha, J.-D. R.; Doyle, C. D.; Tour, J. M.; Weisman, R. B., Stepwise Quenching of Exciton Fluorescence in Carbon Nanotubes by Single-Molecule Reactions. *Science* **2007,** *316* (5830), 1465-1468.

154. Luer, L.; Hoseinkhani, S.; Polli, D.; Crochet, J.; Hertel, T.; Lanzani, G., Size and mobility of excitons in (6, 5) carbon nanotubes. *Nat. Phys.* **2009,** *5* (1), 54-58.

155. Sheng, C. X.; Vardeny, Z. V.; Dalton, A. B.; Baughman, R. H., Exciton dynamics in single-walled nanotubes: Transient photoinduced dichroism and polarized emission. *Phys. Rev. B* **2005,** *71* (12), 125427.

156. Miyauchi, Y.; Matsuda, K.; Yamamoto, Y.; Nakashima, N.; Kanemitsu, Y., Length-Dependent Photoluminescence Lifetimes in Single-Walled Carbon Nanotubes. *J. Phys. Chem. C* **2010,** *114* (30), 12905-12908.

157. Yuan, D.; Ding, L.; Chu, H.; Feng, Y.; McNicholas, T. P.; Liu, J., Horizontally Aligned Single-Walled Carbon Nanotube on Quartz from a Large Variety of Metal Catalysts. *Nano Lett.* **2008,** *8* (8), 2576-2579.

158. Ding, L.; Tselev, A.; Wang, J.; Yuan, D.; Chu, H.; McNicholas, T. P.; Li, Y.; Liu, J., Selective Growth of Well-Aligned Semiconducting Single-Walled Carbon Nanotubes. *Nano Lett.* **2009,** *9* (2), 800-805.

159. Qian, H.; Georgi, C.; Anderson, N.; Green, A. A.; Hersam, M. C.; Novotny, L.; Hartschuh, A., Exciton Energy Transfer in Pairs of Single-Walled Carbon Nanotubes. *Nano Lett.* **2008,** *8* (5), 1363-1367.

160. Tan, P. H.; Rozhin, A. G.; Hasan, T.; Hu, P.; Scardaci, V.; Milne, W. I.; Ferrari, A. C., Photoluminescence Spectroscopy of Carbon Nanotube Bundles: Evidence for Exciton Energy Transfer. *Phys. Rev. Lett.* **2007,** *99* (13), 137402.